

Experimental Study on Heat Transfer of Flat-Wall-Impinging Diesel Spray Flame

(平板に衝突するディーゼル噴霧火炎の壁面熱伝達に関する実験的研究)

学位取得年月 2019年9月

Rizal Mahmud

**EXPERIMENTAL STUDY ON HEAT
TRANSFER OF FLAT-WALL-IMPINGING DIESEL SPRAY FLAME**

by
RIZAL MAHMUD

Dissertation
Submitted to the Graduate School of Engineering
University of Hiroshima
In Partial Fulfillment of the Requirements
For the Degree of

Doctor of Engineering

University of Hiroshima
September, 2019

ABSTRACT

In internal combustion engines, a substantial amount of the fuel's energy input is lost due to heat transfer through the walls of the combustion chamber. This heat loss reduces thermal efficiency, as spray/wall impingement plays a crucial role in direct-injection diesel engines. The engine's heat loss occurs during combustion, mainly due to the heat transfer between the impinging spray/flame and the piston cavity wall. This study investigated the mechanism of the heat transfer from the spray flame to the impinging wall under small diesel engine-like condition.

To investigate the correlation between the diesel flame and wall heat loss, this research studied natural luminosity photography of the flame and measured transient heat flux to the wall. Using a constant volume vessel with a fixed impingement wall, the study measured the surface heat flux of the wall at the locations of spray flame impingement using three thin-film thermocouple heat-flux (TFTHF) sensors. The effects of impingement distance, injection pressure, nozzle hole diameter, and oxygen concentration and their combined effect on heat transfer were investigated parametrically.

The results show the effects of various experimental parameters on the spray/flame impingement behavior, with heat loss occurring significantly under some conditions. In some of the investigated parameter conditions, decreasing the oxygen concentration was effective in reducing the heat transfer through the wall due to the lower temperature distribution. Regarding the ratio of total heat transfer between non-combustion and combustion, around 30% of the heat transferred through the wall was caused by the convection of non-combustion evaporating spray. Moreover, we confirmed that the relationship between the Nusselt number and the Reynolds number was a useful measure for describing heat-transfer phenomena in diesel combustion.

CONTENTS

ABSTRACT	i
CONTENTS	ii
NOMENCLATURES	vi
CHAPTER 1 INTRODUCTION	1
1.1 BACKGROUND AND MOTIVATIONS	1
1.2 OBJECTIVES AND APPROACHES	3
1.3 OUTLINES	4
1.4 REVIEW OF PREVIOUS WORKS	5
1.4.1 Heat Transfer in Engine Combustion Chamber	5
1.4.2 Heat Transfer Correlation	6
1.4.3 Heat Transfer of Wall Impinging Spray	7
(1). Wall Impinging Spray Structure	7
(2). Wall Impinging Spray on Heat Transfer and Combustion Process	9
(3). Modeling of Wall Impingement	12
1.4.4 Optical Diagnostic Technique for Diesel Spray	15
1.5 SUMMARY	19
CHAPTER 2 EXPERIMENTAL APPERATUS, MEASURING METHODS, AND EXPERIMENTAL CONDITIONS	21
2.1 HIGH-PRESSURE AND HIGH-TEMPERATURE CHAMBER	21
2.2 IMPINGEMENT WALL	24
2.3 OPTICAL MEASUREMENT TECHNIQUES	24
2.3.1 Mie Scattering Method	24
2.3.2 Natural Luminosity Recording System and Two-Color Pyrometry	25
(1). Principle Two-Color Pyrometry	25
(2). Calibration of Two-Color Pyrometry	26
2.4 HEAT FLUX SENSOR AND MEASUREMENT	29

2.4.1 Thin Film Thermocouple Heat Flux Sensor	29
2.4.2 Heat Flux Measurement	30
2.5 DATA ACQUISITION	33
2.6 TEST CONDITIONS	35
2.7 SUMMARY	35
CHAPTER 3 HEAT TRANSFER UNDER BASELINE CONDITION.....	37
3.1 INTRODUCTION	37
3.2 EXPERIMENTAL CONDITIONS	37
3.3 SPRAY BEHAVIOR	39
3.4 COMBUSTION FLAME BEHAVIOR	41
3.5 HEAT FLUX AND TOTAL HEAT TRANSFER	42
3.6 SUMMARY	44
CHAPTER 4 HEAT TRANSFER UNDER VARIOUS IMPINGING DISTANCES	47
4.1 INTRODUCTION	47
4.2 EXPERIMENTAL CONDITIONS	47
4.3 SPRAY BEHAVIOR	48
4.4 COMBUSTION FLAME CHARACTERISTICS	50
4.4.1 Flame Natural Luminosity	50
4.4.2 Two-Color Method Results	52
4.4.3 Flame Contact Area	56
4.5 HEAT FLUX AND TOTAL HEAT TRANSFER	58
4.6 SUMMARY	63
CHAPTER 5 EFFECT OF INJECTION PRESSURE AND NOZZLE HOLE DIAMETER	65
5.1 INTRODUCTION	65
5.2 EXPERIMENTAL CONDITIONS	65
5.3 NON_COMBUSTION SPRAY BEHAVIOR AND WALL HEAT TRANSFER	
UNDER INJECTION PRESSURE	66
5.3.1 Spray Behavior	66
5.3.2 Heat Flux on the Wall Surface	70

5.4 COMBUSTION FLAME BEHAVIOR AND WALL HEAT TRANSFER UNDER INJECTION PRESSURE	71
5.4.1 Combustion Flame Behavior	71
5.4.2 Heat Flux on the Wall Surface	74
5.5 COMBUSTION FLAME BEHAVIOR AND WALL HEAT TRANSFER UNDER NOZZLE HOLE DIAMETER	79
5.5.1 Combustion Flame Behavior	79
5.5.2 Heat Flux on the Wall Surface	81
5.5.3 Effect Nozzle Hole Diameter and Injection Pressure on Areal Transferred Heat	84
5.6 SUMMARY	86
CHAPTER 6 EFFECT OF OXYGEN CONCENTRATION ON HEAT TRANSFER	89
6.1 INTRODUCTION	89
6.2 EXPERIMENTAL CONDITIONS	89
6.3 COMBUSTION FLAME BEHAVIOR	90
6.4 HEAT FLUX ON THE WALL SURFACE	93
6.5 SUMMARY	95
CHAPTER 7 COMBINED EFFECT OF IMPINGEMENT DISTANCE/INJECTION PRESSURE AND OXYGEN CONCENTRATION/INJECTION PRESSURE	97
7.1 INTRODUCTION	97
7.2 EXPERIMENTAL CONDITIONS	97
7.3 COMBINED EFFECT OF IMPINGEMENT DISTANCE/INJECTION PRESSURE ON WALL HEAT TRNASFER	99
7.3.1. Combined Effect of Impingement Distance and Injection Pressure under Non- combustion	101
7.3.2. Combined Effect of Impingement Distance and Injection Pressure under Combustion	102
7.3.3. Combined Effect of Impingement Distance and Injection Pressure on Wall Heat Transfer	103

7.4 COMBINED EFFECT OF OXYGEN CONCENTRATION/INJECTION PRESSURE ON WALL HEAT TRNASFER	105
7.5 HEAT TRANSFER CORRELATIONS	108
7.5.1 Flamelet Velocity	108
7.5.2 Relation between Reynolds Number and Nusselt Number	110
7.6 MULTIVARIABLE ANALYSIS	111
7.7 SUMMARY	114
CHAPTER 8 CONCLUSIONS	117
8.1 MAIN FINDINGS OF THIS STUDY	117
8.2 RECOMMENDATIONS FOR FUTURE WORKS	122
REFERENCES	124
ACKNOWLEDGEMENTS	135
APPENDIX	136
Data Acquisition Flowchart	
Validation Between Experiment and Simulation	
Paper Lists	

NOMENCLATURES

A	Instantaneous contact area
ASOI	After start of injection
CFD	Computational fluid dynamics
CVV	Constant volume vessel
DI	Direct injection
D_{imp}	Impingement distance
D_{imp}/P_{inj}	Impingement distance and high injection pressure
D_{hole}	Nozzle hole diameters
EGR	Exhaust gas recirculation
ECU	Electronic Control Unit
FFT	Fast Fourier Transform
fps	Frame speed per second
h	Heat transfer coefficient
i	Step in the depth direction
ICE	Internal combustion engines
K	Bulk modulus of the fuel
k	Step in the time direction
m	Mass of fuel
L	Characteristic length
LAS	The laser absorption-scattering
LIEF	Laser-induced exciplex fluorescence
LIF	Laser-induced fluorescence
LRS	Laser rayleigh scattering
O_2/P_{inj}	Oxygen concentration and high injection pressure
P	Chamber pressure
q	Heat flux

RNG	Renormalization group
RoHR	Rate of heat release
SI	Spark ignition
SRS	Spontaneous raman scattering
TFTHF	Thin film thermocouple heat flux
T	Absolute temperature
T (i,k)	Temperature of the depth i at time k.
T_{gas}	Gas temperature
T_{wall}	Wall temperature
U	Characteristic velocity
V	Chamber volume
cp	Specific heat.
Nu	Nusselt number
Pr	Prandtl number
Re	Reynolds number
ρ	Fuel density
λ	Wavelength
α	Thermal diffusivity
κ	Thermal conductivity
μ	Viscosity

CHAPTER 1

INTRODUCTION

1.1 BACKGROUND AND MOTIVATIONS

Fossil fuel, a primary energy source worldwide, continues to be the main source of energy for transportation. This primary energy consumption grew strongly in 2017 and grew the fastest since 2013 [1]. It is estimated the demand for this fuel will continue to grow by around 20% from 2016 to 2040 [2–3]. Even though demand for almost all types of fuel energy for transportation is increasing, diesel and gasoline fuel will continue to dominate over the next decades (2040) as shown in Figure 1.1.

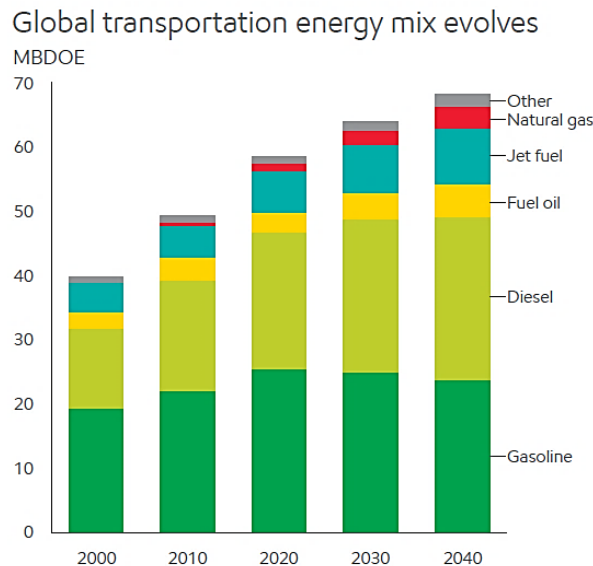


Figure 1.1 Global transportation energy mix evolves [2]

Moreover, global transport emissions have also increased and heavily contribute emissions such as NO_x , particulates and CO. Therefore, to decrease these emissions, and for environmental protection, emission regulations have gradually become increasingly stringent. Examples include the European Euro 1 to 6 standards and the US Tier 1 to 3 standards [4]. This controlled emission is significantly affected by advanced engine technology.

The increasingly strict global emission regulations for vehicles reflect the limited supply of nonrenewable energy resources, which will eventually run out. Therefore, optimization of

engine combustion strategies to improve fuel economy and emissions are an important focus for engine research and development. As a result, along with improvement in fuel economy, recent small-size DI (direct injection) diesel engines have become more efficient and produced low emission because of advanced emission control technologies [5]. However, heat loss is still one of the major factors that contributes to a substantial amount of energy loss for engines. More than half of total heat energy in the internal-combustion engine is lost by cooling through the cylinder wall to the atmosphere and the exhaust gas. As explained by Heywood [6], the conversion from total fuel energy to useful energy output for diesel and SI (spark ignition) engines is only under 40% and 30%, respectively.

The energy balance in the engines is illustrated in Figure 1.2 (a-b). This figure represents the energy losses (in the form of heat) in the engines from the initial applied fuel energy. In a diesel engine, the conversion to effective power is slightly higher than in a SI engine because of the higher compression ratio. The ratio between output work and energy losses is lower. Heat energy loss reduction is essential for improving the thermal efficiency of the engines even though it is impossible to exclude all the losses from the engines. However, it should be possible to decrease heat loss in engines for maximizing the thermal efficiency further.

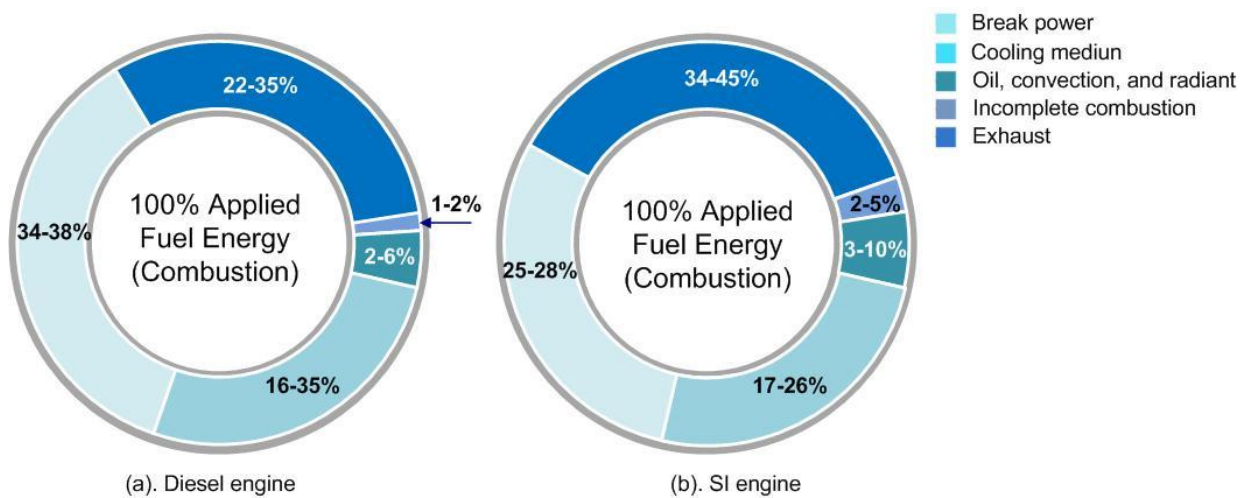


Figure 1.2 Energy balance in the engines [6]

The mechanism of heat transfer inside the combustion chamber is too complex to handle completely. Complex processes affect heat loss to the cylinder wall, such as gas motion by combustion chamber shape, spray-wall impingement from nozzle tip, and turbulence levels

caused by high-pressure injection and supercharging. The influence of spray impingement is extremely important because generally, in combustion chamber design, the fuel spray impinges on the piston cavity before vaporization and mixing are complete. A greater understanding of the fuel spray impingement affect on heat transfer is the primary motivation for this research.

Furthermore, apart from importance of total heat loss from combustion gas to the cylinder wall, understanding the mechanism of local heat flux is also important to know. The general heat flux formula in a diesel engine is shown in below: q is heat flux, h is heat transfer coefficient, T_{gas} is the in-cylinder gas temperature, and T_{wall} is the combustion chamber wall temperature. According to formula (1.1), considering the decreasing value of temporal changes in the heat transfer coefficient and difference between gas temperature and wall temperature is required for decreasing heat flux.

$$q = h (T_{gas} - T_{wall}) \quad (1.1)$$

Many studies have been published in this field, particularly about heat transfer in diesel engines. Because of the need to better understand the mechanism of wall heat transfer with impinging flame on the wall, Senda and a coworker [7]–[10] recently published their study series that analyzes heat loss using a wall insertion-type constant volume vessel (CVV).

However, these studies have not analyzed the proportion of the heat transferred through the wall by the convection of non-combustion evaporating spray. Therefore, this study aims to investigate the characteristics of heat transfer before and during combustion under various experimental parameters. In addition, the wall temperature was controlled (not used by Senda) to investigate the wall heat transfer mechanism from spray flame impingement to the wall surface in CVV under diesel engine-like conditions.

1.2 OBJECTIVES AND APPROACHES

This study aimed at clarifying the heat transfer phenomenon through the combustion chamber wall and was conducted as a basic investigation about the effect of spray flame impingement on transient heat flux to the wall under small diesel engine-like conditions. Several main objectives of this research include:

1. Clarify the effect of flat wall impinging spray flame behavior and heat transfer characteristics under baseline conditions.
2. Investigate the influence of impingement distance on spray flame behavior, transient local heat flux (non-combustion and combustion conditions), and soot formation.
3. Observe the proportion of heat loss between non-combustion and combustion conditions under injection pressure and investigate the effect of nozzle hole diameter transient local heat flux in a combustion condition.
4. Analyze the effect of oxygen concentration on the transient local heat flux characteristics.
5. Explain the combined effect to find the optimum level for decreasing heat loss in a combustion diesel engine-like condition.
6. Confirm that the heat transfer correlation measurement results provided useful insights into the diesel engine combustion.

In this study, spray flame behavior was recorded with a high-speed video camera, and the Mie scattering method was adopted to support the spray impingement illumination photography. To observe soot distribution and local temperature near wall, a two-color pyrometry was applied for natural flame color images. In order to investigate the wall heat loss, three Thin Film Thermocouple Heat Flux (TFTHF) sensors, which measure instantaneous temperature, were mounted on the wall. Numerical simulation was conducted by CONVERGE commercial software to obtain gas temperature at a non-combustion condition to calculate the heat transfer coefficient.

1.3 OUTLINES

To present this work, the dissertation is organized as follows: a review of previous work such as characteristics of spray flame impingement on the wall, the principle of heat transfer, and parametric strategies affected in heat transfer combustion diesel engine are given in chapter 1. Chapter 2 describes the experimental apparatus such as constant volume vessel, fuel injection system, and impingement wall test rig, including the TFTHF sensors. The observation by high-speed video camera, two-color method, heat flux measurement, and data acquisition are also introduced. Chapter 3 describes the spray flame combustion behaviors and transient local heat

flux characteristics under baseline conditions. Chapter 4 shows the effect of impingement distance on the heat flux on diesel spray flame, including the distribution of temperature near a wall and soot emission, respectively, by applying two-color techniques. Chapter 5 deals with the spray flame behaviors of impinging spray and heat transfer characteristics under different injection pressures and nozzle hole diameters. The transient heat flux under different oxygen concentrations is given in chapter 6. Chapter 7 addresses the combination effect on heat transfer and shows the optimum result to decreasing heat transfer on a diesel engine and a heat transfer correlation is expressed in this study. Lastly, general conclusions on spray flame behavior and transient local heat flux in diesel-like conditions and recommendations for future study are summarized in chapter 8.

1.4 REVIEW OF PREVIOUS WORKS

1.4.1 Heat Transfer in Engine Combustion Chamber

Heat transfer is a primary part of the process that causes energy losses in the efficiency of fuel conversion. This heat loss dominates in the energy balance in the engine, affecting engine performance, efficiency, and emissions. In internal combustion engines (ICE), heat loss from combustion gases through the cylinder wall to the coolant strongly influences the thermodynamics of the engine cycle [5].

Figure 1.3 illustrates the schematic of the heat transfer process from hot gas inside the cylinder through the combustion chamber wall to the coolant. Temperature profiles, such as gas temperature (T_g), mean gas temperature (\bar{T}_g), wall temperature (T_w), and coolant temperature (T_c), are also plotted in the figure. The heat flux into the wall has both convective and radiation heat transfer. The heat flux is conducted through the wall and then convected from the wall to the coolant [6]. Based on the Kono et al. [5] most cooling losses take place through the piston wall than cylinder head wall and cylinder block wall.

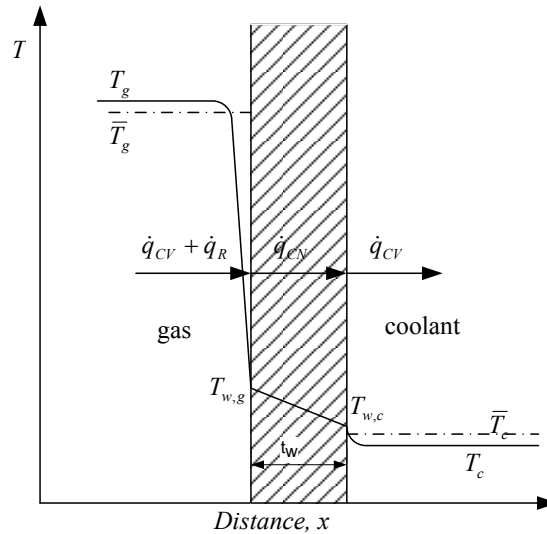


Figure 1.3 Schematic of temperature distribution and heat flow across the combustion chamber wall [6]

1.4.2 Heat Transfer Correlation

According to reviewed studies by Borman and Nishiwaki [11], the first formula for engine heat transfer was introduced by Nusselt in 1923. Nusselt showed that the pressure-temperature term in his correlation was a free convection relationship [12]. Afterward, published literature regarding the gas-to-wall heat transfer process in ICE and a number of correlations have been proposed for calculating the instantaneous heat transfer coefficient [13]–[21].

The several empirical correlations to predict the in-cylinder heat transfer coefficient in ICE were reviewed by Finol and Robinson [22]. The most widely used heat transfer correlations were derived by Woschni [15] and Annand [14]. The basis of these correlations has relied on dimensional analysis for turbulent flow that correlates the Nusselt (Nu), Reynolds (Re), and Prandtl (Pr) numbers. The relationship among Nu , Re , and Pr numbers, which follow those found applied in a turbulent heat transfer equation of the pipe's internal flow or over flat plates [6], [21]. Recently, Kuboyama [23] provided alternative correlations that are applicable to recent diesel engines. As characteristic velocity, mean piston speed is typically used in previously proposed heat transfer equations. Kuboyama used flow induced by fuel injection during the fuel injection period for characteristic velocity. After the fuel injection, character velocity was used in Woschni's equation.

1.4.3 Heat Transfer of Wall Impinging Spray

(1). Wall Impingement Spray Structure

In a small diesel engine, an injected fuel spray impinges on piston cavity surface before vaporization and mixing are complete because of the short distance between the injection nozzle and the wall surface. Furthermore, behavior of spray impingement is important to understand. Figure 1.4 shows the structure and shape of impinging spray.

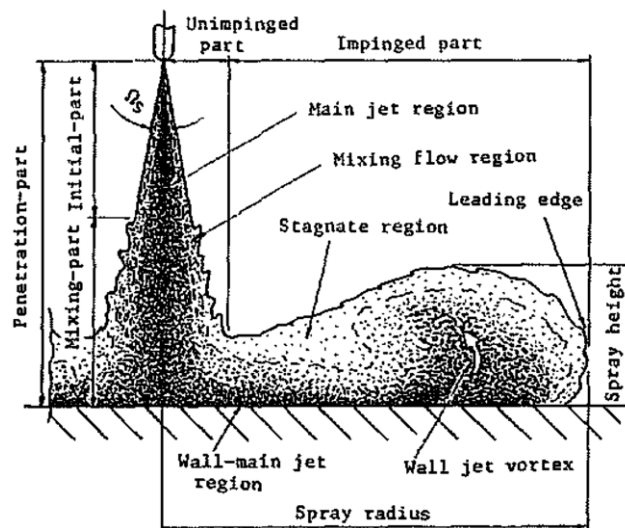


Figure 1.4 Wall impingement structure [24]

The typical structure and regions of interest for the impingement wall have been introduced by Pickett and López [25]. However, more detailed information about structure and shape of impinging diesel spray had been described by Zhao et al. [26] and Katsura et al. [24] as shown in Figure 1.4. They explained that the impinging spray was separated by several parts and regions as follows:

1. Unimpinged part: This part consisted of the main jet region and mixing flow region. In the main region, there was large droplet velocity, momentum, and the droplet density. While in the mixing region, the turbulent mixing occurred between spray, surrounding gas, and the smaller droplet density.
2. Impingement part: This part was divided by several regions. In the wall's main jet region, the spray velocity decreased after impingement and high droplet density appeared along the impingement wall. The stagnate region that occurred at the edge of the impinged part

because of the droplets in the periphery regions were pushed upward and resulted in loss of momentum. The wall jet vortex phenomena appeared at a peripheral region of the impinging spray where the density of droplets was large and turbulent mixing occurred between spray and surrounding gas. Furthermore, droplets were pushed out to the upper by droplets nearer the wall.

3. Initial part: This part lies in the near the nozzle tip exit. The spray has a sharp and clear shape with a spray cone angle (Ω_s).
4. Mixing part: This part lies downstream of the end of the initial part to the impingement wall. In this part, the strong turbulent mixing can be observed.
5. Penetration part: this part is comprised of the initial and mixing parts, where the spray shows similar characteristics to that of steady spray.

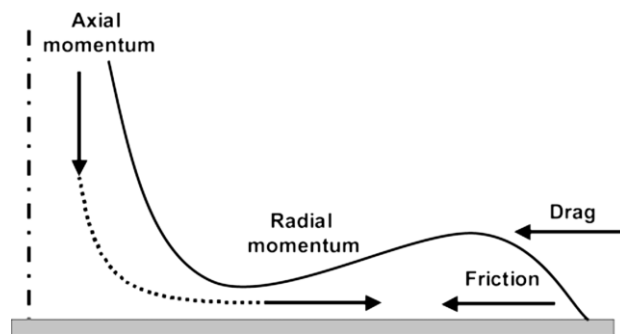


Figure 1.5 Momentum conversion and forces on the impinged spray from the macroscopic point of a view [27]

The information on momentum conversion and forces on the impinged spray introduced by Park [27] is illustrated in Figure 1.5. This momentum conversion and forces on the impinged spray phenomenon was observed from the macroscopic point of view. In the center of the impingement, the axial momentum is converted into the radial momentum. As a result, the radial velocity of the impinged spray is increased by the impingement. The radial velocity is decreased by several kinds of forces, or drag. This drag is caused by the ambient gas and wall friction, the main factors that affect the spray impingement behavior. Studies on velocity distribution after spray impingement have been carried out by Zama et al. [28] by using a time-resolved Particle Image Velocimetry (PIV) technique. As a result, the average radial peak

velocity of the post impingement diesel spray decreased with an increase of ambient gas density and a decrease of injection pressure.

Furthermore, spray impingement to the wall has a significant influence on mixture formation, combustion, and emission. A schematic diagram depicting the conceptual model of diesel jet combustion under an impinging condition during the stabilized diffusion-limited combustion phase was described by Bruneaux [29], as shown in Figure 1.6. During the diffusion combustion phase, the diffusion flame and OH* radical appear at the spray periphery, while the soot particles are confined to the near flat wall region.

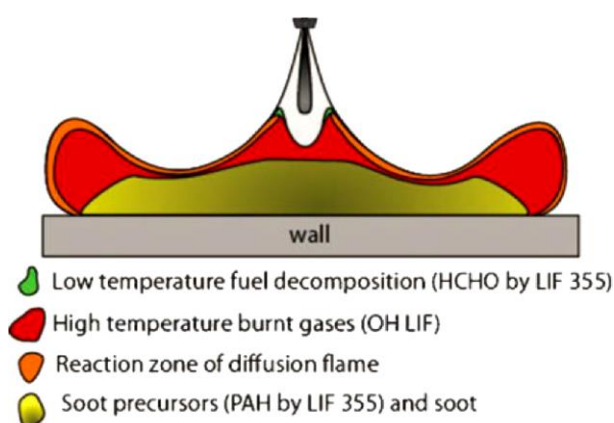


Figure 1.6 Schematic conceptual model of impinging diesel spray under stable diffusion combustion phase [29]

(2). Wall Impingement on Heat Transfer and Combustion Process

There is a long list of publications describing experimental and simulation work with various parameters of heat transfer in diesel engines. Some studies showed that minimizing temperature difference between in-cylinder gas and the combustion chamber wall surface was possible by applying insulation material such as a ceramic coating on the surface [30]–[33]. As a result, the heat loss was reduced. Thus, both exhaust energy and piston work increased, which led to improved thermal efficiency.

Li et al. [34] stated that high injection pressure had a significant effect on the heat loss from combustion gases to the chamber wall. The observations of local heat flux suggested that in case of high injection pressure, the flux reached a peak, which is attributed to an increase in local spray velocity. Another study showed that high injection pressure contributed to increases of flame velocity, flame temperature, and flame contact area because of a fuel injection rate

increase [7]. According to a finding by Dahlström et al. [35], the higher the injection pressure is, the shorter the combustion duration becomes, and thus rate of heat release (RoHR) increases. The factor contributes to higher in-cylinder temperature and thus increased wall heat transfer.

Senda [36], [37] reported that wall impinging spray combustion has a significant effect on the heat transfer characteristics. They found that heat transfer decreases as the droplet impingement frequency increases because of interference between remaining liquid film and impinging droplets. Nakata et al. [10] demonstrated that the heat flux decreased at some spray impingement distance to the wall. Decreasing flame velocity because of the momentum loss by turbulent mixing accounts for this effect.

Bowl geometries and swirl ratio also considered effects on heat loss. Kimura et al. [38] found that transient heat flux in the piston cavity reduced with a larger cavity diameter and higher swirl ratio. On the other hand, a transient heat flux in the piston head was not changed by cavity diameter and swirl ratio. Similarly, Dahlström et al. [35] reported that swirl did not have any effect on heat transfer. This is because of the spray affecting the in-cylinder flow pattern, so the near-wall gas velocity may stay relatively unchanged and thus not alter the convective heat transfer characteristics. Another simulation study reported that in a high compression ratio case, the shallow dish combustion chamber shape with a plateau at the center of the combustion chamber showed potential for heat loss reduction [39]. Kogo et al. [30] demonstrated that the overall heat loss of the new combustion chamber shape (called the taper lip combustion chamber) is approximately 10 J less than the heat loss of the previous reentrant combustion chamber. The effect of gas velocity influences heat loss on the different bowl shape. Perini et al. [40] reported different flow fields at the liner and piston bowl walls leads wall heat transfer to increase significantly at higher swirl ratios. Kono et al. [5] have confirmed that by suppressing the reversed squish flow, the heat flux can be decreased with the tapered shallow-dish cavity compared to the standard cavity.

Engine load and engine speed variations influence heat transfer. Mayer et al. [41] reported that at higher loads the heat release increases because of the larger amount of fuel injected, leading to an increase in the cylinder pressure and mean gas temperature. Thus, an enlarged wall heat flux to the piston occurs. At higher engine speed case, the mean piston

temperature increases because of the intensified convective heat transfer and leads to a heat flux increase.

Tatsumi et al. [8] reported on the heat loss to the wall in a diesel spray flame under various fuel temperature conditions. It was found that key factors to reduce heat loss under various fuel temperatures are the flame flow velocity and flame contact area. Elsewhere, Tatsumi et al. [9] investigated the effect of nozzle hole diameter on heat flux. The controlling factor of the heat loss with respect to the injection hole diameter is the contact area of the flame and duration timing of flame contact.

In a simulation study, applying the exhaust gas recirculation (EGR) rate also considered decreasing flame temperature distribution on heat loss. Comparing the single injection results at a different EGR rate, it was confirmed that the heat flux was decreased at a higher EGR rate [42]. With an increasing EGR rate, the oxygen concentration in the fuel/gas mixture decreases and the specific heat of the cylinder increases and leads to a reaction rate decrease. Further, in-cylinder pressure and combustion decrease [43]. It was evident with an experimental study by Kuboyama [44] that the results show that EGR in a diesel engine suggests that it has the effect of reducing wall surface heat loss.

Spray flame impingement to the wall is also of interest in combustion and emission. Many studies have been conducted on the impinging spray flame on the wall. In those studies, researchers [25], [45] focused on the characteristics of combustion and soot formation. Li et al. [46] investigated the OH* chemiluminescence, flame temperature, and soot emission of flat wall impinging flame and free flame. The result showed that unburned hydrocarbon emission and high soot formation increased when impingement occurred. Wang et al. [47] produced similar results. For example, impingement flame caused deterioration of soot formation when compared to the free flame. Furthermore, Dec and Tree [48] also concluded that spray/wall interaction may increase particulate and unburned hydrocarbon emissions and reduce thermal efficiency. However, Picket and Lo'Pez [25] reported that soot formation was improved by impingement, because it enhanced combustion when compared with free flame.

(3). Modeling of Wall Impingement

Various prediction models for spray wall interaction have been developed in the last thirty years. Naber and Reitz [49] have proposed a submodel on droplet-wall interaction at impingement, called stick model, a reflect model (droplets rebound), and liquid jet analogy model (wall jet), based on the Weber number of impinging droplets. Bai and Gosman [50] have classified the impingement model, i.e., dry wall, which consists of a stick, spread, and splash. Another one is a wetted wall, which consists of rebound, spread, and splash. Senda et al. [51], [52] developed a spray wall interaction model based on his experimental study on droplet impingement. They developed the submodel in low-wall temperature and high-wall temperature conditions, which included fuel film formation on the wall, its breakup process because of droplet impingement, and the dispersion process of breakup droplets. Furthermore, they developed the sub model based on several of their experimental results [53]. A good review of spray-wall impact relevant to IC engines addressed the rationale of describing spray-wall interactions based on the knowledge of droplet impacts [54], prediction models on wall-impingement criteria, post-impingement characteristics of single drops, and external and internal structures of the spray after the wall impact [55].

Criteria of droplet wall interaction can be classified for different conditions that are shown schematically in Figure 1.7 [49]: (a). Stick: in which the impinging droplet adheres to the wall in nearly spherical form when the impact energy is very low. (b). Rebound: in which the impinging droplet bounces off the wall after impact. In a dry wall case, contact between the liquid droplet and the hot surface is prevented by the intervening vapor film. On a wetted wall, the air film trapped between the droplet and the liquid film causes low energy loss and results in bouncing. (c). Spread: the impinging droplet spreads out to form a wall film for a dry wall or merges with the preexisting liquid film for a wet wall. (d). Boiling-induced breakup: the droplet, even at very low collision energy, disintegrates because of rapid liquid boiling on a hot wall. (e). Rebound with break-up: the droplet bounces off a hot surface, accompanied by breakup into two or three droplets. (f). Break-up: the droplet first undergoes a large deformation to form a radial film on the 'hot' surface, and then the thermo-induced instability within the film causes the fragmentation of the liquid film in a random manner. (g). Splash: following the collision of

a droplet with a surface at a very high impact energy, the jets become unstable and break up into many fragments.

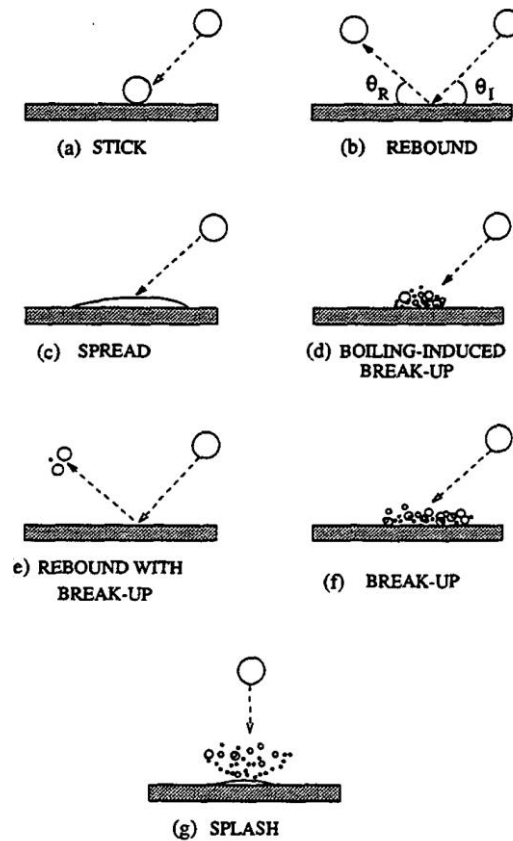


Figure 1.7 Schematic of different impact regimes [49]

The existence of these impingement regimes is governed by a number of parameters characterizing the impingement conditions: droplet velocity, size, temperature, incidence angle, fluid properties such as viscosity, surface tension, wall temperature, surface roughness, and, if present, wall film thickness and a gas boundary layer at the wall.

They classified the impinging droplet behavior based on the Weber number into three types as shown in Figure 1.8 [51]. (I). $We < 80$: Because there was no impinging droplet breakup into film, the impinging droplets were stuck on the wall, and leads fuel film on the wall surface occurred. (II). $80 \leq We < 600$: In this We range, the remaining liquid fuel on the wall or the impinging droplet breaks up into relatively large droplets due to the successive droplet impingement. (III). $We \geq 600$: When the We number of the droplets were larger than 600, the fuel film or the impinging droplet breaks up into small droplets.

	Breakup Form	d_{10} / d_i	V_b / V_i	Range in We No.
I	I non-breakup (into film)	—	—	$We < 80$
II	II large breakup	0.3	0.3	$80 \leq We < 600$
III	III small breakup	0.1	0.5	$We \geq 600$

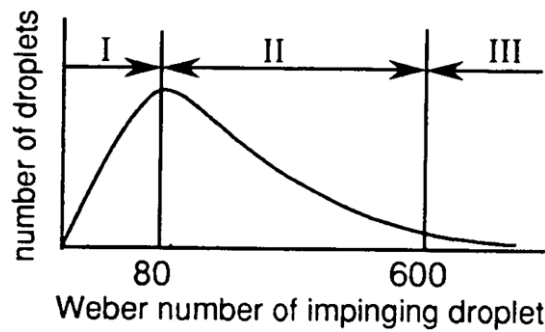


Figure 1.8 Fuel film breakup model by impinging droplets after film formation [51]

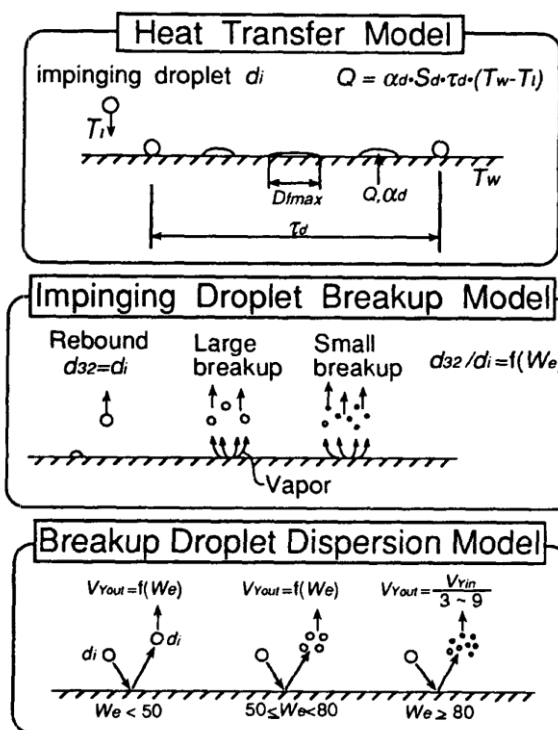


Figure 1.9 Fuel film breakup model by impinging droplets after film formation [51]

Figure 1.9 shows their general models for heat transfer, impinging breakup, and droplet dispersion [51]. Heat transfer model: the impinging droplet spreads as a fuel film in a radial direction on the wall for a certain period, and thereafter the film shrinks and rebounds from the

wall without breaking up, or it breaks up into small droplets. In this case, where the temperature of the impinging droplet (T_t) is lower than that of the wall surface (T_w), heat is transferred from the surface to the film formed on the surface during the residence time (td) of the film. The heat heats the film and evaporates it. Impinging droplet breakup model: the breakup resulting from the boiling phenomena at the liquid–solid interface and the Sauter mean diameter of breakup droplets from the liquid film on the wall were dependent upon both the Weber number of the impinging droplet and the surface temperature (T_w). Breakup droplet dispersion model: an impinging droplet breaks up into small droplets in a higher Weber number region, and they must be dispersed in both upward and radial directions.

1.4.4 Optical Diagnostic Technique for Diesel Spray

Optical diagnostic techniques are one of the best ways to provide invaluable insight and detail information for a better understanding the nature of diesel engine. For the last decades, a lot of investigations study on some quantitative spray and flame parameters during the fuel-air mixing and combustion process have been done in different all kinds of optical techniques development. Different kinds of optical techniques for mixture formation measurement in IC engine have done reviewed by Zhao and Ladommatos[56], [57]. Each measurement technique gives some valuable insight into one of the fundamental processes in spray formation. Their review of various techniques for observation is summarized by Li [45] as in Table 1.1.

The Mie scattering method was used to measure the liquid-phase spray angle and penetration [58], [59]. In other words, the Mie scattering was applied to measure liquid fuel behavior [60]. Furthermore, the Mie scattering method was used to measure droplet size and concentration by Hodges et al. [61] by applying the ensemble-scattering polarization ratio method. Similarly, 1-d and 2-d Mie scattering were applied to visualize the distribution of the fuel droplets [62]. According to the Lorenz-Mie theory, the intensity of Mie scattering is determined by the square of the droplet diameter and the droplets' concentration when droplets remain spherical and droplet diameter is larger than 1 μm [64].

Table 1.1 Summary of optical techniques for in-cylinder mixture formation measurement

Technique	Applications	Advantages	Limitations
Mie Scattering	Liquid fuel distribution	Simple setup	Sensitive to large droplets
Schlieren and shadowgraph	Observations of Overall spray	Simple setup	Sensitive to both liquid and vapor phase
LRS	Density measurement Vapor concentration	Strong signal Simple setup 2-D imaging	Interference from Mie and spurious scattering Limited to gaseous fuel
SRS	A/F ratio Residual gas fraction	Multi-species detection multi-point detection Most accurate A/F readings Unaffected by windows fouling	Weak signal
LIF	Fuel concentration	Strong red shifted signal 2-D image of fuel	Quenching at high pressures Difficult to calibrate
FARLIF	A/F ratio	Direct A/F measurements 2-D images of fuel	Careful calibration required High pressure operation
LIEF	Fuel vaporization & atomization	2-D imaging Simultaneous detection of Vapor and liquid	Quenching by oxygen
LEA (LAS)	Fuel vaporization & atomization	Quantitative concentration measurements Droplet size information	Poor spatial resolution

Schlieren and shadowgraph techniques were used for imaging and measuring phenomena in transparent media [63], [64]. To understand highly transient combustion phenomena such as diesel spray injection and combustion, shadowgraph/schlieren techniques have been used for flow visualization of reacting and nonreacting systems [65]–[67]. These optical diagnostics can simultaneously observe the vapor phase and liquid phase of spray. The details of Schlieren and Shadowgraph techniques have been described by Settles [63]. Researchers [65], [68], [69] also using these techniques to identify the spray boundary under evaporating conditions. The optical setup for Mie and schlieren diagnostics is shown in Figure 1.10 [65].

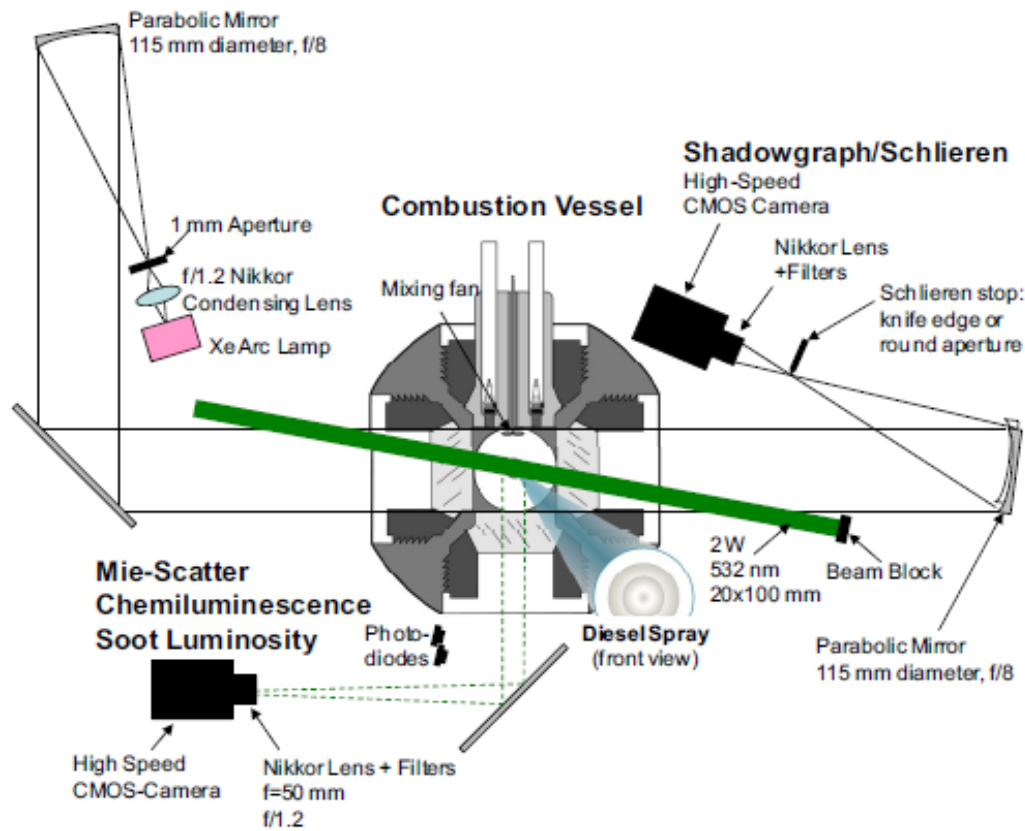


Figure 1.10 shows the optical setup for Mie and schlieren diagnostics [65].

The laser Rayleigh scattering (LRS) technique was applied to a vaporizing diesel spray to show the transient mixing and attainment of a quasi-steady state. It is also used to determine the equivalence ratio in the premixed-burn region of a diesel spray [70]. Zhao and Hiroyasu [71] have reviewed the applications of LRS to combustion diagnostics. Espey et al. [72], [73] used a planar LRS technique successfully to obtain the quantitative images of fuel vapor concentration in an optical single cylinder direct injection diesel engine under motored and firing conditions.

Spontaneous Raman scattering (SRS) is a technique to identify molecular species, measure gaseous species concentrations, and calculate air/fuel ratio. Hoffmann et al. [62] determined accurately by using the SRS technique how to measure the quantitative air/fuel ratio and temperature in the vapor phase before the combustion. The SRS technique was applied, enabling the quantitative measurement of the local air/fuel-ratio along a line of a few millimeters by Egermann et al. [74]. The results clearly showed an additional air entrainment

into the wall jet and leaner air/fuel ratios in that location. Furthermore, the mixture formation significantly improved by an increasing injection pressure. Use of the SRS technique successfully applied in modern diesel injection system like diesel engine condition can be found in studies by several researchers [75]–[79].

Laser-induced fluorescence (LIF) is an electronic absorption and emission process that produces relatively strong signal intensity with high spatial resolution [56]. The method was used in the previous studies to see in-cylinder fuel distribution [80], fuel film in the piston-top under reacting combustion condition [81], and NO measurement in diesel spray flame [82] or emissions from HCCI engines [83], [84]. Eventually, Bruneaux [85] clarified combustion structure of free and wall impingement diesel spray using the information given by simultaneous LIF techniques under the stable diffusion combustion phase.

Laser-induced exciplex fluorescence (LIEF) is a method to quantitatively measure the vapor phase and liquid phase of spray simultaneously in engines since its development by Melton [86]. Numerous studies [51], [85]–[90] exist for measuring the structures of concentrations of the liquid phase and the vapor phase by applying LIEF. They provide detailed information on the fuel mixture formation process and give some fundamental principles of free and imping spray evolution.

The laser absorption-scattering (LAS) technique is an available method to detect vapor concentration in the presence of liquid fuel droplet in a spray [91]. This technique is based on the principle that the optical thickness of absorption light attribution to the attenuation by droplets scattering and vapor absorption, and the optical thickness of transmitted light only contributed by droplet scattering. LAS technique was firstly proposed by Chraplyvy [92], who measured vapor and liquid scattering, respectively. During the past twenty years there has been extensive research to analyze the mixture formation processes in the diesel engine [93]–[97]. Studies have provided the information of quantified liquid and vapor mass concentration, entrained air concentration, and equivalence ratio.

1.5 SUMMARY

In order to determine the reduction of heat loss from combustion gas to the cylinder wall, it is necessary to understand the heat transfer mechanism for maximizing the thermal efficiency

of the engine, especially in small-size diesel engines. Therefore, the target of this study is to clarify the effects of impingement distance, injection pressure, oxygen concentration, nozzle hole diameter, and their combined effect on impinging spray flame behavior, soot formation, and heat transfer characteristics.

This chapter first gives the background and employed approaches of this study. Then, the previous works of heat transfer principle, heat transfer in diesel engines, and a spray impingement model are reviewed. Finally, the optical diagnostics applied in this research are simply introduced.

CHAPTER 2

EXPERIMENTAL APPERATUS, MEASURING METHODS, AND EXPERIMENTAL CONDITIONS

2.1 HIGH-PRESSURE AND HIGH-TEMPERATURE CHAMBER VESSEL

Experiments were performed in a high-pressure and high-temperature chamber vessel with Denso injector as shown in Figure 2.1. The vessel has four side windows. Two of them were used for installing an injector and a spray impinging wall plate facing each other. Others were provided for visualization. In order to simulate an engine-like thermodynamic environment, an electric heater was installed at the bottom of the chamber, and pressurized hot air was supplied through an Electric Muffle Furnace. This preheater equipment was produced hot air temperature up to 973 K, which it can be heated to 753-773 K when hot air entered into the combustion chamber vessel. The internal and external surfaces of the chamber was covered by the thermal insulator to avoid the heat conduction and maintain the stable environment. The chamber pressure was manually operated, whereas the chamber temperature was controlled by a volt slider for the heater. Water cooling galleries were installed around the glass windows and the injector holder to avoid overheating. In order to measure ambient temperature, three K-type thermocouples were fitted near the wall and remaining one K-type thermocouple was fitted at a distance of 5 mm under the nozzle tip, which was placed between nozzle tip and wall. Diesel fuel was injected into the chamber when the ambient temperature was achieved at the target temperature measured by thermocouple placed in middle of nozzle tip and wall. It should be noted that the temperature difference of thermocouples became within 5 K.

A heat flux measurement was done a little later after hot gas feed for avoiding turbulence in the vessel. Diesel fuel was injected into the chamber when temperature difference of the thermocouples became within 5 K. Fuel, which was supplied from a common rail system, was injected through a single hole nozzle injector controlled by an Electronic Control Unit (ECU). Injection quantity and timing was controlled by a delay pulse generator (Stanford Research Systems DG645). Injection pulse had been calibrated by the injection rate measurement previously.

According to Wakisaka and Azetsu [98], shapes of fuel injection rate influences on the combustion and thus emission formation. Figure 2.2 shows an averaged result of ten times injection rate measurement of the single-hole injector by Zeuch method by using Ono Sokki Co. Ltd, FJ-7000. The injection rates of 80, 120 and 180 MPa injection pressure under nozzle hole diameter of 0.133 mm and 0.133 and 0.122 mm under 120 MPa injection pressure are shown in Figure 2.2 (a) and (b), respectively. In order to maintain the same fuel quantity of 5 mm³, injection durations were changed by the pressures and nozzle holes diameter. Bower and Foster [99] was performed and confirmed that the Zeuch method is more accurate for measuring injected volume. The Zeuch method is a measurement method based on the pressure measurement in an airtight chamber in which diesel fuel is contained. When fuel is injected into

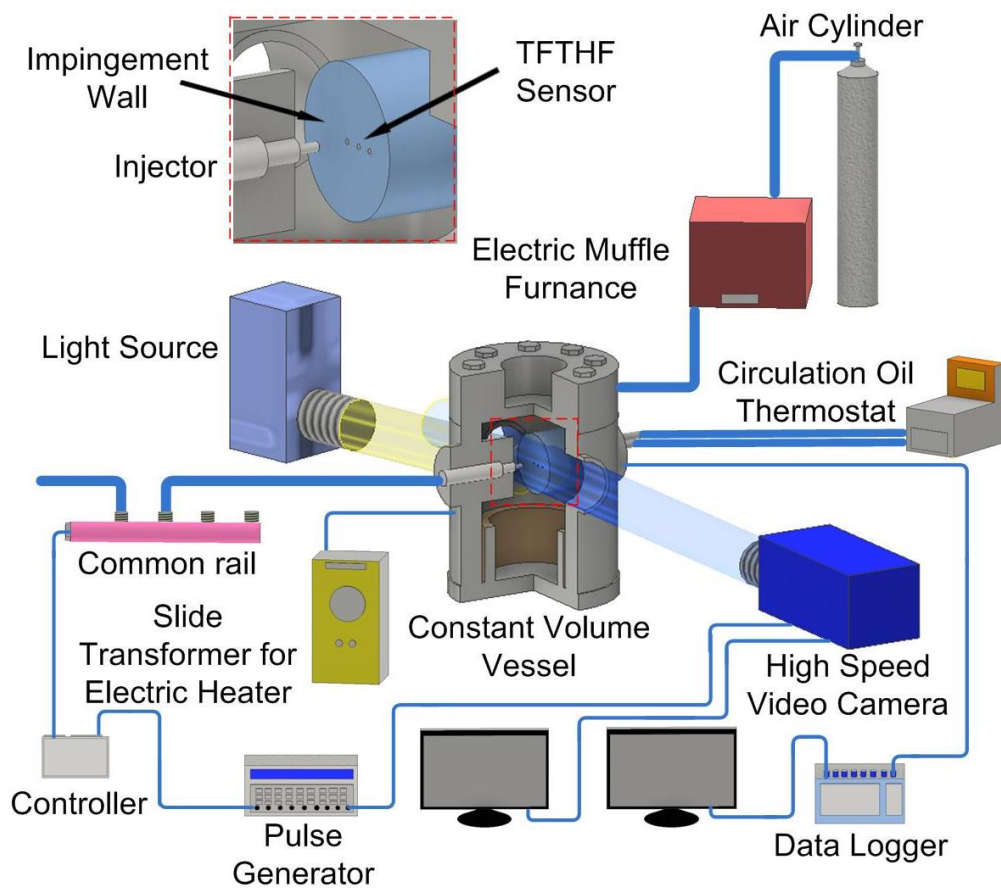


Figure 2.1 Experimental apparatus

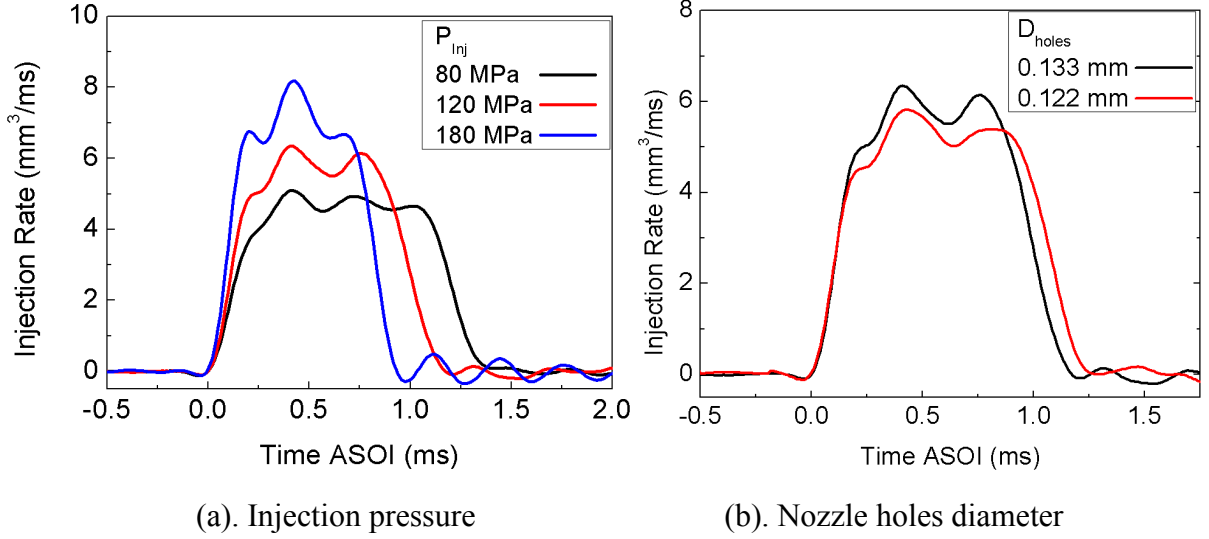


Figure 2.2 Injection rates

the chamber, it induces pressure rise in proportion to the fuel mass injected. The derivative of the pressure with respect to volume produces the injection rate profile.

The equation for the Zeuch injection rate measuring method is derived based on the conservation of mass. By inserting the fuel bulk modulus, the governing equation can be written as follows.

$$\frac{dm}{dt} = \rho \cdot \frac{V}{K} \cdot \frac{dP}{dt} \quad (2.1)$$

Where m is mass of fuel, ρ is fuel density, V is chamber volume, K is bulk modulus of the fuel, and P is chamber pressure. Regarding this equation, the mass injected rate is proportional to the fuel density, chamber volume, and rate of chamber pressure rise and inversely proportional to the fuel bulk modulus. The fuel bulk modulus is a function of pressure and temperature, which it is defined as the change in pressure due to the injected volume of fuel multiplied by the initial chamber volume. The bulk modulus is an analogous to the modulus of elasticity for metals [99].

$$K = V \cdot \frac{dP}{dV} \quad (2.2)$$

However, concerning the chamber design, the volume must be sized so that the chamber pressure rise is within the appropriate limits (1-3 MPa) for the desired volumetric injection rate [99].

2.2 IMPINGEMENT WALL

Injection direction was set perpendicular to the impingement wall. The impinging distances between the nozzle tip and the impingement wall were set at 30, 40, and 50 mm with spacers as shown in Figure 2.3. Spray tip penetration is defined as summation of axial (D_{imp}) and radial penetrations ($S_{wall}/2$). The flat wall was made of stainless steel which has a thickness of 7.3 mm. Three micro heat flux sensors were mounted on the impinging surface side of the wall with high-temperature adhesive with 10 mm distance radially from the center of the wall. The back side of the wall plate was cooled by oil in order to form one-directional heat flow across the wall. The cooling oil temperature was kept constant by a thermostatic oil bath.

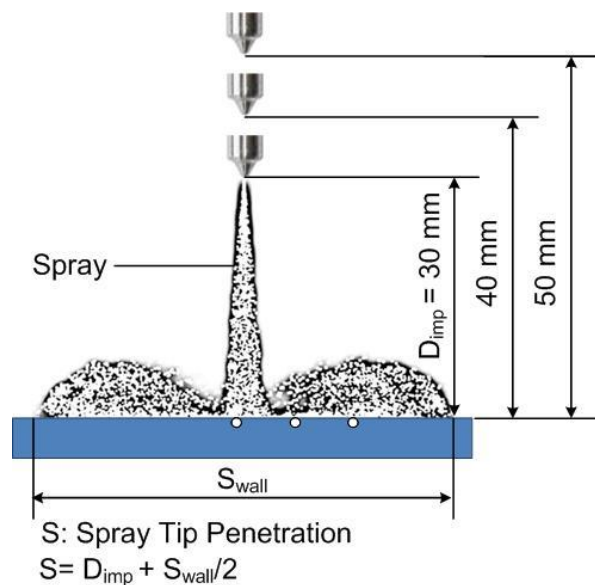


Figure 2.3 Spray impingement distances

2.3 OPTICAL MEASUREMENT TECHNIQUES

2.3.1 Mie Scattering Method

Mie scattering method was adopted to support the spray impingement illumination photography. A Xenon lamp was applied for the source of scattering light. The light from Xenon lamp illuminated the spray in the combustion chamber through the sideward transparent quartz window. Figure 2.4 shows the optical set-up of Mie scattering method. A high-speed video camera (nac Image Technology Inc, HX-3) was used to record the spray behavior. The camera setting for experiments was as follows: imaging speed of 20,000 frame speed per second

(fps) and resolution of 320 x 448 pixels, which each represent 5 pixels per mm. This Mie scattering method was used in non-evaporating and non-combustion evaporation conditions to detect spray behavior. As original images contain elements other than the spray in these conditions, we removed such extra elements by image processing. This resulted in high-quality spray images

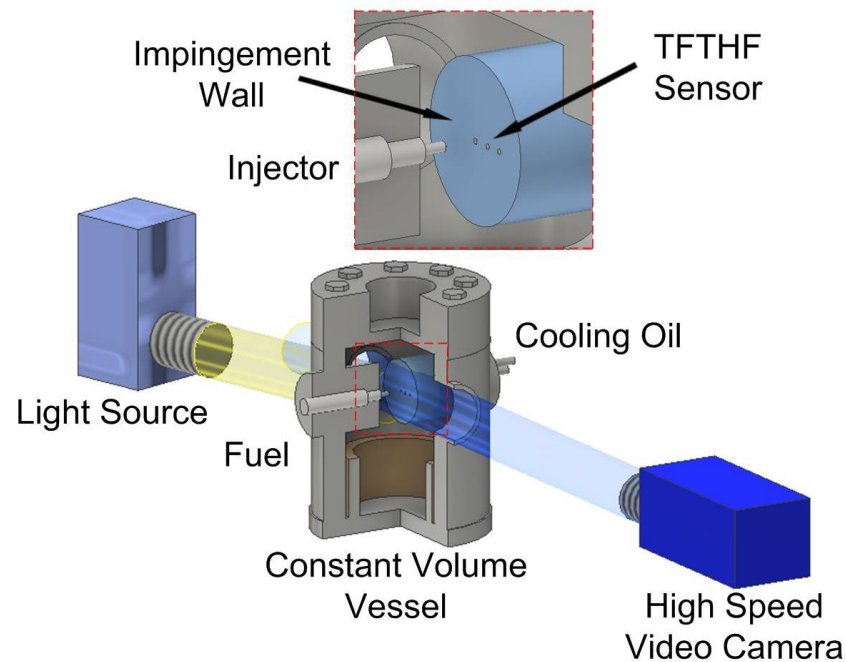


Figure 2.4 Optical set-up of Mie scattering method

2.3.2 Natural Luminosity Recording System and Two-Color Pyrometry

Generally, rich mixture of fuel and air leads to soot formation with luminous flame. Natural luminosity mainly comes from soot incandescence in diesel flame, which was related to temperature and soot volume fractions. The natural flame luminosity measurements were carried out in this research. A high-speed video camera and the camera setting were similar with non-combustion case. A flame color image consists of red, blue, and green colors. However, since red was a dominant flame color, we used it for luminosity analysis. Flame luminosity was calculated by the summation of red color value for each pixel.

(1). Principle Two-Color Pyrometry

To observe local temperature near the wall and soot distribution, a two-color pyrometry was applied for the natural flame color images. Detail discussion of the principle of two-color

pyrometry can be found in Matsui and his coworkers [100], [101], [102]. As reported in Ahn et al. [102], the principle of the two-color method utilizes radiation intensity from soot particles through the combustion process in order to calculate the flame temperature.

According to the Wien's equation, the monochromatic radiance of the flame $N(\lambda, T)$, which can be expressed as:

$$N(\lambda, T) = C_1 \lambda^{-5} \exp\left(-\frac{C_2}{\lambda T_a}\right) \quad (2.3)$$

Where λ is the wavelength, T is absolute temperature, C_1 and C_2 are the first Planck's constant and the second Planck's constant respectively, and T_a is the luminous temperature. When ε_λ denoted the monochromatic emissivity of the flame, Eq. (2.3) can be rewritten.

$$N(\lambda, T) = \varepsilon_\lambda C_1 \lambda^{-5} \exp\left(-\frac{C_2}{\lambda T}\right) \quad (2.4)$$

If the emissivity of the luminous flame ε_λ is given by Hottel-Broughton equation [103], it can be expressed by Eq (2.5).

$$\varepsilon_\lambda(\lambda, T) = 1 - \exp\left(-\frac{KL}{\lambda^\alpha}\right) \quad (2.5)$$

Where K is the absorption coefficient, nearly proportional to the number density of soot particles, L is the path length of the flame in the direction of the light axis of the flame detection, and α is a constant within a specific range of wavelength.

Combining Eq (2.3), Eq (2.4) and Eq (2.5), it can be written as Eq (2.6):

$$KL = -\lambda^\alpha \ln \left[1 - \exp \left\{ -\frac{C_2}{\lambda} \left(\frac{1}{T_a} - \frac{1}{T} \right) \right\} \right] \quad (2.6)$$

If there are two specific wavelengths λ_1, λ_2 that are measured simultaneously, the value KL which is proportional to the integrated soot concentration can be eliminated:

$$\left[1 - \exp \left\{ -\frac{C_2}{\lambda_1} \left(\frac{1}{T_{a1}} - \frac{1}{T} \right) \right\} \right]^{\lambda_1^{\alpha_1}} = \left[1 - \exp \left\{ -\frac{C_2}{\lambda_2} \left(\frac{1}{T_{a2}} - \frac{1}{T} \right) \right\} \right]^{\lambda_2^{\alpha_2}} \quad (2.7)$$

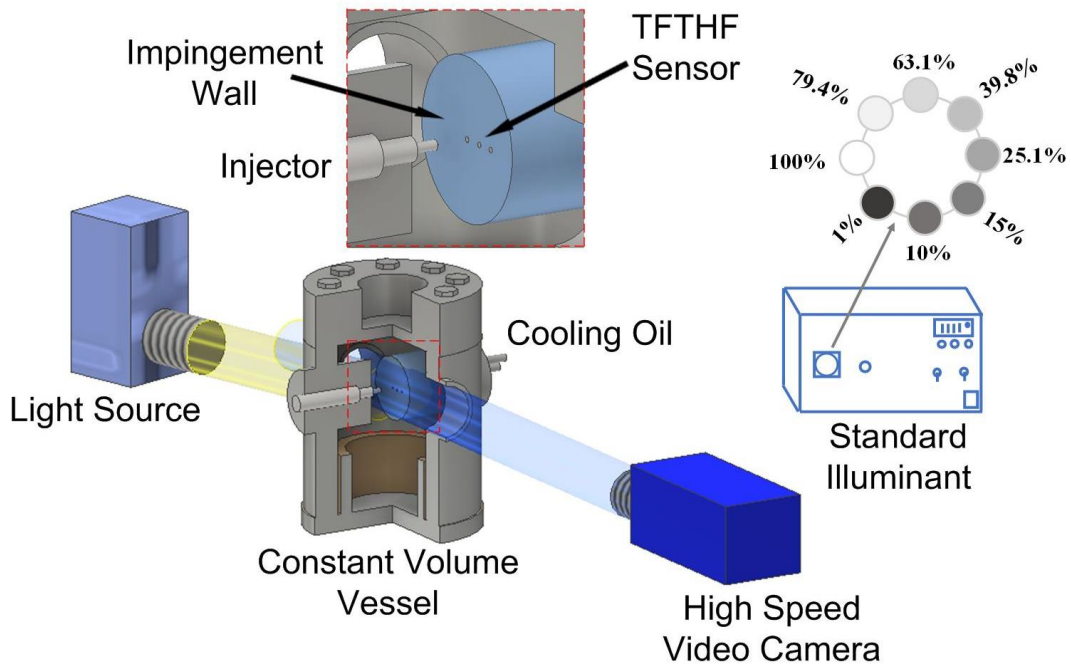


Figure 2.5 Experimental setup for natural luminosity and two-color pyrometry

By substituting the brightness temperature of the flame T_{a1} and T_{a2} at two specific wavelengths λ_1 and λ_2 , which can be obtained according to the calibration data, the actual temperature and the KL value can be calculated. Data analysis was performed by nac Image Technology's "Thermias" as two-color pyrometry software. As a result, the flame temperature and KL factor were two-dimensional with line-of-sight information.

(2). Calibration of Two-Color Pyrometry

The basic principle of calibration of two-color pyrometry was reported by Ahn et al. [102]. Recently, the calibration was explained details by Li et al. [104], [45]. A standard light illuminant was used for the calibration of the two-color method. The Eight neutral density filters with different transmittance are rotating before the standard illuminant. In the optical set-up, standard light was placed at the same distance with the flame to the camera. The Red, Green and Blue channels could be obtained from high-speed video camera. However, we select the red and blue channels for two-color calculation because these two channels have spectral responses with insignificant overlap according Svensson et al. [105].

According to the Eq (2.4), the power of monochromatic emissive after passed through the neutral filter with transmittance of τ_i can be expressed as, [104]

$$N(\lambda, T) = \tau_i \varepsilon_\lambda C_1 \lambda^{-5} \exp\left(-\frac{C_2}{\lambda T}\right) \quad (2.8)$$

Combining Eqs (2.3) and (2.8), it can be written as Eq (2.9):

$$\frac{1}{T} - \frac{1}{T_a} = \frac{\lambda}{C_2} \ln(\tau_i \varepsilon_\lambda) \quad (2.9)$$

When the transmittance is 1, the temperature T will be received by using a thermodetector and then T_a will be calculated through equation 1. The empirical correlation of $\varepsilon_\lambda = a_0 + a_1 \lambda + a_2 T + a_3 \lambda T$ is used in this calculation.

The luminous intensity I perceived by camera sensor could be expressed as:

$$1 = a \tau_i \varepsilon_\lambda C_1 \lambda^{-5} \exp\left(-\frac{C_2}{\lambda T}\right) + b \quad (2.10)$$

Where a and b are constants which depend on the camera sensor. Taking the logarithm at both sides of Eq (2.10) gives,

$$\ln(1 - b) = \left(-\frac{C_2}{\lambda T}\right) + \ln(a \varepsilon_\lambda C_1 \lambda^{-5}) \quad (2.11)$$

According to this equation, the relationship between $\ln(1-b)$ and $\frac{1}{T}$ follow linearity when the illuminant happens. The slope equals to $-\frac{C_2}{\lambda}$, in reverse, the effective wavelength of this system could be defined as follows:

$$\lambda_{effective} = \left(-\frac{C_2}{slope}\right) \quad (2.12)$$

In this experiment, three effective wavelengths of color camera could be acquired:

$$\lambda_{red} = 577.38 \text{ nm}, \lambda_{green} = 541.12 \text{ nm}, \lambda_{blue} = 517.82 \text{ nm}$$

When the source of the light is a standard illuminant, the ε_λ in will becomes the value of 1, and the T will be replaced by T_a . By using Eq 2.12, results output from camera that recorded eight kinds of luminous intensity which are attenuated by eight kinds of neutral filters then the calibration line as shown Figure 2.6 will be obtained.

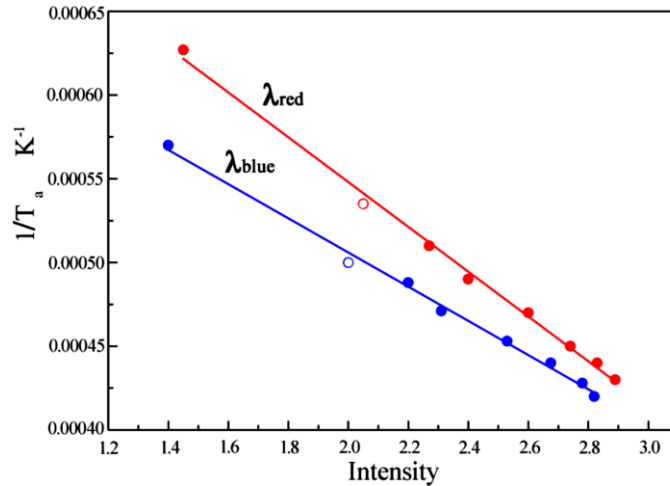


Figure 2.6 Calibration graph sample.

Figure 2.6 shows the vertical axis represents the black body's temperature and the horizontal axis represents the actual intensity $\ln(I-b)$ which is received by camera sensor and b is a constant of the camera. From this calibration, the temperatures of black body at two effective wavelengths are received, which the actual temperature could be calculated by applying Eq (2.7).

2.4 HEAT FLUX SENSOR AND MEASUREMENT

2.4.1 Thin Film Thermocouple Heat Flux Sensor

Three Alumel/Chromel Thin Film Thermocouples Heat Flux (TFTHF, Medtherm 10702B) sensors were mounted to obtain instantaneous surface heat flux of the wall. To detect the surface temperature of the wall accurately, the sensors were installed as close as possible to the wall surface, approaching exactly from the wall surface. The sensors location and its arrangement as shown in Figure 2.7.

The sensor consists of two thermocouple sensors. One is a surface temperature sensor and the other is an inner temperature sensor. Diameter of the sensors is $\varnothing 1.55$ mm, and distances between thermal contacts (surface and inner) is 3.30 mm. The sensors were radially located with 10 mm distance each other as shown in Figure. 2.7. Positions of the sensors are designated as Position1 (center of wall impingement), Position2 (10 mm from center) and Position3 (20 mm from center).

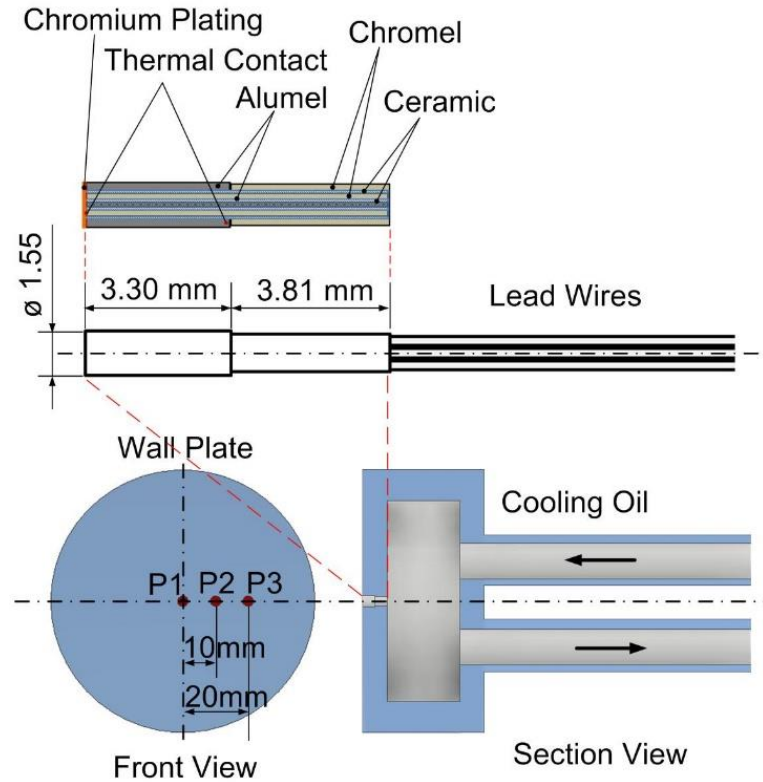


Figure 2.7 Thin film thermocouple heat flux sensor and sensor arrangement.

2.4.2 Heat Flux Measurement

Because direct measuring of transient heat flux is impossible, we identified heat flux applying one-dimensional non-steady heat conduction equation using two measured temperatures by one sensor as boundary conditions. The equation is written as a second order partial differential equation (2.13).

$$\frac{\partial T}{\partial \tau} = \alpha \frac{\partial^2 T}{\partial x^2} = \frac{\kappa}{c_p \cdot \rho} \frac{\partial^2 T}{\partial x^2} \quad (2.13)$$

Where T is temperature, τ is time, x is location of thickness direction, α is thermal diffusivity, κ is thermal conductivity, c_p is specific heat, and ρ is density. We solved the equation by using finite difference method with measured surface and metal inner temperatures of each TFTHF sensor as boundary condition, and obtained transient temperature distribution in the wall. Divide from the wall surface of the thermocouple to the inside wall surface, divide it into n , use $i = 0$ for the wall surface and $i = n$ for the inside wall surface. The forward difference type differential equation is used from equation (2.14) and the following equation is derived.

$$T(i, k + 1) = T(i, k) + \theta x \{T(i + 1, k) + T(i - 1, k) - 2T(i, k)\} \quad (2.14)$$

Where i indicates a step in the depth direction, k indicates a step in the time direction, and $T(i, k)$ indicates the temperature of the depth i at time k . Approximate the time derivative in Equation (2.14) with a forward difference and Eq. (2.15) is stability criteria of which should not exceed the value imposed on by the following.

$$\theta x = \alpha \frac{\Delta \tau}{(\Delta x)^2} \leq \frac{1}{2} \quad (2.15)$$

The measured temperatures at the wall surface and inside wall of the TFTHF sensor are given to the temperatures at $i = 0$ and n , and Δx and Δ are division widths in the step direction and the time direction, respectively by the boundary condition. And then we calculated non-steady surface heat flux component by using inner wall temperature distribution result with the following equation.

$$\begin{aligned} q(k) &= h (T_{flame} - T_{wall}) \\ &= \frac{\kappa}{\Delta x} \{T(0, k) - T(1, k)\} + C_p \rho \frac{\Delta x}{2} \frac{T(0, k+1) - T(0, k)}{\Delta \tau} \end{aligned} \quad (2.16)$$

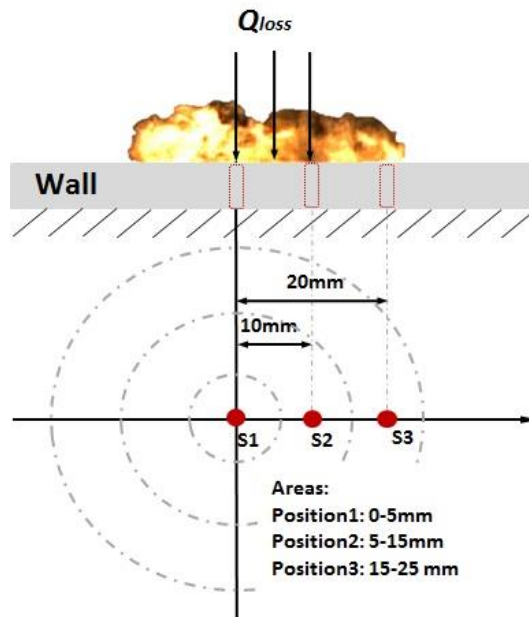


Figure 2.8 Areas at wall surface

Total heat loss was calculated by integrating the heat flux with concentric area and time. In area integration, heat flux affecting areas were defined as concentric circles of 0-5 mm for Area1, 5-15 mm for Area2, and 15-25 mm for Area3, respectively as shown in Figure 2.8. The heat fluxes measured were used as their representatives, as reported by Tatsumi et al. [7].

Furthermore, so as to predict heat transfer coefficient (h) by CFD (computational fluid dynamics) precisely, we need accurate h experimentally. Steady state heat transfer coefficient is expressed in equation (2.17), but this relation is also applicable for the transient heat transfer.

$$h = \frac{q_{wall}}{T_g - T_{wall}} \quad (2.17)$$

Where T_{wall} is instantaneous local temperature and q_{wall} is transient local heat flux, both of them are obtained from TFTHF sensor measurement. T_g is gas temperature. To find an accurate h , we need to determine the gas temperature. However, gas temperature during combustion varies both spatially and temporally and it is difficult to determine adequate value. Whereas gas temperature at non-combustion is almost constant throughout the injection. According to our CFD calculation, however, vaporized spray temperature near the wall surface was around 60 K lower than the ambient temperature at evaporation condition. It decreased to 804, 808 and 810 K for injection pressure of 80, 120 and 180 MPa, respectively. Therefore, we used predicted spray temperature as a mainstream temperature for heat transfer calculation. The CFD solver CONVERGE software was used in this study. Turbulence model employed was renormalization group (RNG) k- ϵ turbulence model, with wall film and wall heat transfer models by O'Rourke and renormalization group Amsden. Modeling, initial and boundary conditions were conducted same as an experimental study. Then to validate the results, comparison with experiment is made as shown in appendix Figure 5. After validating, we are able to use the data for calculation.

The local heat flux increase came from convection by turbulent spray arrival both combustion and non-combustion cases [106]. Convection is dominant for the wall heat transfer by impinging spray flame. In non-combustion case, we used temperature near wall obtained by simulation at non-combustion condition as the gas temperature for the calculation. By this approximation, we were able to find relatively precise value of h . In combustion condition,

there exists large temperature gradient distributed in flame [106]. Then we used mean flame temperature which was obtained from two-color method analysis as gas temperature.

In engines, the spray flame from fuel injected are turbulent flow and are therefore strongly influenced by the properties of the fluid flow such as thermal conductivity, specific heat, viscosity and density. However, rate processes are usually characterized by correlations between dimensionless numbers i.e. Reynolds, Prandtl, Nusselt numbers [6]. Regarding Bergman and Lavine [107] this parameter (Nusselt number) is equal to the dimensionless temperature gradient at the surface, and it provides a measure of the convection heat transfer occurring at the surface. The Nusselt number is to the thermal boundary layer what the friction coefficient is to the velocity boundary layer.

The relation between Nusselt number (Nu) and Reynolds number (Re), Kuboyama et al. [44] applied turbulent heat transfer equation of the pipe internal flow which is assumed to be applicable for heat transfer in diesel engine. Where the Nu is a function of Re and Pr (Prandtl number).

$$Nu = (Const) \times Re^m \times Pr^n \quad (2.18)$$

Where Nu , Re and Pr are defined as the following equation (2.19), (2.20), and (2.21). m and n are defined based on the laminar or turbulent heat transfer. L is characteristic length, κ is thermal conductivity of the working fluid, ρ is density, U is characteristic velocity at each position, μ is viscosity and cp is specific heat. We used impingement distance and flame height as the characteristic length.

$$Nu = \frac{h.L}{\kappa} \quad (2.19)$$

$$Re = \frac{\rho.U.L}{\mu} \quad (2.20)$$

$$Pr = \frac{\mu.cp}{\kappa} = \frac{\nu}{\alpha} \quad (2.21)$$

As explained in the textbook [107], Reynolds number represents the ratio of the inertia to viscous forces. Prandtl number is defined as the ratio of the kinematic viscosity, also referred to as the momentum diffusivity, ν , to the thermal diffusivity α . The Prandtl number provides a

measure of the relative effectiveness of momentum and energy transport by diffusion in the velocity and thermal boundary layers, respectively.

2.5 Data Acquisition

Signals from the TFTHF sensors were acquired by a data logger (Graphtec: GL 900) and transferred to a PC. Sampling interval was 10 μ s. As the original signal contained very large noise component, low pass filtering was performed with Fast Fourier Transform (FFT) technique. The FFT technique has been used by some researchers [108], [21] to solving the noise components as shown in the following equation:

$$T(t) = T_m + \sum[A_n \cos(n\omega t) + B_n \sin(n\omega t)] \quad (2.22)$$

Where, $T(t)$ is time-dependent temperature profile at the wall surface. T_m is the time-average wall surface temperature. The FFT is applied in Fourier coefficients (A_n and B_n), n is the harmonic number and ω is angular velocity.

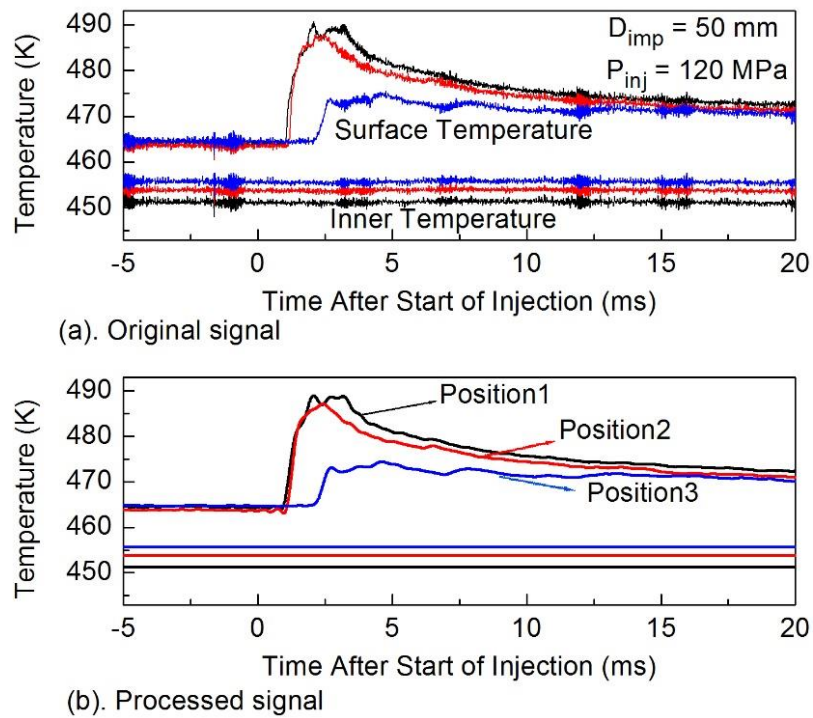


Figure 2.9 Original instantaneous temperature signals and their processed ones filtered by FFT: (a) original signal and (b) processed signal.

Figure 2.9 shows an example of original instantaneous temperature and its filtered one. We had got noiseless clean signal by the noise reduction process. Then by using the method

similar to Tatsumi [7] and Senda [36], which solves non-steady heat transfer equation with finite difference method by using measured temperatures as boundary conditions, we obtained instantaneous surface heat flux waveforms. Because it was very short time for one measurement, the surface temperature showed temperature rise by combustion, on the other hand inner temperatures were constant during the shot.

TFTHF sensors signal and spray/flame video image were recorded simultaneously with the injection. We cleaned the wall surface at every experiment condition change, since built-up deposits on the wall from combustion process affect the measurement accuracy according to Woschni and Huber [109]. Combustion differed from cycle to cycle and the surface temperatures were changed in every measurement, therefore we had carried the same condition measurement several times and averaged three good results.

2.6 TEST CONDITIONS

Measurement conditions, which were decided according to the actual diesel engine operating condition. It is assumed low load in a small size diesel engine. We performed three principal condition tests, i.e. non-evaporating spray, evaporation, and combusting spray in order to investigate the relation between spray/flame and heat flux.

In order to know spray characteristics such as: an effect of impinging distance, injection pressure, nozzle hole diameter and oxygen concentration, we investigated non-evaporating spray at room temperature without heating. Chamber pressure was set at 1.4 MPa with nitrogen gas in order to keep the ambient gas density same as combustion condition of 16 kg/m^3 .

In order to know the effect non-combustion (evaporating spray), nitrogen gas was supplied as ambient gas so as not to burn the spray. Ambient temperature and pressure conditions were the same as the combustion test.

We measured the wall temperature and took high-speed video photographs at the same time during combustion. Air (N_2 :79% and O_2 :21%) was used as ambient gas and its density was held at 16 kg/m^3 by setting chamber pressure and temperature 4.1 MPa and 873 K, respectively. Natural flame luminosity images from the high-speed video camera were used to analyze two-color method.

2.7 SUMMARY

In this chapter, the specific experimental apparatus, technical equipment and heat flux measurement were introduced. In order to investigate the mechanism of wall heat transfer with impinging spray/flame on the wall in improving the thermal efficiency. The spray/flame were carried out in high-speed video camera. The spray behavior was observed by applying Mie scattering method and flame temperature and soot concentration were calculated by applying two-color pyrometry, which was based on the flame natural luminosity result perceived by high-speed video color camera. Instantaneous temperature was detected by three Thin Film Thermocouple Heat Flux Sensors which were mounted on the wall surface side. Instantaneous heat flux into the impinging wall surface was computed using finite difference methodology based on one-dimensional unsteady heat transfer equation in which measured temperatures are used as boundary conditions.

CHAPTER 3

HEAT TRANSFER UNDER BASELINE CONDITION

3.1 INTRODUCTION

Heat loss is one of the main causes of energy loss in modern DI diesel engines. This heat loss of the engine occurs during combustion, mainly due to the heat transfer between the impinging spray flame and the piston cavity wall. In order to decrease heat transfer, we have to understand the phenomenon of heat transfer through the combustion chamber wall more clearly. Test rig of flat wall was used to investigate the effects of spray flame impingement on transient heat flux to the wall. Varying experimental conditions such as effects of impingement distance, injection pressure, nozzle hole diameter, oxygen concentration and its combined effect were studied on wall heat transfer mechanism. In this chapter, as a part of preliminary experiments, baseline condition will be used for comparing with all of parameter conditions in the all next chapter. Three conditions such as non-evaporation, evaporation and combustion are discussed in order to investigate the relation between spray/flame and heat flux.

3.2 EXPERIMENTAL CONDITIONS

The experimental apparatus used at all experiments are fundamentally the same, which was set up under diesel engine-like conditions. Spray/flame behavior was investigated with a high-speed video color camera. Simultaneously, the surface heat flux of the impingement wall was studied by three Thin Film Thermocouple Heat Flux (TFTHF) sensors. These sensors were mounted on the wall surface. Moreover, in order to investigate the mechanism of diesel flame and the wall heat loss, the two-color method was used to observe flame temperature distribution from luminous flame. The baseline condition information summarizes in Table 3.1 and 3.2. Injector and injection conditions are listed in table 3.1. The fuel injection was electronically controlled by a Bosch fuel injection system using a common rail. The injector was used a piezo actuator type and had single-hole nozzle with 0.133 mm nozzle hole diameter. In the baseline condition, injection pressure was kept at 120 MPa. Injection quantity and injection timing were controlled by a delay pulse generator (DG645).

Table 3.1 Injector and Injection Conditions

Injector type	Piezo actuator type
Number of nozzle holes	1
Injection quantity (mm ³)	5
Diameter of nozzle holes (mm)	0.133
Injection pressure (MPa)	120

Table 3.2 Experimental and Impingement Wall Conditions

Ambient condition	Non-Evaporation	Evaporation and Combustion
Ambient gas	N ₂	Combustion: Air (N ₂ :79%,O ₂ :21%) Evaporation: N ₂
Ambient pressure (MPa)	1.4	4.1
Ambient temperature (K)	300	873
Ambient density (kg/m ³)	16	←
Fuel	Diesel Fuel	←
Impingement wall	Flat plate, Stainless steel	←
Impingement distance (mm)	40	←
Wall temperature (K)	300	460 ±10
Cooling method	-	Oil cooling

We performed the test at three principal conditions such as non-evaporation, evaporation, and combustion. Throughout all conditions were kept uniform ambient density, i.e. 16 kg/m³. In case of non-evaporating spray, nitrogen gas was used as ambient gas at room temperature without heating. Nitrogen gas also was supplied as ambient gas so as not to burn the spray under evaporation condition. Ambient temperature and pressure conditions were the same as the combustion test. The wall temperature was controlled at 460 ±10 K both evaporation and combustion test. We measured the wall temperature and took high-speed video photographs at the same time during combustion. Air (N₂:79% and O₂:21%) was used as ambient gas under combustion case. The distance from nozzle tip to the wall was set up at 40 mm. Table 3.2 summarizes the experimental and impingement wall conditions.

3.3 SPRAY BEHAVIOR

In this section, the impinging spray behavior under non-evaporation and evaporation conditions were studied. Spray images were recorded by high speed video color camera with frame rate of 20,000 frame per second (fps) at 320 x 448 pixels image resolution, which each represent 5 pixels per mm. Mie scattering method was used both non-evaporation and evaporation conditions in order to investigate impinging spray behavior. A Xenon lamp and two reflection mirrors were applied for the source of scattering light. The light from Xenon lamp illuminated the spray in the combustion chamber through the sideward transparent quartz window.

Figure 3.1 (a-b) shows line-of-sight images from high speed video camera. Left and right side are non-evaporating and evaporating wall impinging spray images. These results after removed such extra element by image processing. Spray travel from the top to the bottom at each photo and impinges on the wall. Both non-evaporating and evaporating spray images were observed at same ambient density (16 kg/m^3), which used room temperature (300 K) for non-evaporating spray and at high temperature (873 K) for evaporating spray. The vertical axis shows time after start of injection (ASOI). Time 0.1 ms to 1.2 ms ASOI represents the spray evolution during injection duration.

In the case non-evaporating spray in Figure 3.1 (a), spray was injected and impingement to the wall at 0.45 ms ASOI. Spray continues to be injected and spray flows radially spread to circumferential wall area after its impingement to the wall. The spray impingement on the wall might affect to the mixture formation and air entrainment comparing with before impingement to wall. On the other hand, under evaporating spray condition in Figure 3.1 (b), the liquid phase concentration decreases significantly due to high ambient temperature which could promote spray atomization and air-fuel mixture. The intensity of white color shows liquid spray concentration. As can be seen in the figure, the liquid phase of the spray could not reach to the wall. It indicates that impingement distance of 40 mm enough to do a conversion from liquid to vapor phase before it reaches over to the wall. The liquid phase almost complete evaporates at 1.2 ms ASOI as indication of the end of fuel injection.

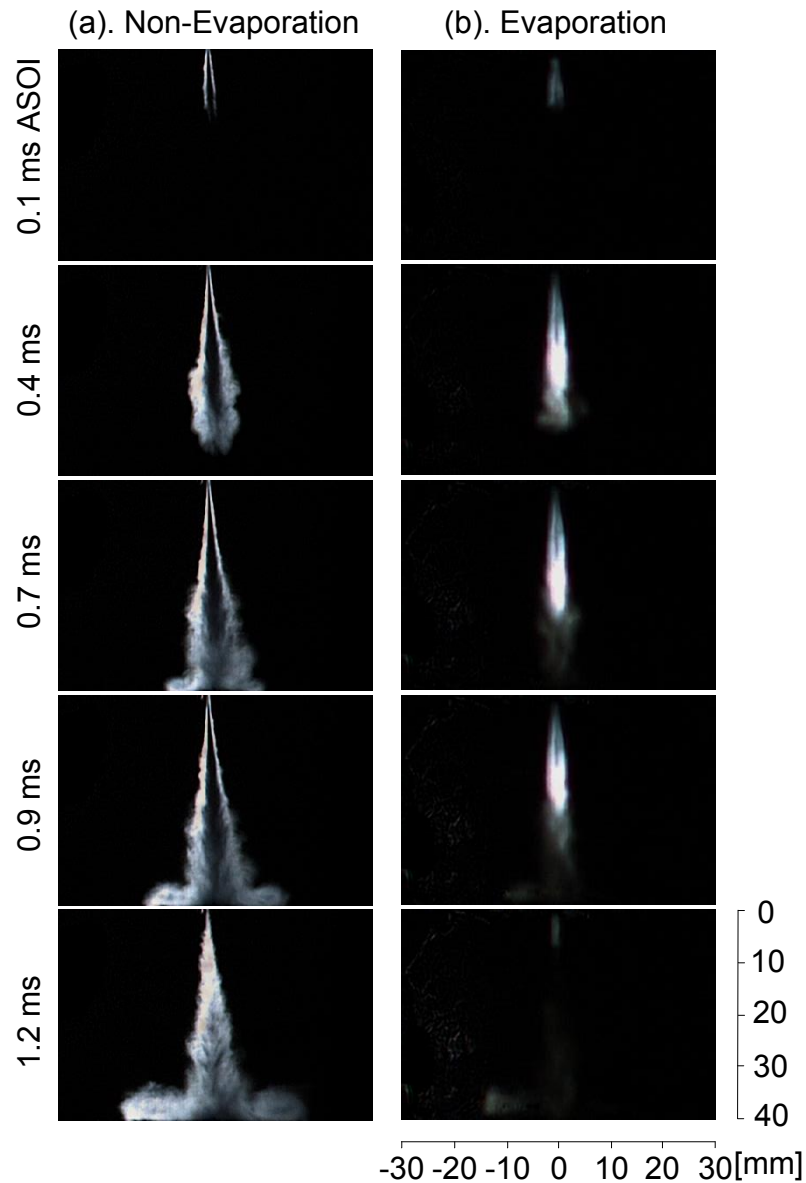


Figure 3.1 High-speed video camera images of wall impinging spray at non-evaporating and evaporating

Spray tip penetration, which was obtained from the non-evaporating spray and liquid length from evaporating spray images are presented in Figure 3.2. The injection duration was 1.2 ms ASOI. Spray tip penetration length in vertical axis on the left-side graph is defined as a summation of axial (D_{imp} : impingement distance) and radial penetration distances (S_{wall} : Spray on the wall after impingement) as shown in Figure 2.3. The liquid length in vertical axis on the right-side graph, which was defined similar to the non-evaporating spray, was obtained by the image processing as the maximum liquid penetration during the injection using a pre-

determined threshold intensity. We used a threshold intensity of 10 % on the 0 to 255 intensity scale of the image.

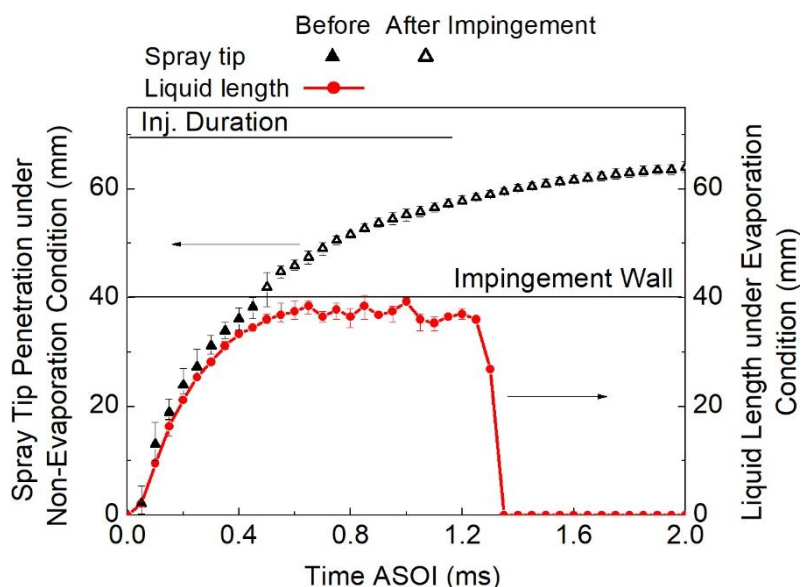


Figure 3.2 Definition on non- evaporating spray tip penetration and its measurement result of spray tip penetration and liquid length

The closed and open triangles show the liquid length under evaporation before and after the spray impingement on the wall, respectively. Under non-evaporating spray, the spray tip penetration increased with time, although the fuel has done injected. This means that the spray rate was continuously enhanced to cover a wider area along the flat wall. In contrast, the liquid length linearly increased with time for only a few hundred milliseconds ASOI until it reached a maximum liquid length penetration. The liquid length penetration was saturated under 40 mm. When it reached the maximum value, the liquid length remained constant, with slight fluctuation, although the fuel continued to be injected. Furthermore, the liquid length immediately dropped just after the end of injection. In this time, all the fuel was completely evaporated. As shown in the comparison in Figure 3.2, the liquid length of the evaporating spray decreased significantly in relation to that of the non-evaporating spray condition.

3.4 COMBUSTION FLAME BEHAVIOR

In this section, the behaviors of the impinging flame and how combustion affects the wall heat transfer are studied. Figure 3.3 shows impinging flame images captured by a high-

speed color video camera. These figures represent the time history of the impinging flame's natural luminosity development. As commonly discussed, the flame's natural luminosity comes primarily from soot incandescence and chemiluminescence. In a diesel engine, the soot incandescence is dominated by the thermal radiation from soot particles in flame, with a broadband emission spectrum. As illustrated in the non-evaporating spray photographs in Figure 3.1a, luminous flames occurred a few hundred micro-seconds after the spray impingement, at 0.9 ms ASOI, and then disappeared after 1.9 ms ASOI. The most luminous flame was observed at 1.3–1.5 ms ASOI. Moreover, considering the photographs of non-evaporating spray in Figure 3.1b, it can be seen that a luminous part was present in the vapor area due to combustion. The combustion occurred in the vapor area near the center of the wall impingement. This area provided a suitable equivalence ratio and temperature for ignition [110].

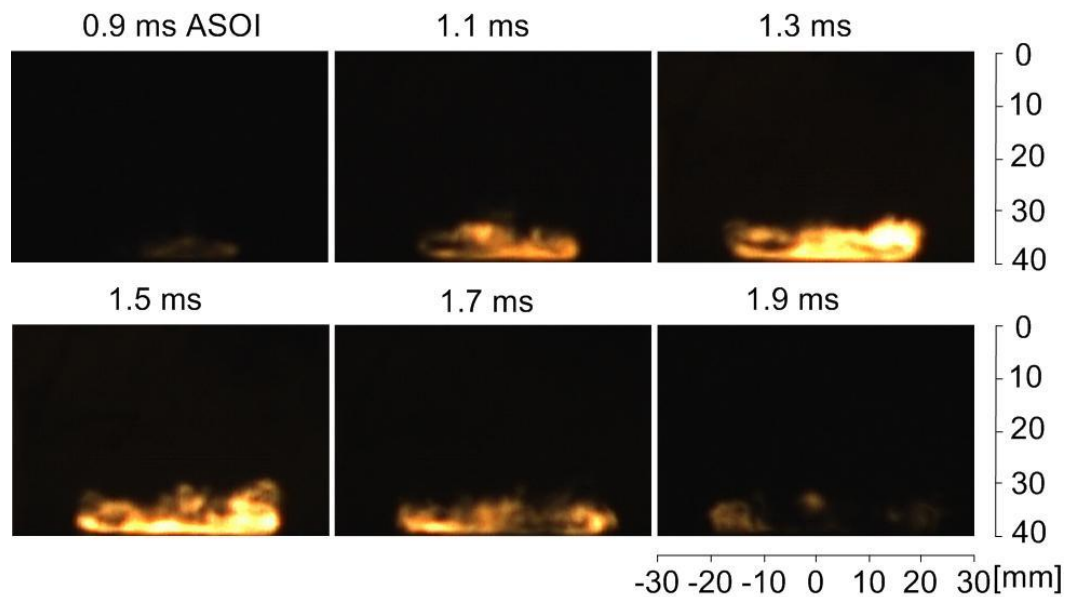


Figure 3.3 Video images of impinging flame distribution

3.5 HEAT FLUX AND TOTAL HEAT TRANSFER

Unsteady local heat flux and integrated flame luminosity were used for studying heat transfer from the combustion flame to the impingement wall. The local heat flux was computed from temperatures measured by TFTHF sensors, and the integrated flame luminosity was

calculated using the total of red color values from natural flame color images. The results are illustrated in Figure 3.4. The upper side shows the integrated flame's natural luminosity, while the lower side shows the local heat flux. The horizontal axis shows the time ASOI. The timings of spray impinging and ignition, obtained from video images, are also plotted in the graph. The luminosity increase starts nearly at the ignition timing.

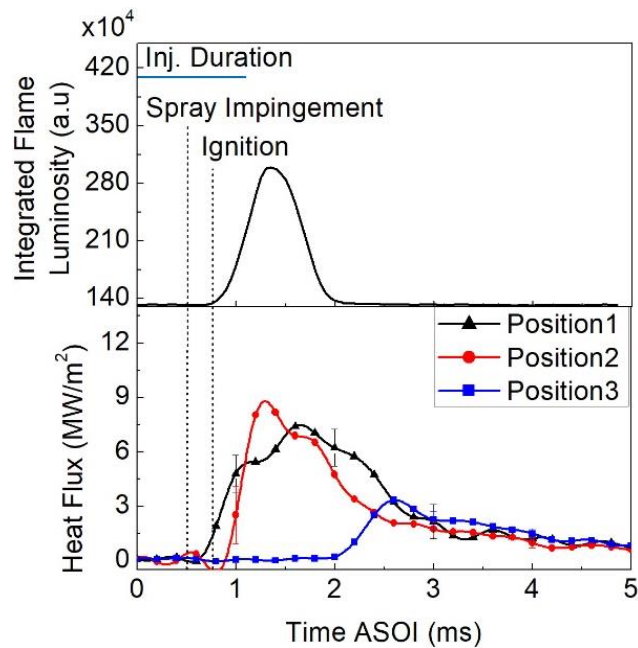


Figure 3.4 Local heat flux and integrated flame luminosity

As shown in the local heat flux graph, the time histories of local heat fluxes were different at the three measurement locations (Position1, Position2, and Position3). These differences can be attributed to the spatial nonuniformity of the spray and flame flow. The spray flowed radially after impingement, and it arrived at each position at different timings, causing heat flux fluctuation. The local heat flux at Position1 started to increase earlier, followed by Position2 and Position3 in all conditions. The observed increase in local heat flux at Position1 could be interpreted as being a result of the effect of convection when a turbulent part of the evaporating spray impinges to the wall. Then, the large effect of combustion gas velocity was responsible for starting the local heat flux peak at Position2. Another possible explanation for this is that the impinging flame was strongly developed from Position1 to Position2 in this timing, as shown in Figure 3.3. As commonly discussed, the luminosity is related to the soot volume fraction and temperature, where the temperature has a high impact on the heat transfer

rate. In addition, the local heat flux at Position3 was significantly lower than the heat fluxes at the other positions, since both wall friction and momentum loss due to turbulent mixing took place. This local heat flux also increased later than it did at the other positions because the flame travel took time to reach Position3 (20 mm from the center of impingement).

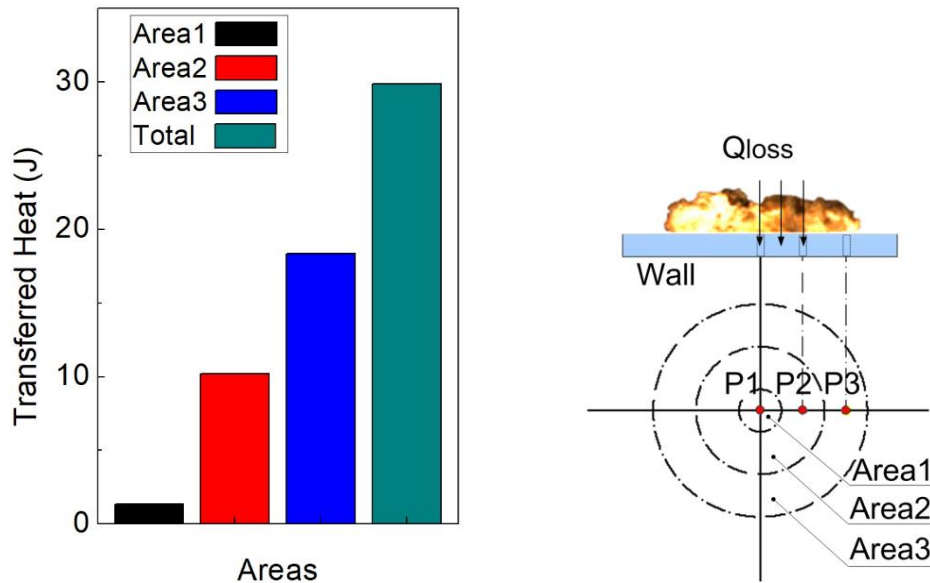


Figure 3.5 Areas and total transferred heat

Figure 3.5 shows the areas and total transferred heat. The values are a summation of heat fluxes at the toroidal area of the sensors during the heating period; the definition of areas on the wall surface can be seen in Figure 2.8. From the graph, it is evident that the transferred heat increased with a wider area. This means the wider area (Area3) gave more transferred heat to the wall, although the local heat flux value at Position3 was smaller, as shown in Figure 3.4. The total transferred heat under the base condition was around 30 joules.

3.6 SUMMARY

At baseline, the correlation between spray/flame behavior and transient local heat flux under diesel-like conditions was investigated in this chapter. Based on the results obtained, the main conclusions can be summarized as follows:

1. There were significant differences between the images of evaporating and non-evaporating spray in terms of liquid phase concentration. These were also confirmed in terms of the

liquid length, which showed a substantial decrease in the evaporating compared with the non-evaporating spray condition. This suggests that a high ambient temperature under evaporating conditions could promote spray atomization and the air-fuel mixture;

2. By using a high-speed video camera, it was found that the liquid phase concentration hardly reaches the wall at a distance of 40 mm. At the vapor area around the center of impingement, flame luminosity occurrence was identified after reaching a certain temperature for ignition;
3. The nonuniformities of spray and flame flow after impingement on the wall, resulting in transient local heat fluxes, were different at the three measurement locations (Position1, Position2, and Position3) in relation to different timing of rises and peak values;
4. The mechanism of heat transfer on the wall and its correlation with the spray/flame behavior was explained in detail in the transient local heat flux waveform; and
5. The heat transfer area is more influential in wall-transferred heat compared with the local heat flux value at each point.

CHAPTER 4

HEAT TRANSFER UNDER VARIOUS IMPINGING DISTANCES

4.1 INTRODUCTION

In small high speed-diesel engine, an injected fuel spray impinges on a piston cavity surface due to the short distance between the injection nozzle tip and the surface, where the distance between them varies both locational and time. However, it is too difficult to study the relation of heat transfer and combustion with the running engine. Therefore, it is necessary to investigate the impinging spray flame under different impingement distances with chamber rig test. For these reasons, this chapter aims to investigate the effect of flat-wall impingement distance on transient local heat flux, combustion and soot distribution from the spray and flame to the impinging wall. In order to investigate the mechanism of diesel flame and the wall heat loss, the two-color method was used to observe soot and flame temperature distribution from luminous flame photography. Furthermore, measurement of heat flux into the impinging wall surface was computed using finite difference methodology based on one-dimensional unsteady heat transfer equation in which measured temperatures are used as boundary conditions.

4.2 EXPERIMENTAL CONDITIONS

Measurement conditions, which were decided according to the actual diesel engine operating condition, are listed in Table 4.1 and 4.2. It is assumed low load in a small size diesel engine. The ambient pressure and temperature for combustion and evaporating experiments were selected as 4.1 MPa and 873 K to reproduce the thermodynamic environment near top dead center in combustion chamber of a low compression ratio diesel. We performed three principal condition tests, i.e. non-evaporating spray, evaporation, and combusting spray in order to investigate the relation between diesel spray/flame and heat flux on the wall. All of conditions were keep the same ambient gas density of 16 kg/m^3 . In order to measure ambient temperature, four K-type thermocouples were fitted in the middle of the nozzle tip and the wall, and three were near the wall. A heat flux measurement was done a little later after hot gas feed for avoiding turbulence in the vessel. Injection direction was set perpendicular to the impingement

wall. To understand the impinging spray behavior, diesel sprays impinging on flat wall was studied using Mie Scattering method at non-evaporation condition. The impingement distances between the nozzle tip and impingement wall were set at 30, 40, and 50 mm with spacer as shown in Figure 2.3.

Table 4.1 Injector and Injection Conditions

Injector type	Piezo actuator type
Number of nozzle holes	1
Injection quantity (mm ³)	5
Diameter of nozzle holes (mm)	0.133
Injection pressure (MPa)	120

Table 4.2 Experimental and Impingement Wall Conditions

Ambient condition	Non-Evaporation	Evaporation and Combustion
Ambient gas	N ₂	Combustion: Air (N ₂ :79%,O ₂ :21%) Evaporation: N ₂
Ambient pressure (MPa)	1.4	4.1
Ambient temperature (K)	300	873
Ambient density (kg/m ³)	16	←
Fuel	Diesel Fuel	←
Impingement wall	Flat plate, Stainless steel	←
Impingement distance “D _{imp} ” (mm)	30, 40, 50	←
Wall temperature (K)	300	460 ±10
Cooling method	-	Oil cooling

4.3 SPRAY BEHAVIOR

In this section, behavior of the impinging spray at room temperature with different distances were studied. Three impingement distances from injection tip to the wall, i.e. 30, 40 and 50 mm, were investigated at injection pressure 120 MPa. In the all experiments, injected quantity was uniform at 5 mm³.

At 0.3 ms ASOI, spray reach to the wall under impingement distance (D_{imp}) of 30 mm. At this timing, no significant variations are appearing among spray behavior under different distances. When impingement distance is increased to further, the spray/wall interaction does not occur in this timing. By increasing the timing to 0.5 ms ASOI, the impingement just

occurred under $D_{imp} = 40$ mm. It just few hundred micro-second after $D_{imp} = 30$ mm impingement to the wall. This confirms that the impingement timing of spray become later with its distance. The spray distributions are nearly similar under $D_{imp} = 40$ and 50 mm. However, under $D_{imp} = 30$ mm, the spray droplet radially spread along to wall after impingement.

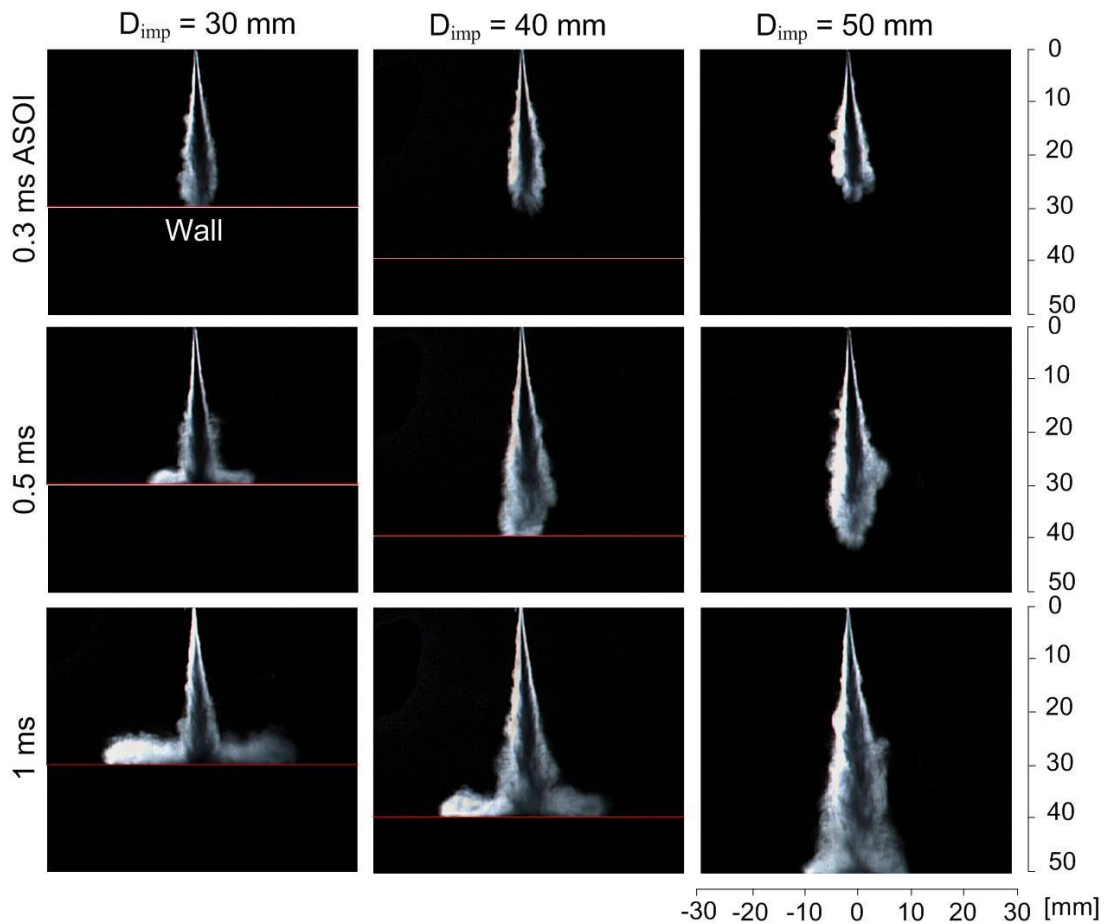


Figure 4.2 Non-evaporating wall impinging spray at different distances

When time is increased to 1 ms ASOI, $D_{imp} = 50$ mm also undergoes impingement to the wall. In this timing, distribution of spray droplet only around the center of impingement. When attention is paid to $D_{imp} = 30$ and 40 mm, spray droplet spread to large area along to wall especially at shorter impingement distance. By comparing each distance, the impingement timings are linearly increased with its distance. Due to air entrainment and spray atomization process at before and after impingement, the impingement timing influences the ignition delay and even more at combustion process.

Spray tip penetration length with different distances obtained from the non-evaporating spray images is plotted in the Figure 4.3 (a). Close and open symbols show before and after spray impingement on the wall each. Penetration loci of three impinging distances agree with each other until impingement on the wall, but they differ each other after impingement. This much difference in penetration length after impingement can be observed. Even though the $D_{imp} = 30$ mm has more spray spread along to wall. By this figure, it can be finding the tip penetration is reduced by smaller impinging. Figure 4.3 (b) shows spray tip penetration velocity during spray injection. The figure shows almost the same inclination after impingement among the three impingement distances. It indicates that the distance variation with same injection pressure is not significant effect on the velocity.

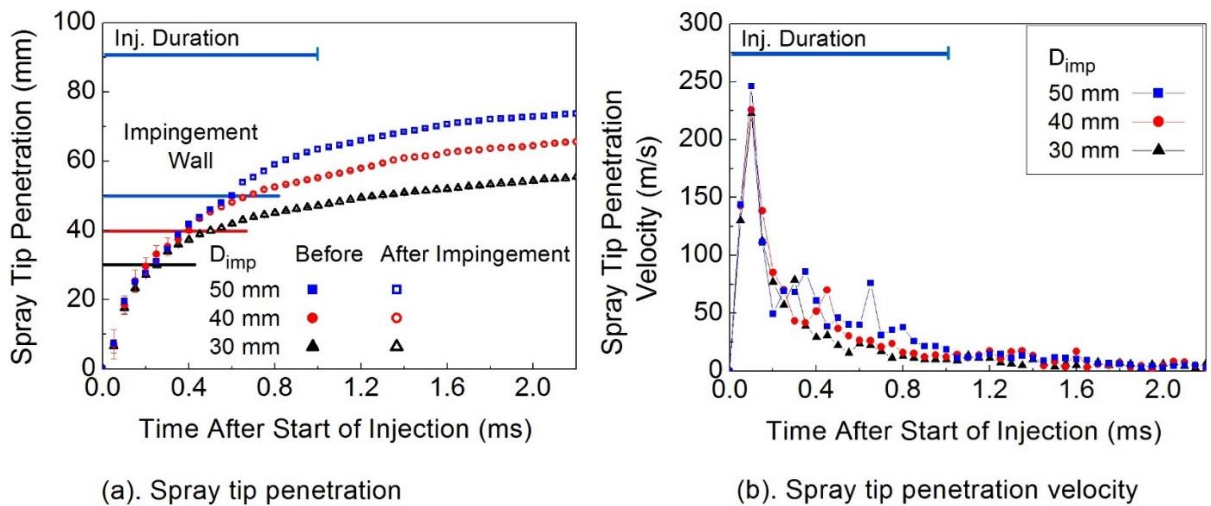


Figure 4.3 Spray tip penetrations and spray tip penetration velocity at different impingement distances.

4.4 COMBUSTION FLAME CHARACTERISTICS

4.4.1 Flame Natural Luminosity

The influences of impingement distance on ignition and combustion process were investigated. Figure 3.4 shows the luminous flames from the high-speed video color camera. The flame structure and combustion behaviors were differed under various impingement distances. At 1.1 ms ASOI, flame natural luminosity was observed in near wall surface area in all distances. The flame behavior was similar with non-evaporation images, where the flame luminosity more spread along to wall under smaller impingement distance. At this timing, the

ignition delay from these photographs by the luminosity change due to start of a chemical reaction of combustion. It was confirmed that the ignition delay became later with distance. It might spray mixture was improved by earlier impingement and the combustion occurred after impingement to the wall in all conditions.

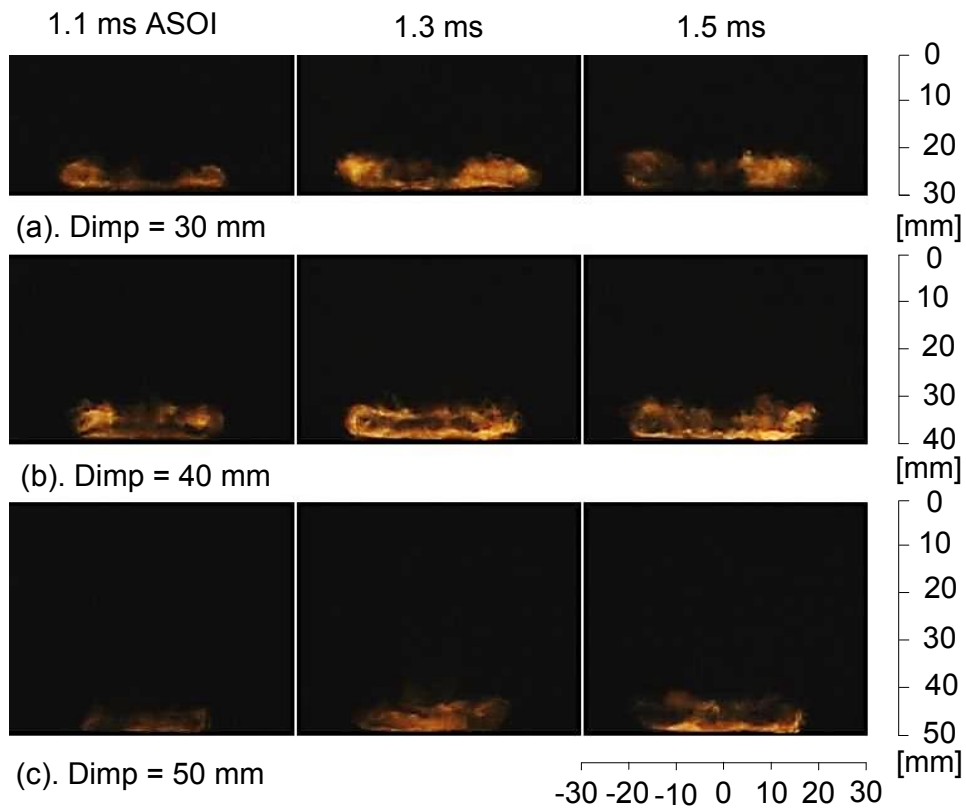


Figure 4.4 Video images of impinging flame at different distances

At 1.3 ms ASOI, the impinged flame was tended to roll up which caused by shorter impingement distance at $D_{imp} = 30$ mm. It suggests that the wall-jet vortex was large due to high turbulent effect in this distance. When the distance increases to $D_{imp} = 40$ mm, the impinged flame natural luminosity was seen uniform. It means soot luminosity was significant occurred in this distance. On the other hand, $D_{imp} = 50$ mm with longer impinging path, the impinged flame became slow with small flame area. This longer impingement distance lead to enough time the spray atomization and fuel-air mixture before its impingement. As time continues to 1.5 ms ASOI, flame natural luminosity was decreased and the flame behavior proceed to roll up under $D_{imp} = 30$ mm. However, the impinged flame continues develop along

to wall under both $D_{imp} = 40$ and 50 mm. It is because the ignition delay become later with the longer distances, which influence to the combustion duration process.

4.4.2 Two-Color Method Results

This section shows results of combustion and soot formation process analyses under the different impingement distances. In diesel combustion, radiated luminosity of flame, which is generated from the soot combustion, can represent combustion temperature by black-body radiation theory. Then we analyzed the natural flame images with two-color pyrometry.

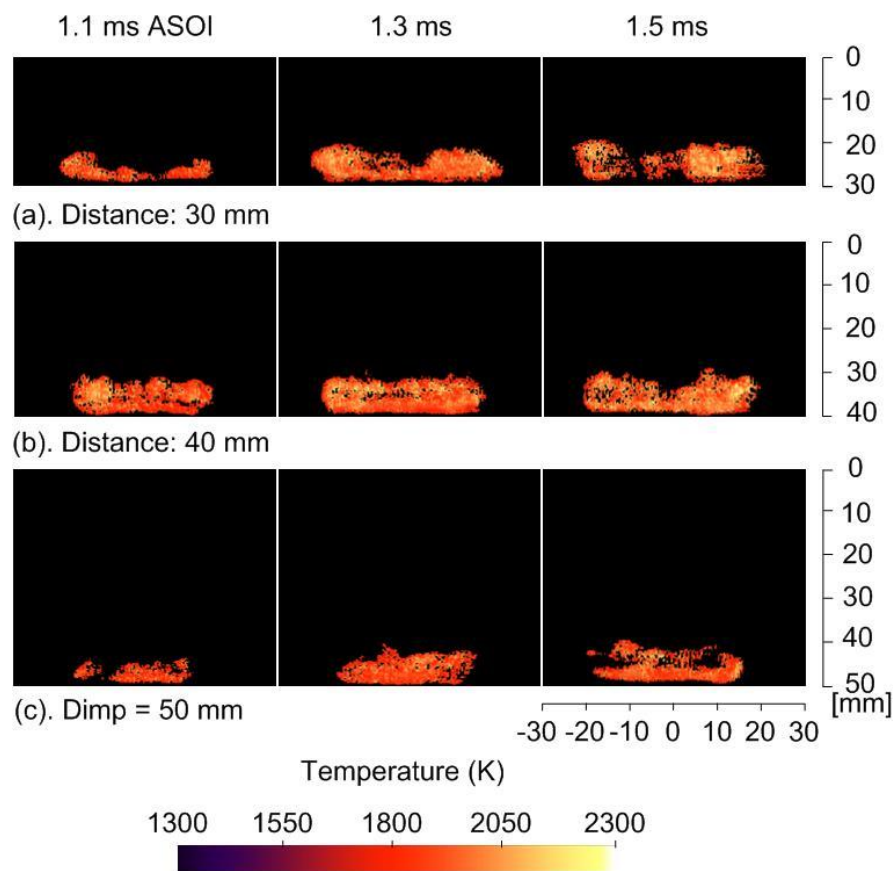


Figure 4.5 Flame temperature at different distances

Figure 4.5 and Figure 4.6 shows distribution of temperature and KL factor obtained at each impinging distance. The figure compares from 1.1 ms until 1.5 ms ASOI, which is around the maximum values at each distance. The distribution shapes of high temperature and KL factor are similar, because both of them are obtained from images of luminous flame by soot combustion.

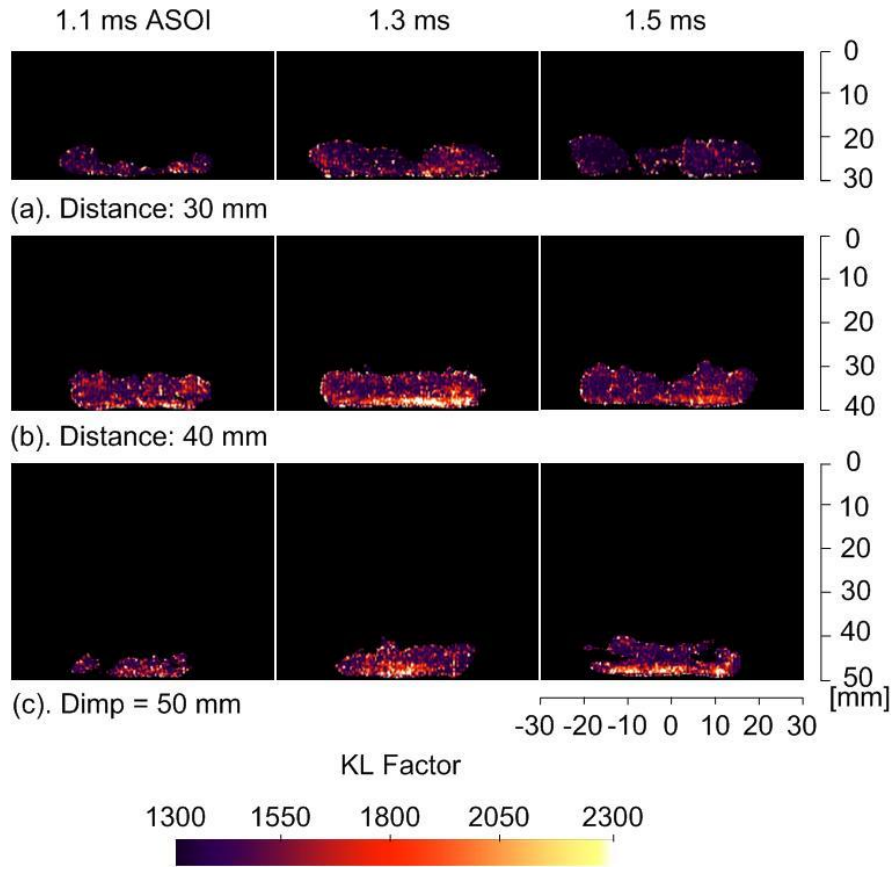


Figure 4.6 KL factor at different distances

In the temperature images, at 1.1 ms ASOI, the temperature occurred around the center of impingement area (0 -10 mm) along to wall. After 1.1 ms ASOI, the temperature continues to increase at all distances. From the figure it can be seen that the temporal and special temperature distributions were within 1800-2050 K. A great deal of attention must be paid when 1.5 ms ASOI, the flame temperature shape area almost uniform under $D_{imp} = 40$ mm comparing with other distances. Consequence the rate of heat transfer to wall will be given to $D_{imp} = 40$ mm. In the KL factor images, the large soot concentration was detected along the wall surface at all distances. These indicates that the fuel film could not avoid under impinging flame condition and high particle concentration is produced. It means the combustion is incomplete and rich local equivalence ratio occurs along wall surface area.

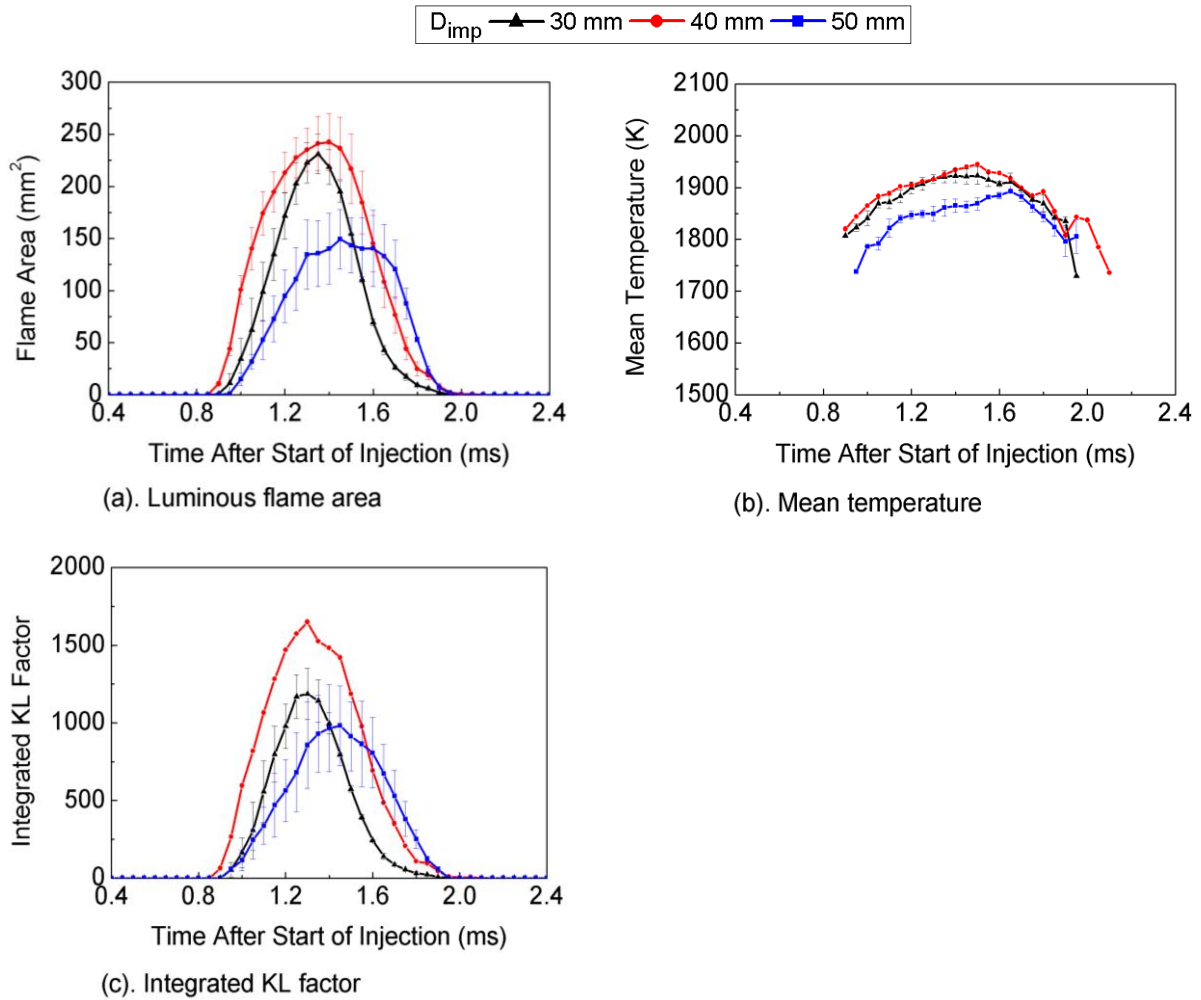


Figure 4.7 Luminous flame area, mean temperature and KL factor at different distances

Each of Figure 4.7 (a-c) shows transition of luminous flame area, mean temperature and integrated KL factor. Even though the $D_{imp} = 30$ mm has most widely spread flame temperature area due to shorter impingement distance. However, flame area was slightly decreased comparing with $D_{imp} = 40$ mm. These also applied to mean temperature and integrated KL factor. Two possible explanations for the reduction in KL factor are as follows: (1) impinged spray droplets were rolled up which caused by shorter impingement distance. This results in better mixing with ambient air, which enhances oxidation of fuel and reduces soot formation. (2) Thermal interaction that cools the spray, makes the rate of soot formation slow [25].

At $D_{imp} = 40$ mm shows higher flame area, mean temperature and KL factor compared with the other impingement distances. It can be seen in temperature images that the large flame temperature behavior was detected every timing increased. Regarding KL factor was increased,

it means the deteriorated combustion occurred at this distance thus it leads high soot formation. It can be proved by the soot distribution near the wall was higher comparing with other distances as shown in Figure 4.6. The mean temperature also higher in this distance, as flame natural luminosity was much higher in Figure 4.4 which It was related to temperature and soot fraction.

When increasing the distance to 50 mm, flame area, mean temperature and KL factor were significant lower value. At $D_{imp} = 50$ mm with longer impinging path, combustion became slow with lower temperature and soot formation was reduced due to the improved fuel air mixing before combustion occurrence. According to Li et al. [46] experiment, combustion is enhanced by increasing the impingement distance. As shown in Figure 4.7, distribution of flame are similar to KL factor, thereby temporal changes of luminous flame area are also similar to the KL factor.

Spatial distribution of local temperature in near wall under flame impinging becomes important to clarify the heat losses on the wall. Temperature near the wall highly influences to the wall temperature due to rapid heat transfer by convection. Figure 4.8 shows the areal averaged temperatures at 0.8 mm from wall surface in the three areas. These result in the all plots were obtained from Figure 4.5. It cannot be plotted when no luminous flame was observed at the area. The above figure shows that temperature distribution is varying in the radial direction in that time. It implies strong combustion gas turbulent flow exists together with the combustion reaction. At $D_{imp} = 30$ mm, the temperature near wall was higher in the earlier timing at 1 ms to 1.1 ms ASOI than other distances. This was increased at all positions due to earlier ignition which was occurred in near wall and flame spread to wider area. However, because the impinged flame underwent roll up due to shorter distance, the temperature near wall was saturated and decreased by increasing timing.

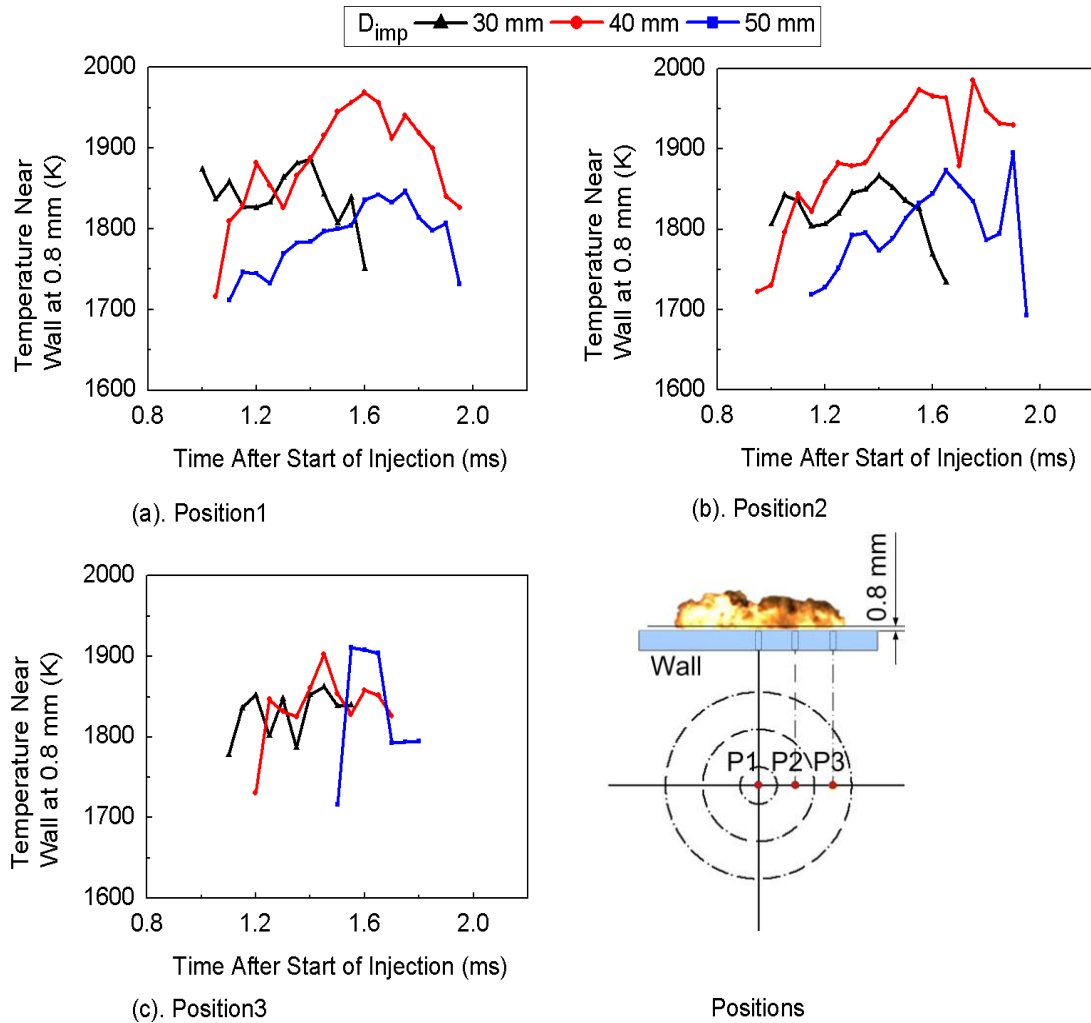


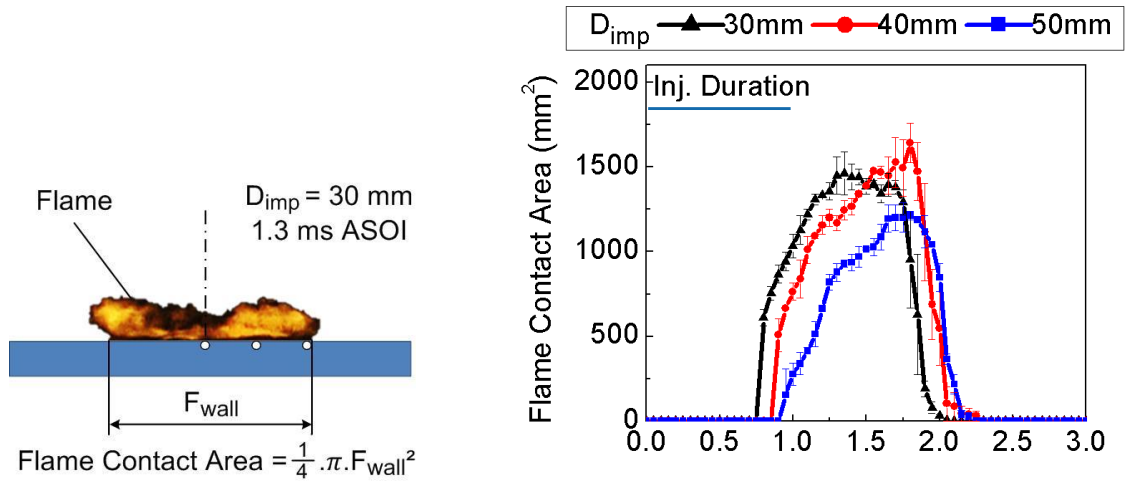
Figure 4.8 Near wall temperature at 0.8 mm from wall

The graphs show that the At $D_{imp} = 40$ mm has the maximum temperature at Position1 and 2. If these areas are dominant for wall heat transfer, $D_{imp} = 40$ mm shows the maximum heat transferred. However, as shown in the later section, transferred heat is similar both $D_{imp} = 30$ and 40 mm. Therefore, average temperature has not so dominant effect on heat transfer to the wall. On the other hand, $D_{imp} = 50$ mm was lower temperature except Position3 comparing with other distances. However, at Position3, the impinged flame occurred later and short resident time because the flame growth to wider area takes time due to longer path.

4.4.3 Flame Contact Area

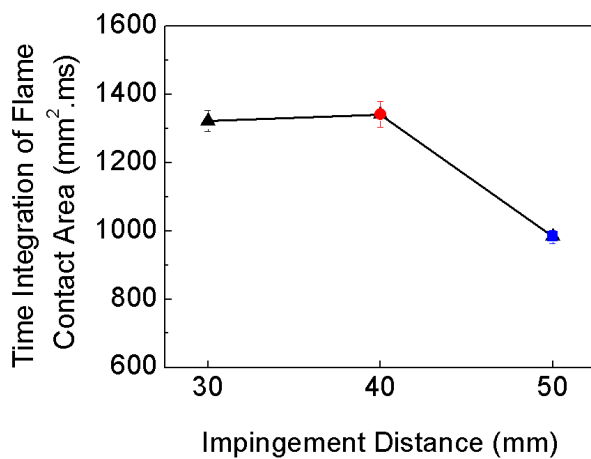
Since temperature of flame is so high to increase instantaneous heat flux, flame contact area can be thought one of the influential factors that affect the heat transfer rate by conduction.

In order to study the effect of flame contact to the wall, flame contact area was calculated using the flame photographs. The flame contact area assumes where flame is in contact with the wall surface with a concentric circular area as shown in Figure 4.9 (a).



(a). Definition of flame contact area

(b). Flame contact area



(c). Time integration of flame contact area

Figure 4.9 Definition, flame contact areas and time integration of flame contact areas at different distances

Temporal changes of the flame contact area at the different distances are shown in Figure 4.9 (b). It shows that $D_{imp} = 30$ mm which shorter distance makes quicker flame contact area increase. However, when time is increased and impinged flame growth to wider area, $D_{imp} = 40$ mm lead large flame contact area. The maximum flame contact area is around 1700 mm^2 .

On the other hand, $D_{imp} = 50$ mm in which longer distance from the wall surface have a smaller contact area than smaller distance.

Time integration of the flame contact areas are shown in Figure 4.9 (c). For calculating the time integration of flame contact area, it used the same equation to Tatsumi [8] as shown in the follows:

$$\text{Time integration of flame contact area} = \int_0^{\tau} A dt \quad (4.1)$$

Where A is an instantaneous contact area, and τ is end of combustion. The figure shows that $D_{imp} = 30$ and 40 mm have similar contact area and they are larger than 50 mm, though each of the three contact periods is similar. It can be thought that more heat was lost at $D_{imp} = 30$ and 40 mm due to the wider flame contact area than 50 mm.

4.5 HEAT FLUX AND TOTAL HEAT TRANSFER

Unsteady local heat flux with flame impinging on the wall was investigated. Figure 4.10 shows local heat flux computed from temperatures measured by the TFTHF sensors and integrated luminosity of the red component of flame images at each impinging distance. Timings of spray impinging and ignition, which are obtained from video images, are also plotted in the graphs. Luminosity increase starts nearly at the ignition timings at all distances, however, heat flux increase starts before the ignition timings at both Position1 and Position2 in all distances. On the other hand, at Position3, it starts increase far after the luminosity increase starts in all distances. Combustion photographs of Figure 4.4 show that combustion simultaneously starts in some range, which covers Position1 and 2, near the wall then spreads to the circumferential area of the wall with increasing brightness. Spray impinges at a range and extends radially, therefore it takes time to reach the 20 mm position.

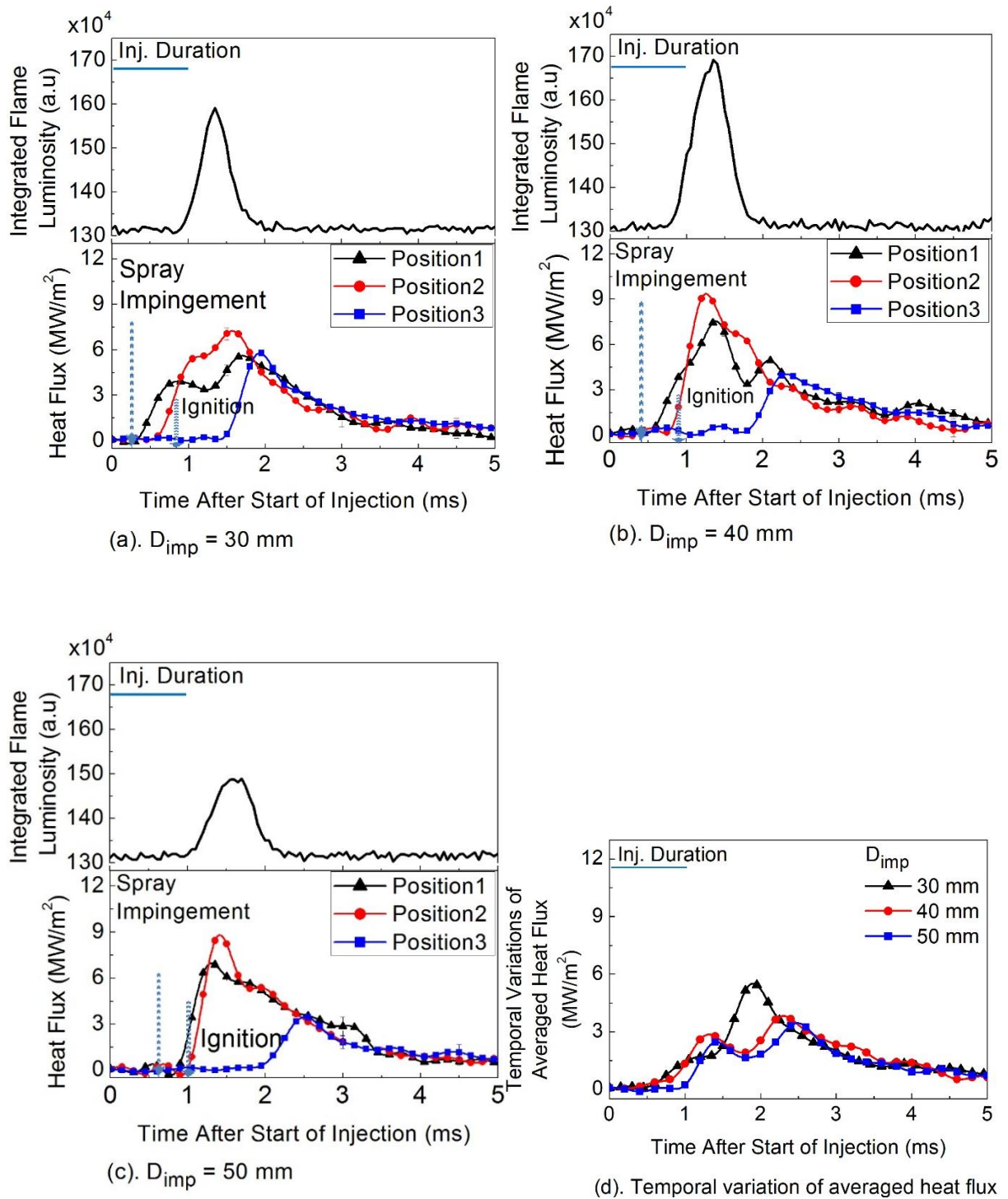


Figure 4.10 Local heat flux and integrated flame luminosity at different distances

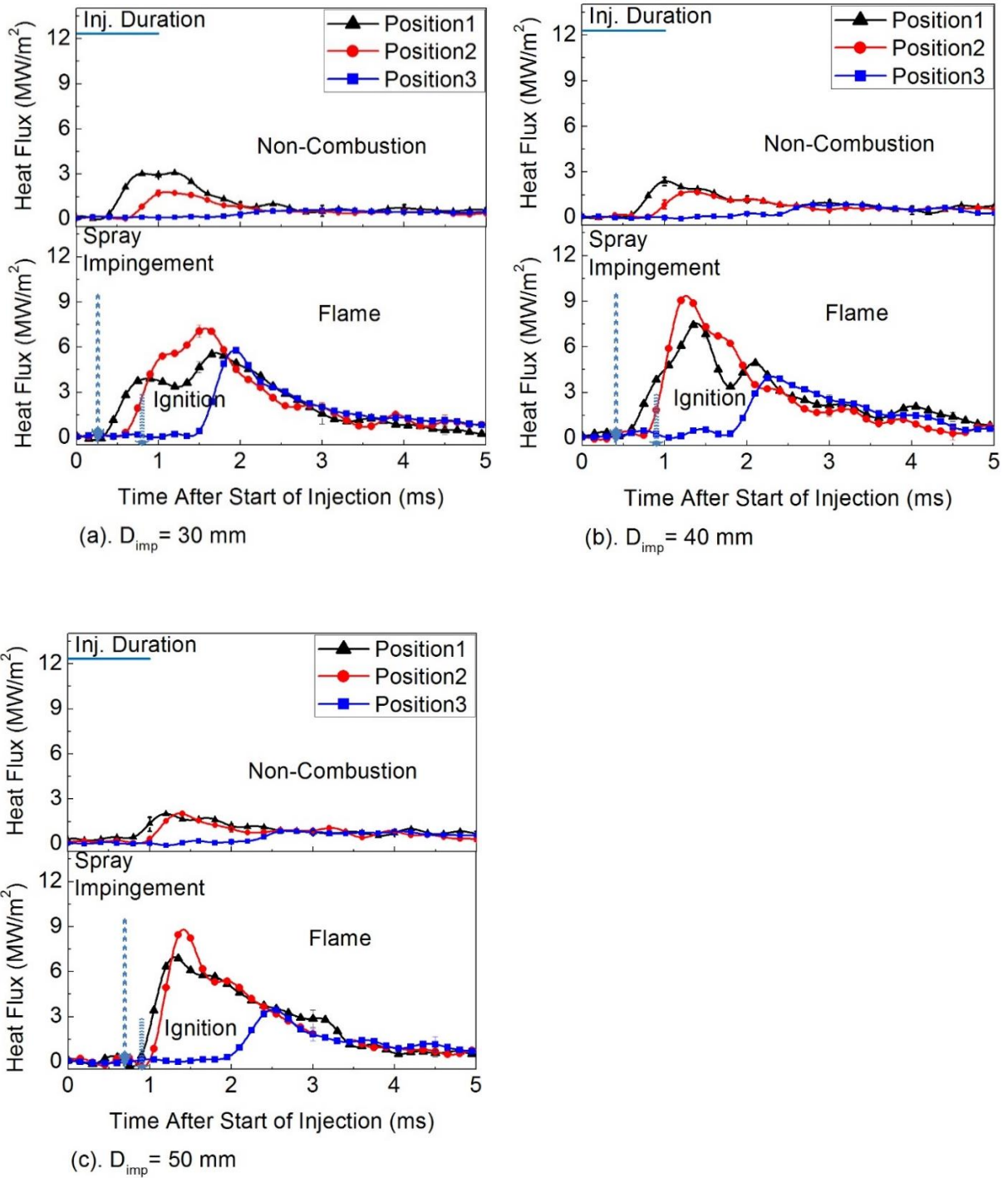


Figure 4.11. Comparison of local heat flux between combustion and non-combustion

The increase timings of the Position3 are roughly agreed with penetration timings to the point which are obtained from the Figure 4.3 (a). By these facts, it seems that the heat flux increase comes from convection by turbulence with spray arrival. This convection theory also

explains that the heat fluxes continue after luminosity drops to the base level in all distances. It indicates that strong hot gas flow non-luminous flame still exists after end the combustion.

The local heat flux waveform at Position1 has a large valley after increasing in Figure 3.12 (a). Combustion varied with time and was weak at this timing as shown Figure 4.4 (a). The maximum local heat flux values are achieved at Position2 in all distances because in that position has higher temperature near wall as shown in Figure 4.8. In this graph found that the dominant higher temperature near wall was $D_{imp} = 40$ mm. This phenomenon can be explained why $D_{imp} = 40$ mm have larger local heat flux. However, local heat flux at Position3 was lower values except $D_{imp} = 30$ mm. It means the $D_{imp} = 30$ mm in which impinged flame spreads to a larger area lead significant heat transfer rate.

Temporal variations of averaged heat flux were calculated by summing local heat flux timed by area over all of the area. Figure 3.12 (b) shows the result of temporal variations of averaged heat flux under impingement distance. It shows $D_{imp} = 30$ mm has the maximum temporal variations of averaged heat flux value. The area is influential factor for the temporal variations of averaged heat flux. At a smaller impingement distance, it was more affected. This is evidenced by local heat flux at Position1, 2 and 3 has almost a similar maximum value as shown in Figure 4.10 (a) compared with $D_{imp} = 40$ and 50 mm in Figure 4.10 (b-c), respectively. It was 5.5 MW/m^2 for $D_{imp} = 30$ mm, 3.8 and 3.4 MW/m^2 for $D_{imp} = 40$ and 50 mm, respectively. Even though, the local heat flux has peak value at $D_{imp} = 40$ mm, there were no significant differences between $D_{imp} = 40$ and 50 mm in term temporal variations of averaged local heat flux.

The reason of the heat flux increase phenomenon by convection could also be explained by comparison of local heat flux between combustion and non-combustion in Figure 3.13 as follows.

1. The start points of local heat flux increase at all positions are similar between combustion and non-combustion in all distances.
2. In case of non-combustion, local heat flux increase only comes from convection by spray impingement.
3. Under non-combustion, the local heat flux value was decreased with its distance.

4. There was significant local heat flux waveform at each distance in combustion case. These differences can be attributed to spatial nonuniformity of spray and flame flow at difference distances.

In non-combustion, the highest local heat flux occurs at the center of impingement. On the other hand, in combustion, the local heat flux at Position2 has the maximum value. It can be thought that the combustion flame most developed around the location somewhat distant from the impingement center. According to this explanation, the local heat flux increase has two stages. At first, the local heat flux is increased by turbulence by non-combustion spray. Then combustion which starts after impingement accelerates the increase.

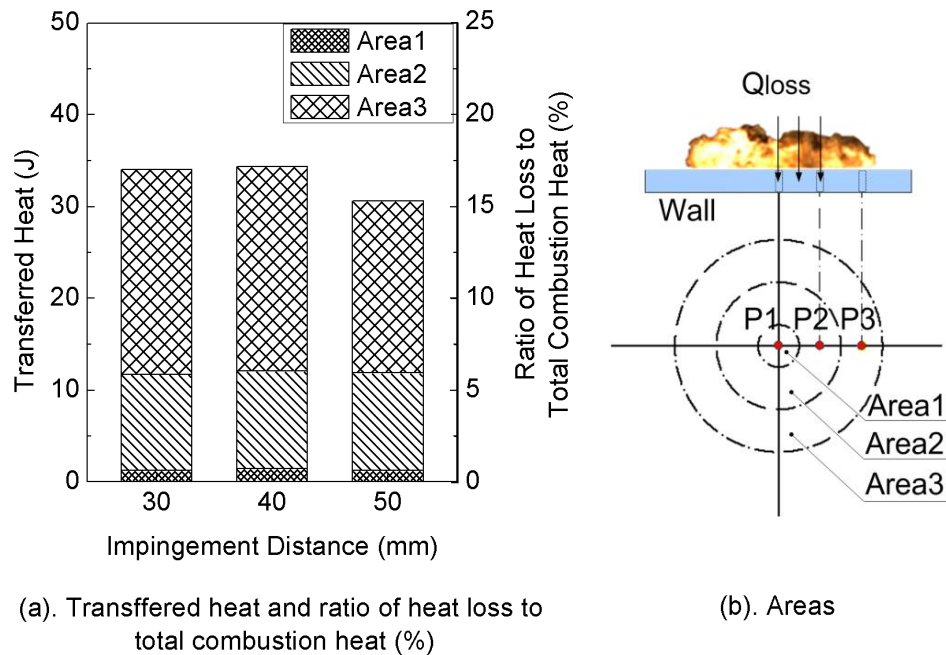


Figure 4.12 Comparison of the areal transferred heat and ratio of heat loss to total combustion heat at different distances

Figure 4.12 shows a comparison of the areal transferred heat. As an outer area is wider, the areal transferred heat becomes larger with outer radial position. The heat transfer area is more influential to this value than the heat flux at each point. Therefore, heat flux of Position3 most affects the total transferred heat as mentioned in previous section. The impingement distance 40 mm has the maximum heat loss on the wall. As totaled flame area shown in Figure 4.9 (c) has similar relation with impingement distance, flame contact area may have dominant effect for heat loss. The larger flame contact during resident time on the wall leads high wall

surface temperature, therefore it is important to decrease flame contact for improving heat loss. Figure 4.12 also shows the ratio of heat loss through the wall to total combustion heat at different impingement distances. It is about 14 to 15 % of total combustion energy.

4.6 SUMMARY

The effects of impingement distances (30 mm, 40 mm, and 50 mm) on transient local heat flux, combustion and soot distribution in diesel like conditions were investigated in this chapter. The main conclusions are summarized as follows.

1. By using the high speed video image analysis, we found that combustion was slow with low temperature small flame at large impingement distance.
2. By applying TFTHF sensors on the impingement wall, we could obtain transient heat flux. Transient heat transfer by impinging spray/flame is mainly caused by the turbulent convection through detailed analysis of the heat flux waveform.
3. Flame contact area of wall affects heat transfer to the wall. Among the 3 different distances, 50 mm showed the least heat transfer to the wall. This was caused by slow combustion and small flame contact area.
4. It was found that the correlation of flame temperature in near the wall with the local heat flux reach peak value. This high temperature near wall is one of the contributing factors in heat transfer rate to the wall.
5. Variation of impingement distance has an important role in the spray behavior, combustion development, soot emission and then heat loss. At $D_{imp} = 50$ mm, KL factor and temperature have the same variation in which both decreasing. With longer impinging path, fuel air mixing improves before impingement occurrence which resulting combustion is enhanced and then decreasing in soot luminosity.

CHAPTER 5

EFFECT OF INJECTION PRESSURE AND NOZZLE HOLE DIAMETER

5.1 INTRODUCTION

Recently, kind of control parameter and physical factor such as injection condition and nozzle parameter have been paid much attention as optimization of engine combustion strategies in modern diesel engine. These strategies of course has an impact on fuel economy, thermal efficiency, emission, and performance in engine. To clarify the influence of the injection pressure and nozzle parameter on the thermal efficiency, energy lost in total fuel conversion energy caused by heat loss will be studied. Therefore, in this chapter, focusing on the heat loss caused by the collision spray flame with of the injection pressure and nozzle was observed parametrically.

5.2 EXPERIMENTAL CONDITIONS

The injector and injector condition under various injection pressures and nozzle hole diameter are shown in Table 5.1 and 5.2 respectively. In this chapter, the attentions were paid to investigate the effect of injection pressure and nozzle hole diameter on heat transfer impinging spray/flame. Under injection pressure, nozzle hole diameter was kept at 1.33 mm as baseline condition and 80, 120, 180 MPa were selected to investigated injection pressure. On the other hand, injection pressure was kept at 120 MPa and 1.33 and 1.22 mm were chosen in

Table 5.1 Injector and injection conditions under various injection pressures

Injector type	Piezo actuator type
Number of nozzle holes	1
Injection quantity (mm ³)	5
Diameter of nozzle holes (mm)	0.133
Injection pressure/duration of injection (MPa/ms)	80/1.4, 120/1.2, 180/0.9

order to discussion on effect nozzle hole diameter. The experimental and impingement wall conditions are shown in Table 5.3. Gas density was set 16 kg/m^3 and impingement distance of 40 mm was carried out in all of conditions.

Table 5.2 Injector and injection conditions under various nozzle hole diameters

Injector type	Piezo actuator type
Number of nozzle holes	1
Injection quantity (mm^3)	5
Diameter of nozzle holes (mm)	0.133, 0.122
Injection pressure (MPa)	120
Nozzle hole diameter/duration of injection (mm/MPa)	0.133/1.2, 0.122/1.25

Table 5.3 Experimental and impingement wall conditions

Ambient condition	Non-Evaporation	Evaporation and Combustion
Ambient gas	N_2	Combustion: Air (N_2 :79%, O_2 :21%) Evaporation: N_2
Ambient pressure (MPa)	1.4	4.1
Ambient temperature (K)	300	873
Ambient density (kg/m^3)	16	←
Fuel	Diesel Fuel	←
Impingement wall	Flat plate, Stainless steel	←
Impingement distance “ D_{imp} ” (mm)	40	←
Wall temperature (K)	300	460 ± 10
Cooling method	-	Oil cooling

5.3 NON-COMBUSTION SPRAY BEHAVIOR AND WALL HEAT TRANSFER UNDER INJECTION PRESSURE

5.3.1.Spray behavior

In this section, effect of the injection pressure on the spray motion was investigated under non-evaporating and evaporating non-combustion. The injection rate under injection pressure is shown in Figure 2.2 (a). In order to maintain the same fuel quantity, injection durations were changed by the pressure. Figure 5.1 shows non-evaporation wall impinging spray images at different injection pressures at room temperature. At 0.1 ms ASOI, the images

revealed that higher injection pressure made the spray faster from top to bottom. These spray leads to impingement to wall at 0.4 ms ASOI in which shorter impingement timing than both injection pressure of 80 and 120 MPa. When time is increased to 0.7-1.2 ms ASOI, the spray undergoes impingement in both injection pressure of 80 and 120 MPa. However, at injection pressure of 180 MPa, spray development was enhanced then there became larger spray spreading to the circumferential area of the flat wall. From images, it is noteworthy that as the injection pressure increases, spray radius and spray height increase. Larger spray tangential and normal velocities with increasing injection pressure are thought to be responsible for this spray formation [50].

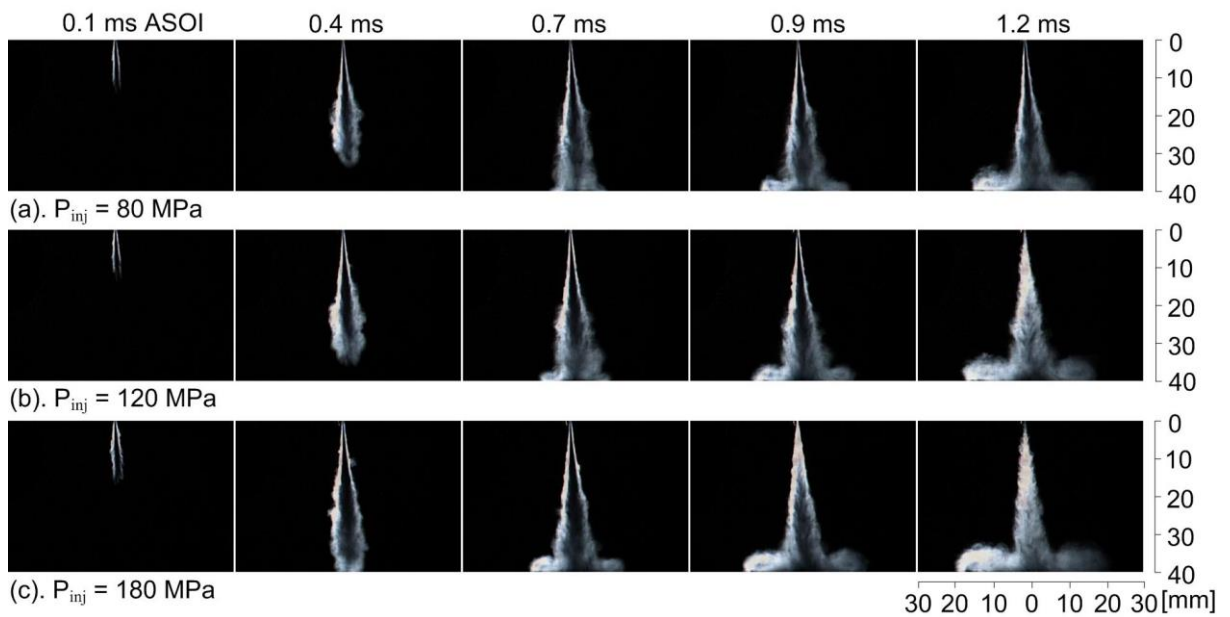


Figure 5.1 Non-evaporating wall impinging spray at different injection pressure

Non-combustion evaporating spray images under the three injection pressures at high temperature (873K) are shown in Figure 5.2. From this figure, at 0.1 ms to 1.2 ms ASOI, liquid phase could not impingement on the wall. The spray almost evaporated before impinging to the wall. As Pickett et. al [69] pointed out, the liquid phase eventually reaches an axial position where it is completely vaporized as hot gases entrain into the spray. Following, liquid phase fluctuates throughout the injection duration, whereas vapor phase continues to penetrate downstream. In case of injection pressure 80 MPa, liquid fuel existed till later period compared

with the other pressures. As shown in the injection rate graph, lower injection pressure requires longer injection duration. The figure shows that 120 and 180 MPa images show smaller liquid phase areas compared with 80MPa. This means that an increase in velocity with higher injection pressure leads to more effective atomization. Consequently, more homogeneous mixture distribution takes place due to faster evaporation rate. As it can be seen in Figure 5.2 (c) at 0.7 ms ASOI, some fuel droplets spread on the wall, which accounts for why some fuel droplets impinge earlier on the wall.

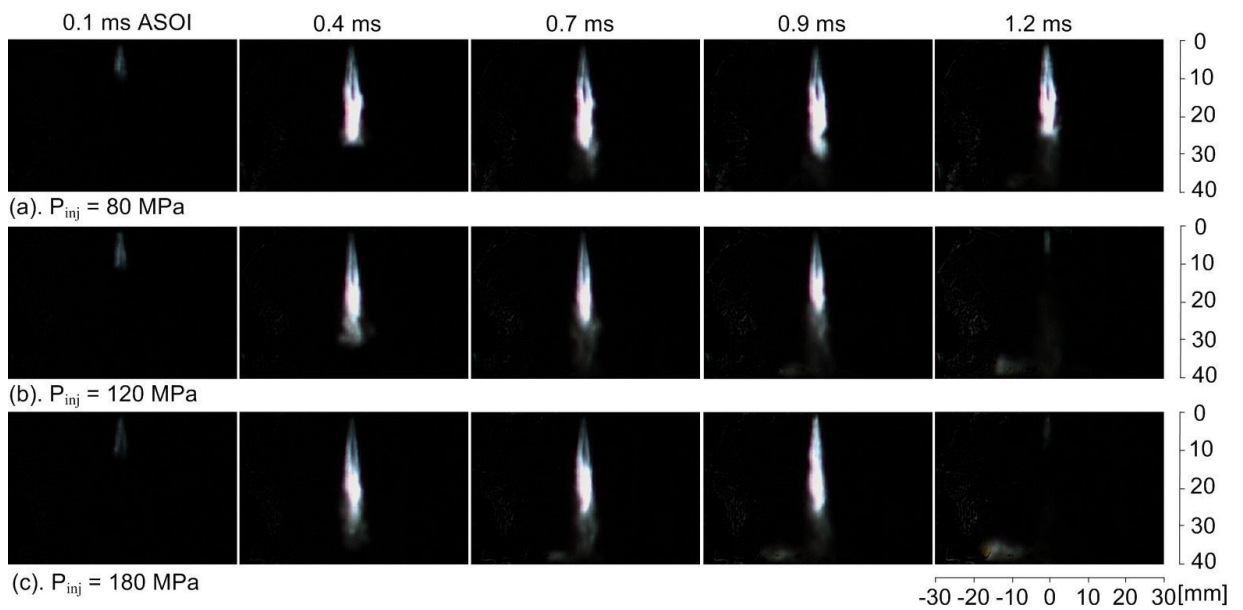


Figure 5.2 Evaporating wall impinging spray (liquid component) at different injection pressure

Spray tip penetration lengths under different injection pressures obtained from the non-evaporating images are plotted in the Figure 5.3. Closed and open markers show before and after the spray impingement on the wall, respectively. The penetration pattern of each injection pressure is different in respect of before or after impingement on the wall with different injection duration. In Figure 5.3, we can see that the higher injection pressure made further spray tip penetration. If the injection pressure rises, the spray droplet velocity increases. As a consequence, it leads to increase in fuel momentum, which results in earlier impingement timing and larger spray tip penetration. However, after injection duration complete at all

injection pressure, the tip penetration becomes almost identical eventually despite the pressure difference.

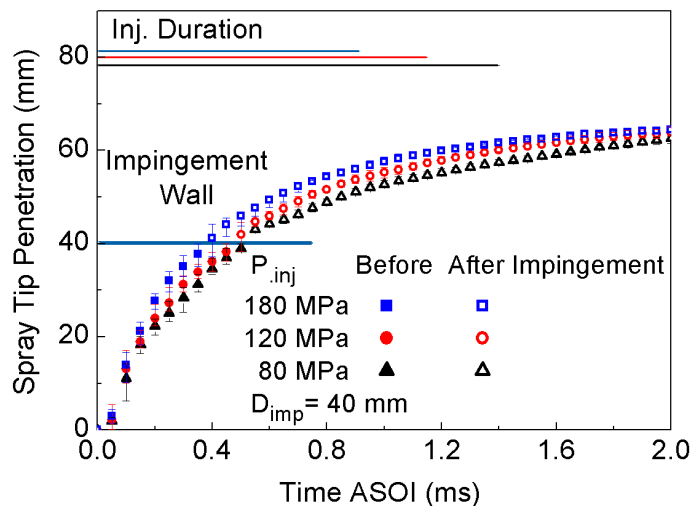


Figure 5.3 Spray tip penetrations non- evaporating spray at different injection pressure

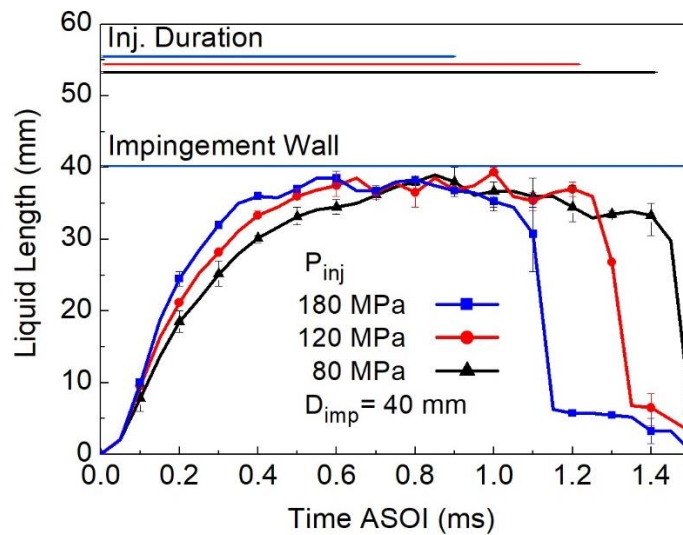


Figure 5.4 Liquid lengths of evaporating spray at different injection pressure

Liquid penetration lengths with different injection pressures obtained from the non-combustion evaporation images are plotted in the Figure 5.4. The lengths, which was defined similar to the non-evaporating spray, were obtained by the image processing as the maximum liquid penetration during the injection using a pre-determined threshold intensity. Liquid phase fuel, i.e. the liquid penetration length, was obtained from the non-combustion evaporation images. The liquid length linearly increased with time for a few hundred-microsecond ASOI.

Higher injection pressure lead to a faster penetration velocity, however, they reached similar distance at a maximum. The maximum liquid penetration lengths were around 35-40 mm. Liquid length with slight fluctuation remained constant even though fuel continued to be injected. During this Quasi-Steady Period, liquid penetration length was nearly constant at all injection pressure even though their injection rate profiles ware different. This implies accelerated evaporation occurred at the spray tip. The phenomenon suggests that the higher injection pressure lead to enhanced evaporation rate for wider area. The average mixture temperature decreased by evaporation. As a result, heat fluxes at non-combustion increased much lower than combustion case. After the Quasi-Steady Period ended, the liquid length immediately dropped just after the end of injection.

5.3.2.Heat Flux on the Wall Surface

To examine the effects of the injection pressure, heat fluxes in non-combustion condition were measured. Figure 5.5 shows temporal variation of the local heat fluxes and the total heat fluxes. Each of (a-c) shows local heat fluxes at the positions at 80, 120 and 180 MPa. The local heat flux appears simple waveform due to combustion is not occur in evaporation condition [111]. As explained in the previous section, the unsteady wall heat transfer occurred due to the spray impingement on the wall. This is true for these results. By increasing injection pressure, starts of local heat flux increase became earlier, which were associated with the increased spray velocity. That is to say the higher pressure leads to the earlier turbulent convection.

Higher injection pressure made total local heat flux increase earlier with a maximum value of 2.11 kW as shown in Figure 5.5 (d). It increased the total heat flux due to higher velocities as a consequence of an increased fuel injection rate. These higher velocities led to hot gas flow toward to wider wall area. This was evident by local heat flux at Position3 which start to increase earlier as shown in Figure 5.5 (c). As mentioned in the previous section, the area was influential factor for the temporal variations of averaged total heat flux.

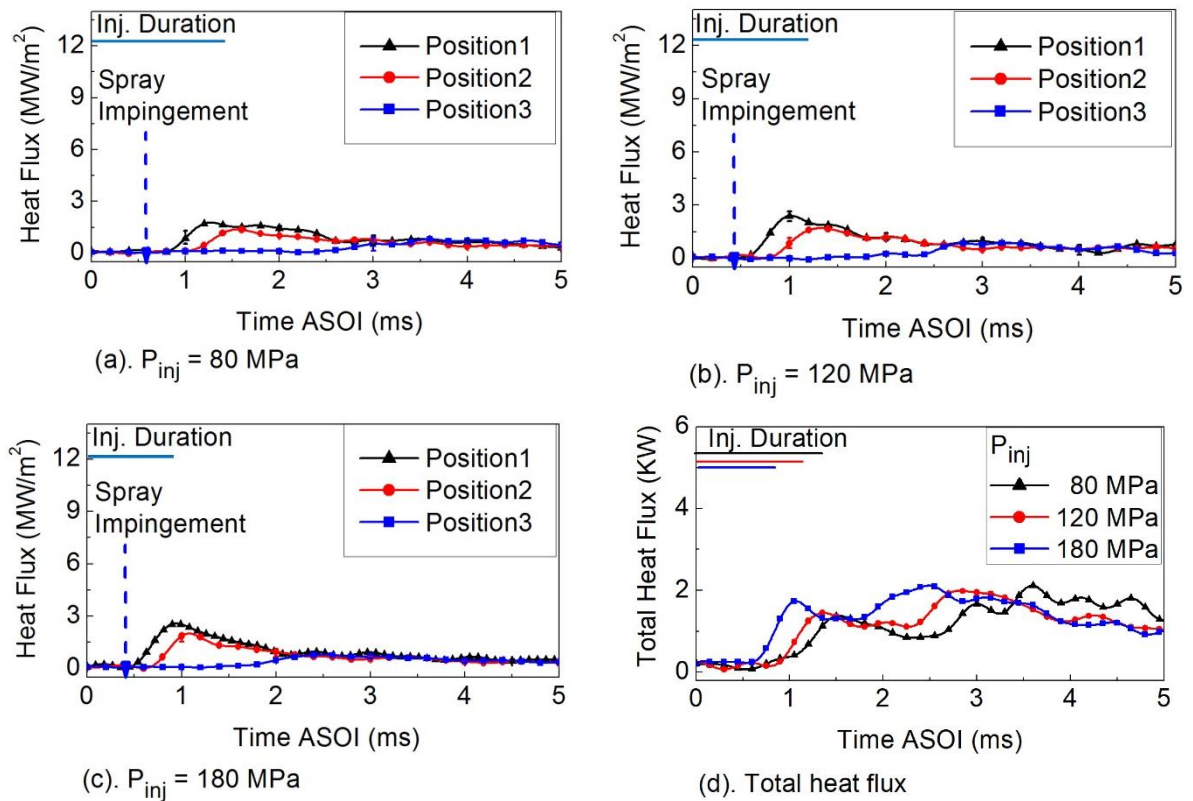


Figure 5.5 Temporal variation of local heat flux and total heat flux at non-combustion

5.4 COMBUSTION FLAME BEHAVIOR AND WALL HEAT TRANSFER UNDER INJECTION PRESSURE

In this section, behaviors of the impinging flame and how combustion affects the wall heat transfer under the different injection pressures are studied. Effects of the three injection pressures, i.e. 80, 120, and 180 MPa were investigated.

5.4.1. Combustion Flame Behavior

Figure 5.6 shows images of impinging flame at different injection pressures. Comparing with non-evaporating spray photographs in Figure 5.1, luminous flames occur a few hundred micro-seconds after the spray impingement. It is evident from Figure 5.6 that luminous flame appeared earlier with higher injection pressure. At 0.9 ms ASOI, flame luminosity was occurred at injection pressure 120 and 180 MPa. In contrary, flame luminosity unfound at 80 MPa. It means increasing injection pressure is to promote greater premixing between fuel and air and it leads shorter ignition delay. Flame natural luminosity was detected at injection pressure 80 MPa

when time is increased to 1.2 ms ASOI. In this timing, injection 180 MPa reached most brightness in flame luminosity. In all conditions, combustion occurred just after the spray impingement on the wall and it began before the end of the fuel injection.

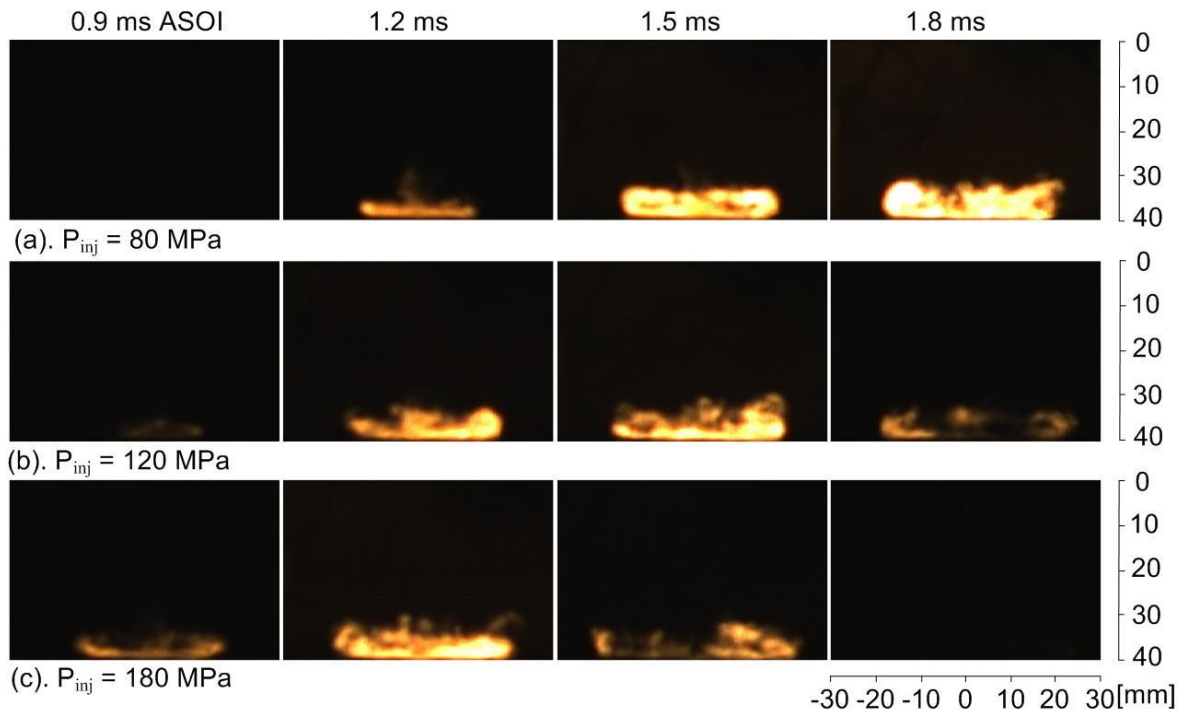


Figure 5.6 High-speed video camera images of impinging flame at different injection pressure

A comparison of the images between non-evaporating spray and combustion flame revealed that the spray development at non-evaporating and spray flame growth at combustion were significantly enhanced with increasing injection pressure. Furthermore, comparing the photographs of non-combustion in Figure 5.2 and combustion in Figure 5.6, it can be seen that the luminous part by combustion existed in the vapor area. The combustion occurred in the vapor area near the center of wall impingement.

At time is 1.5 to 1.8 ms ASOI, in case of 180 MPa, flame luminosity started to decrease and then disappeared. Similarly, injection pressure 120 MPa demonstrated flame luminosity start to decrease at timing of 1.8 ms ASOI. However, under 80 MPa, the flame natural luminosity continuous to develop in this timing. Since the natural luminosity mainly comes from soot incandescence in diesel flame, this lower injection pressure of 80 MPa, more flame

natural luminosity was observed. It is because lower velocity lead to decreasing in atomization and fuel air-mixing.

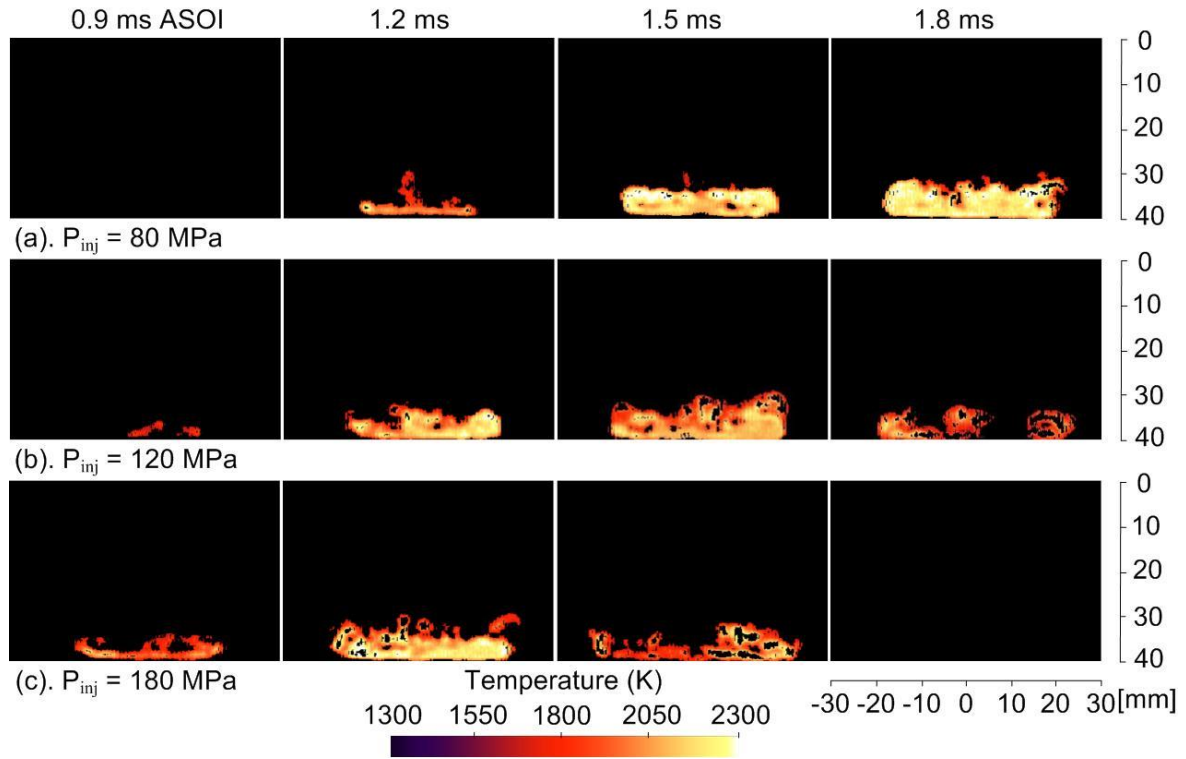


Figure 5.7 Flame temperature distribution at different injection pressure

Information of temperature distribution of impinging spray/flame is important for the heat transfer analysis. Figure 5.7 shows flame temperature distributions at different injection pressures obtained from two-color method analysis, which was performed with flame natural luminosity images. The temperature distribution shapes were similar to those of flame, because they were obtained from the flame luminosity and could not be obtained from non-luminous area. The color distribution scale varying from dark to bright indicates temperature.

By comparing the temperature distributions with different injection pressures, it was presented that temperature distribution was most spread to wider area and its complete earlier at high injection pressure. On the other hand, it was opposite when injection pressure was lower. This phenomenon contributed in heat transfer rate on the wall in term of timing of rises and its value at each position. Even though the ignition timing, combustion duration and flame growth rate in graph 5.8 (a) under different injection pressure were different each other. However, the

different of maximum temperature under injection pressures were around 100 K. As shown in flame temperature distribution image, it can be expressed as the maximum flame temperature distribution when time was 1.2, 1.5 and 1.8 ms ASOI at injection pressure of 180, 120 and 80 MPa. At these timing, it can be seen that the distribution of temperature value almost uniform at 80 MPa than the others. Consequently, it had the highest mean temperature as shown in graph 5.8 (b). These phenomena can be explained as follows. At lower injection pressure of 80 MPa, more flame natural luminosity was observed, which was related to temperature and soot volume fractions. In this condition, soot is dramatically higher which is contributed by less air entrainment with decreasing in spray atomization and fuel air-mixing and therefore bring it to local high equivalent ratio. The correlation of high temperature with local high equivalent ratio is commonly discussed for being account for soot production. In contrast, natural flame intensity for an injection pressure of 180 MPa was reduced. High injection pressure is more air entrainment with improving in spray atomization and premixing between fuel and air due to high velocity which causes reducing in soot formation.

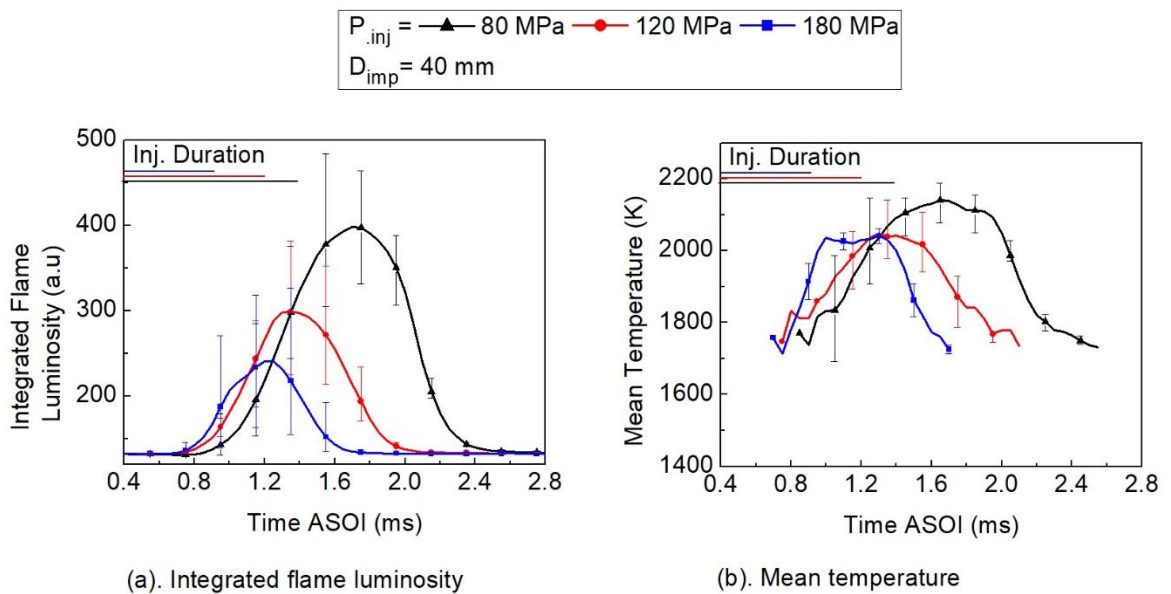


Figure 5.8 Integrated flame luminosity and mean temperature at different injection pressure

5.4.2. Heat Flux on the Wall Surface

Unsteady temporal variation of local heat flux values of flame impingement on the wall and integrated flame luminosity under each injection pressure shown in Figure 5.9 (a-c). Spray impinging and ignition timing have been also plotted on the graph. Time histories of local heat

fluxes at each position was discussed in the previous section. There were significant differences local heat flux waveform under injection pressure variations in terms of time of roses and peak values. These differences can be attributed to flame velocity differ at each injection pressure.

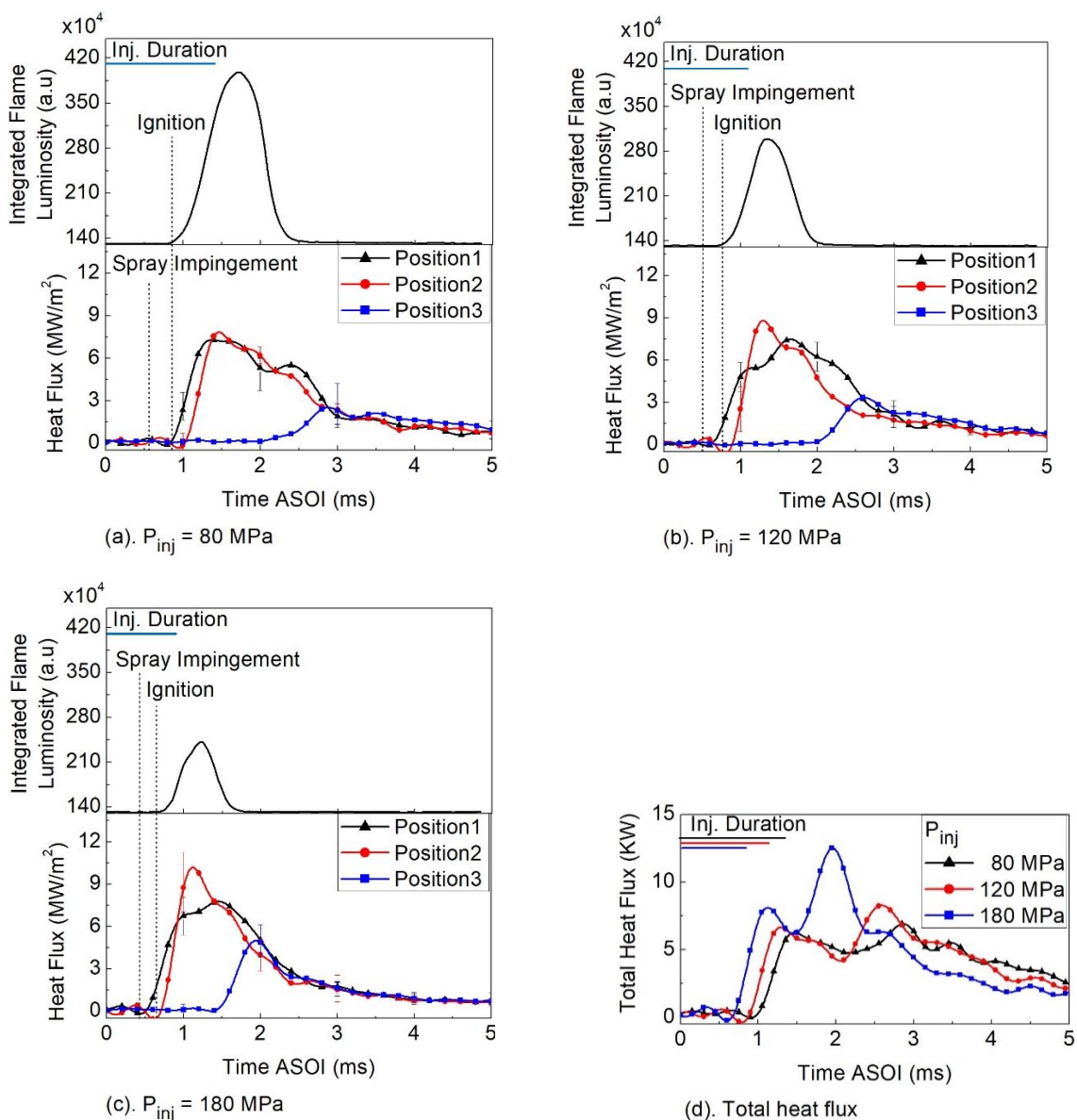


Figure 5.9 Temporal variation of local heat flux, integrated flame luminosity, and total heat flux at combustion

The effect of injection pressure in relation to local heat flux, it could be found from the graphs as follow: At lower injection pressure i.e. 80 MPa, the local heat fluxes of Position1 increased simultaneously with the ignition. One possible explanation is that the convection by turbulence from spray impinging takes time to reach the wall as can be seen in Figure 5.3. In

the case of increasing injection pressure, thus increasing injection velocity, leads to higher kinetic energy in which fuel travels further distance. As a result, spray impingement and ignition occur at a faster rate with higher injection pressure. It also found that a higher peak value of local heat flux was detected at all positions because increased flame velocity which is caused by an increased injection rate. These increasing flame velocities were toward to wider wall area, which is responsible for local heat flux at Position3 increased. This Implies that increasing flame velocity is due to high injection pressure can accelerate the rate of heat transfer to wall.

Figure 5.9 (d) shows temporal variation of the total heat flux at different injection pressures. It can be seen in the graph, all of the waves had two peaks i.e. there were two stages for the local heat transfer. At first, the local heat flux was increased by turbulence of impingement spray. Then, heat transfer by flow along the wall, which started after impingement, took place. The result showed that a maximum total heat flux value of 16.5, 8.2 and 6.9 kW for injection pressure of 180, 120, and 80. According to the more substantial amount of total heat flux, it can be concluded that the increasing flame velocity because high injection pressure causes more energy loss to the wall.

A comparison of the transferred heat at each area under different injection pressures between non-combustion and combustion are presented in Figure 5.10 (a-b). This figure shows transferred heat in vertical axis on the left-side graph and ratio of heat loss to total combustion heat in vertical axis on the right-side graph. As can be seen in figure non-combustion condition, the value of transferred heat was around 11-12 joule at different injection pressure. This heat transfer was occurred by convection mainly from flow induced by the fuel spray injection during injection period. However, it has a small amount of the effect when injection pressure increased. In case of combustion, the transferred heat increased significantly, and it is also found that the highest transferred heat is observed at 180 MPa among lower injection pressure both. The flame velocity, which relates to heat transfer coefficient that will be explained in the next figure, increased with the injection pressure and leads to hot gas flow spreading to the circumferential area of the flat wall. Comparing non-combustion and combustion, around 30% of the transferred heat through the wall was transferred by the convection of non-combustion

evaporating spray. Of total combustion heat loss, the ratio to the wall was shown in the graph 5.10. It comprises approximately 12 to 14% of total combustion energy.

h is one of the decisive factors which influence on the heat transfer loss through wall. Temporal local heat transfer coefficients which were calculated by equation (2.22) with the measured heat flux at non-combustion and combustion conditions at different injection pressures are shown in Figure 5.11. As the gas temperature at non-combustion, we used temperature near wall which was obtained by the simulation. The gas temperature at combustion, which used in the convective h equation, was obtained from two-color method analysis. The graph shows that the peak values differ at both conditions because of not only turbulent convection by gas flow but also radiation which varies locally and temporally.

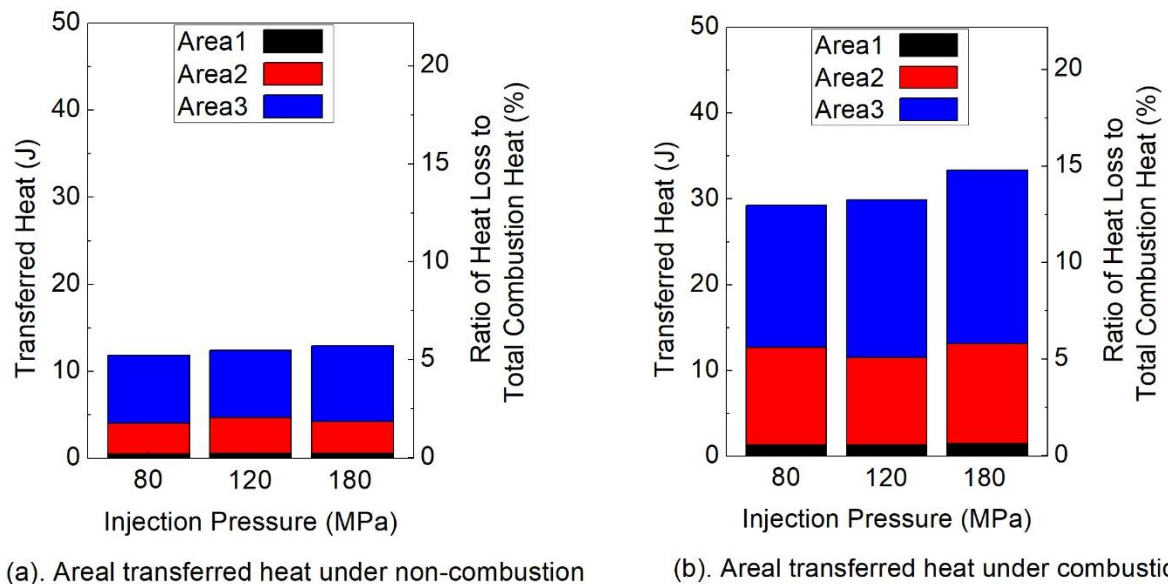
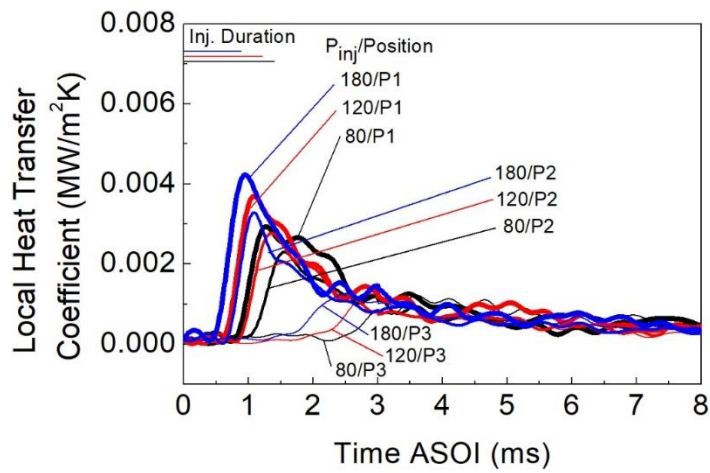


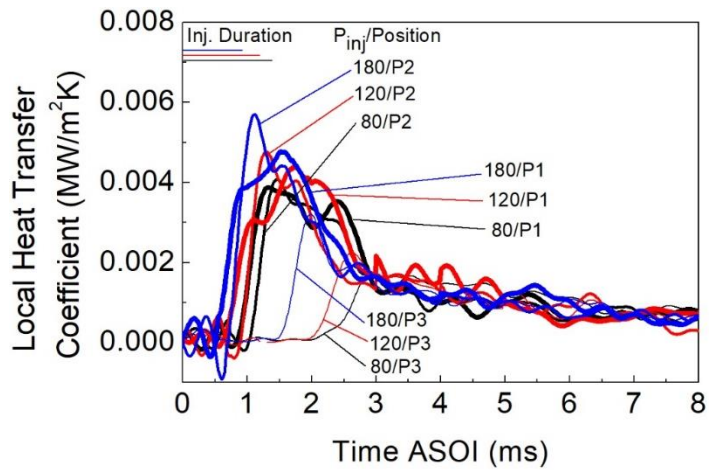
Figure 5.10 Comparison of the areal transferred heat and ratio of heat loss to total combustion heat between non-combustion and combustion at different injection pressure

Furthermore, in this condition, the combustion flame most developed around the location somewhat distant from the impingement center. Consequently, the location of Position2 had a higher value than that of others in all injection pressures. However, the graphs showed that both combustion and non-combustion conditions have similar waveforms and order of heat transfer coefficient at both all the positions and injection pressures. This indicates

that, in combustion, flow induced by the injected spray is dominant for the heat transfer to the wall.



(a). Non-combustion



(b). Combustion

Figure 5.11 Comparison of local heat transfer coefficient between non-combustion and combustion at different injection pressure

Both graphs show that the local heat transfer coefficient increased proportionally in all positions with injection pressures. It means higher injection pressure, which increases momentum and velocity of the fuel spray, is one of the significant influential factors on the α . In other words, higher injection pressure leads to larger local heat flux value as shown in Figure 5.5 and 5.9. Similarly, the dominant factor of heat loss variation under injection pressure could be the heat transfer coefficient differences caused by the spray flame flow changes [112]. If the heat transfer coefficient at the non-combustion condition fully contributed to the total heat

transfer in figure 5.11 (a), spray motion contributed 30 to 40 % for the total transferred heat under the combustion condition.

5.5 COMBUSTION FLAME BEHAVIOR AND WALL HEAT TRANSFER UNDER DIFFERENT NOZZLE HOLE DIAMETERS

In this section, the effects of nozzle hole diameter on flame temperature distribution and local heat flux were investigated. The nozzle hole diameters (D_{hole}) were selected as 0.133 and 0.122 mm. The injection pressure and impingement distance were set at 120 MPa and 40 mm for both nozzle hole diameters.

5.5.1. Combustion Flame Behavior

Heat transfer by convection may be formed significantly when gas or flame temperature much different with wall surface. These gas or flame temperature distribution become important since heat loss on the wall much affected to the large area. In order to understand this effect, flame temperature distribution at different nozzle hole diameter is presented in Figure. 5.12. The different injection rate at different nozzle hole diameters are shown in Figure 2.2 (b). At the same fuel injected, larger nozzle hole diameter required in increasing injection rate value and shorter injection duration. As a consequence, momentum and velocity become larger as the value of injection rate increased.

At the flame temperature distribution, the figures did not show any significant difference between both nozzle hole diameter as far as temperature concentration is concerned. However, larger temperature distribution was observed at $D_{\text{hole}} = 1.22$ mm. As it was confirmed that a smaller hole size nozzle produced smaller droplet sizes and a smaller amount of particulate [113]. It is straightforward to atomization and air entrainment into the spray. As a result, the combustion development into outer periphery of the spray flame, as a consequence of air entrainment [9].

Figure 5.13 shows distribution of axial flame temperature from wall surface at each sensor at 1.5 ms ASOI, when they are at combustion peak, by nozzle hole diameter. The figure shows that temperature distribution is varying in the axial direction in that time. It implies strong combustion gas turbulent flow exist together with the combustion reaction. It also confirmed

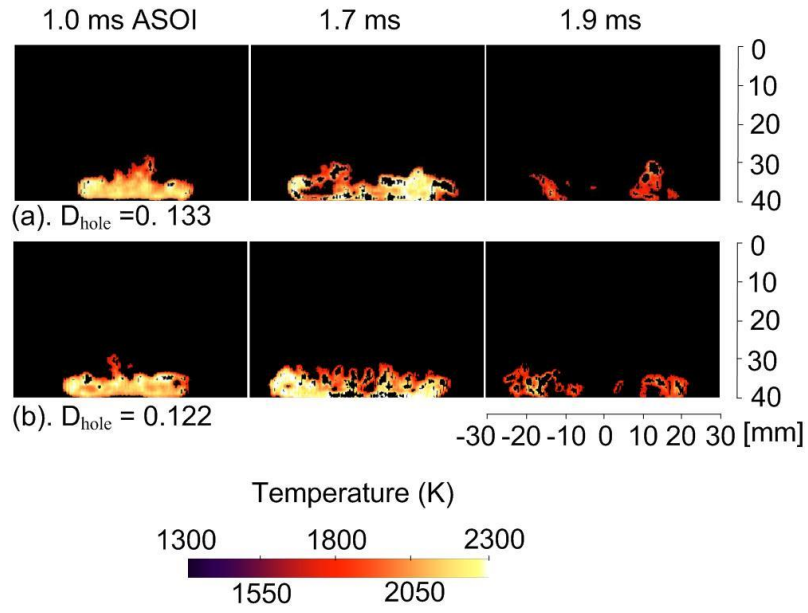


Figure 5.12 Flame temperature distribution at different nozzle hole diameters

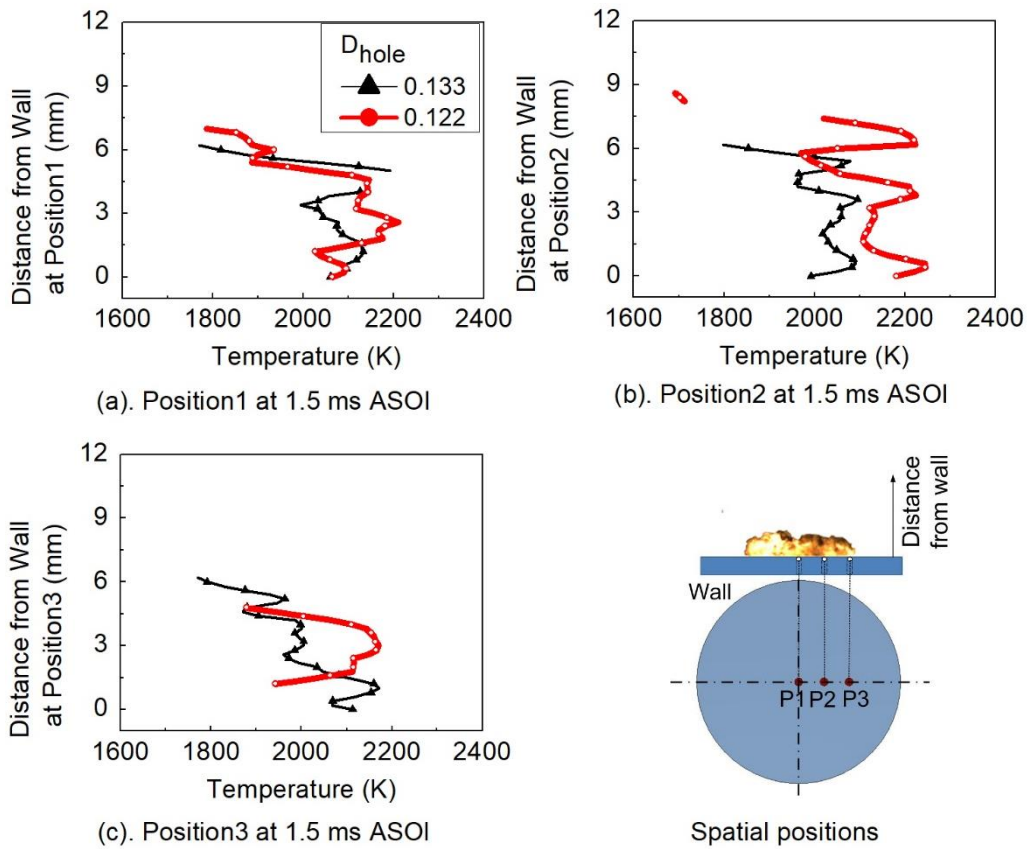


Figure 5.13 Temperature distribution from wall surface at different positions

that temperature higher along the wall surface then decreases with increasing distance from wall surface. At Position1, the temperature distribution almost similar each nozzle hole

diameter. When area is increases to Position2, the temperature values increase further with smaller nozzle hole diameter, 0.122 mm. Improved mixture due to the fuel atomization effect on ambient air entrainment play important role in this temperature increase. At Position3, distribution of axial temperature slightly smaller. Far away from the center of impingement and creating flame vortex are possibility reason in this phenomenon.

Considering the effect of nozzle hole diameter on flame contact area is presented in Figure 5.14. When flame on the wall start to develop to radial area, flame contact increased linearly with the time and both nozzles almost similar until timing of 1.6 ms ASOI. After this timing, flame contact at $D_{hole} = 1.33$ mm started to collapse. However, due to longer injection duration at $D_{hole} = 1.22$ mm, flame contact continues until it reached the maximum value though it eventually collapsed. Apart from this slightly flame contact different, Figure 5.13 shows how long the resident time the flame contact area on the wall. It was found that smaller nozzle hole diameter was longer flame contact period on the wall. It can be thought more rate of heat transfer at $D_{hole} = 1.22$ mm due larger area affected.

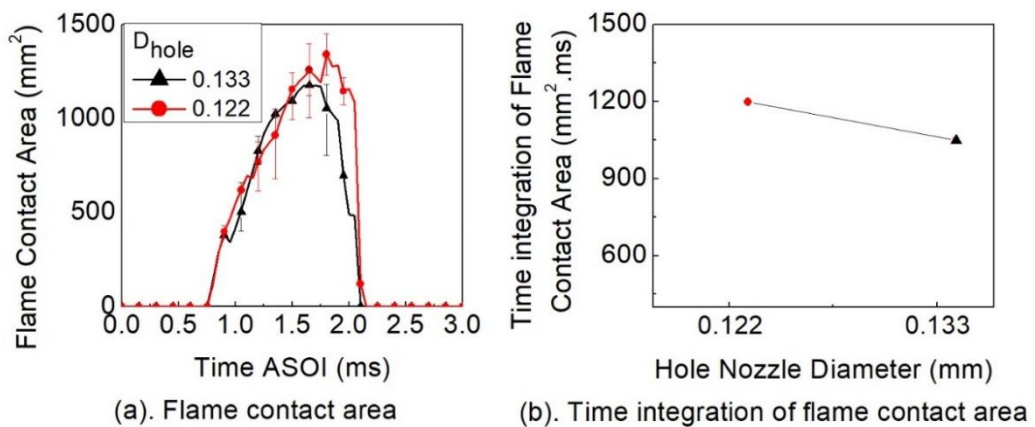


Figure 5.14 Flame contact area and time integration at different nozzle hole diameters

5.5.2.Heat Flux on the Wall Surface

To clarify the effect of nozzle hole diameter on the heat transfer characteristics, the local heat flux and ratio of heat transfer to total combustion were examined. Figure 5.15 (a-c) presents the data on local heat flux characteristics and total heat flux. The upper and bottom graph shows non-combustion and combustion local heat flux. In this section, comparison nozzle hole

diameter different were discussed both local heat flux of combustion and non-combustion. Comparison between non-combustion and combustion local heat flux itself has discussed in detail in the previous section. At non-combustion condition under nozzle hole diameters, the marked observation to emerge from the data comparison was heat flux rises at Position1 became earlier and higher at $D_{\text{hole}} = 1.33$ mm in which larger nozzle hole diameter. It increased due to higher momentum and velocities as a consequence of an increased fuel injection rate. The maximum peak value at Position1 was around 2.3 MW/m^2 both nozzle hole diameter.

In the case of combustion condition, the higher heat flux value at Position1 and 2 were obtained at larger nozzle diameter as shown in Figure 5.15 (a). This shows that increased impinging flame velocity correlated to increase in local heat flux value, rather than the effect of flame temperature. Considering the effect of flame temperature near wall as shown in Figure 5.13 (b), area at Position2 reached the maximum temperature in which was responsible to local heat flux at position2 increased to peak value at both nozzle hole diameter. However, due to more combustion development to wider area at $D_{\text{hole}} = 1.22$ mm as shown in Figure 5.12 (b), as a consequence Position3 was increase earlier and higher. More air entrainment and with improving in spray atomization was achieved at small nozzle hole diameter, as a result flame develops into the wider circumferential area.

Figure 5.15 (c) shows temporal variation of total heat flux at different nozzle hole diameter. As a result, we can see in the graph (i.e. combustion case) that hole size diameter of 0.122 mm has a maximum peak value in the second stage. Although the higher heat flux value was obtained at larger nozzle hole diameter as shown in Figure 5.13 (a). However, small nozzle hole diameter was affected higher local heat flux at Position 3 as we can see in Figure 5.13 (b). As mentioned in previous section the heat transferred over a larger area has more influence on the total heat flux value. The non-combustion results have a number of similarities with combustion case findings. However, in non-combustion, the differences between the two are very small, such as the maximum value of 1.6 kW for $D_{\text{hole}} = 1.22$ mm and 1.4 kW for $D_{\text{hole}} = 1.33$ mm.

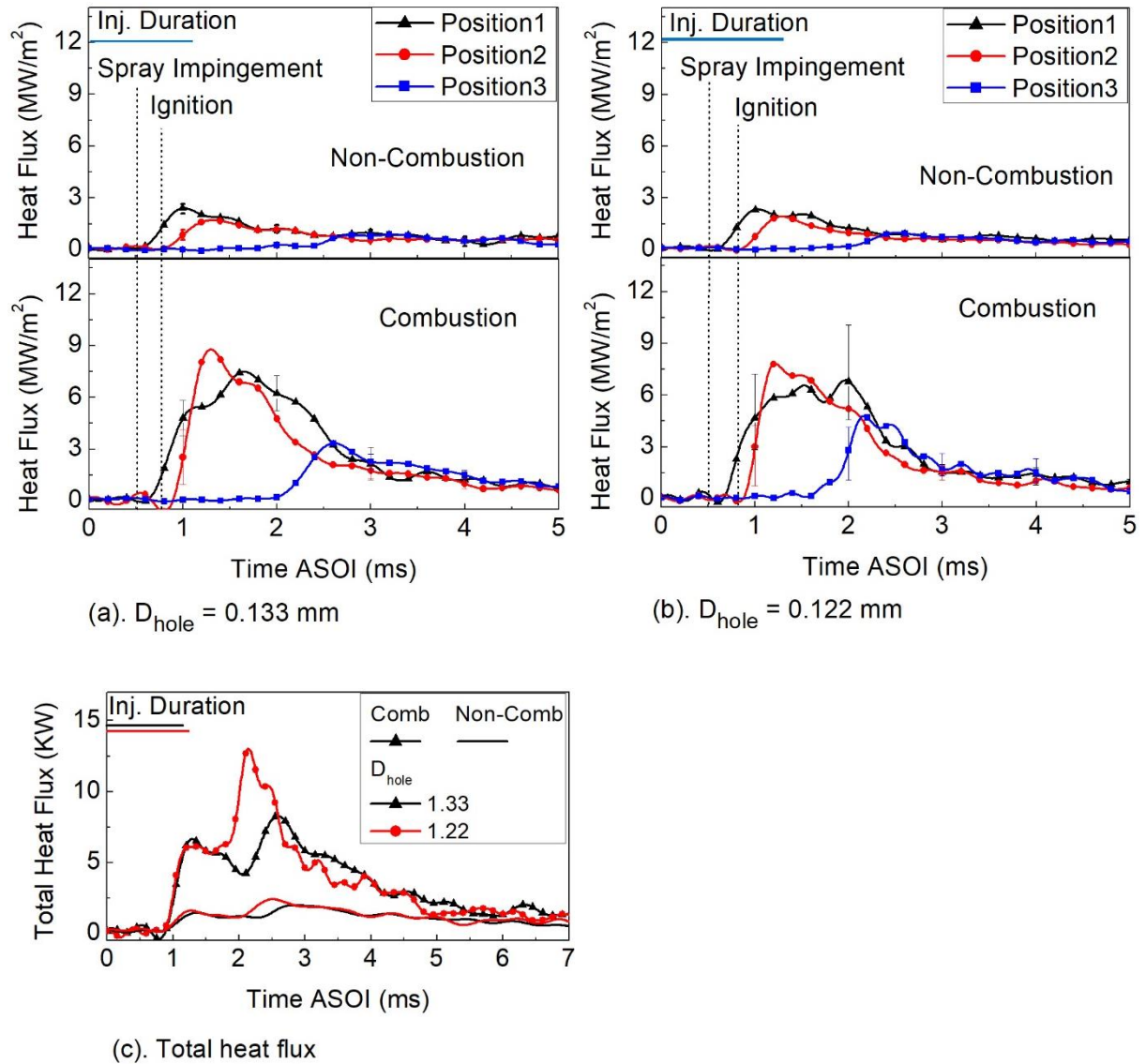


Figure 5.15 Local heat flux and total heat flux at different nozzle hole diameters

Figure 5.16 (a-b) shows a significant difference in the transferred heat at each area under different nozzle hole diameters between non-combustion and combustion conditions. These results also similar with total heat flux in Figure 5.15 (c), the differences were statically significant between both conditions. It is due to the primary heat transfer come by convection from flow induced by the fuel spray injection during injection period. At non-combustion condition in Figure 5.16 (a), the results show the comparison between different nozzle hole diameter did not significant effect on transferred heat. It was about 12-13 joules transferred heat from impinging evaporation spray to the wall. Based on these results, energy loss become 6%

from total combustion heat. If compared with combustion in Figure 5.16 (b), the proportion energy loss by evaporation non-combustion was around 30-40% energy lost. It was found that the convective heat transfer from spray induce during injection given important factor on energy loss.

When the combustion occurred, large amount of heat transfer was found as shown in Figure 5.16 (b). As can be seen in the figure, the value of transferred heat increases as nozzle hole diameter is decreased, the proportion of transferred heat was 32 joules when the nozzle hole diameter was 0.122 mm. It is assumed that the hot gas flow from combustion spreading to the circumferential area of the flat wall, because the smaller nozzle hole diameter with smaller droplet size diameter can promote spray atomization and entrainment. The result on the ratio of heat loss to total combustion heat was 14% at $D_{hole} = 1.22$ mm.

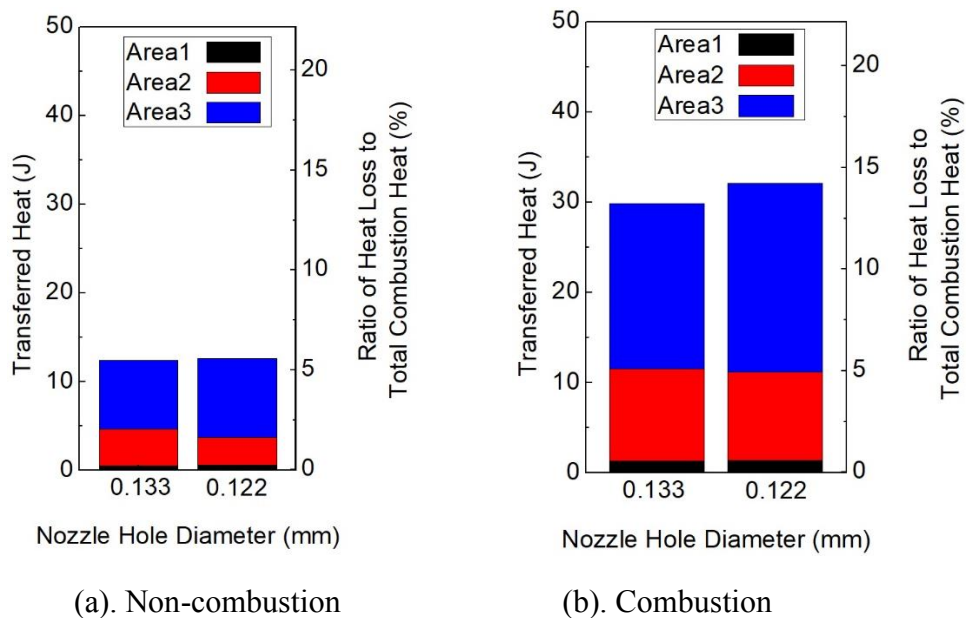


Figure 5.16 Comparison of areal transferred heat and ratio of heat loss to total combustion heat between non-combustion and non-combustion at different nozzle hole diameters

5.5.3. Effect Nozzle Hole Diameter and Injection Pressure on Areal Transferred Heat

As previously investigated, nozzle hole diameter has significant effect on atomization, fuel-air mixture and heat flux characteristics. Besides, injection pressure has also similar effect due to its velocity. In this subsection, further study was compared the effect of injection pressure and nozzle hole diameter. The aim was to understand to what extent this combination had effect

on transferred heat and ratio of heat loss to total combustion. The different nozzle hole diameters, $D_{\text{hole}} = 1.33$ and 1.22 mm were compared with injection pressure of 80, 120 and 180 MPa, respectively. The impingement distance was set at 40 mm regardless of injection pressure and nozzle hole diameter condition.

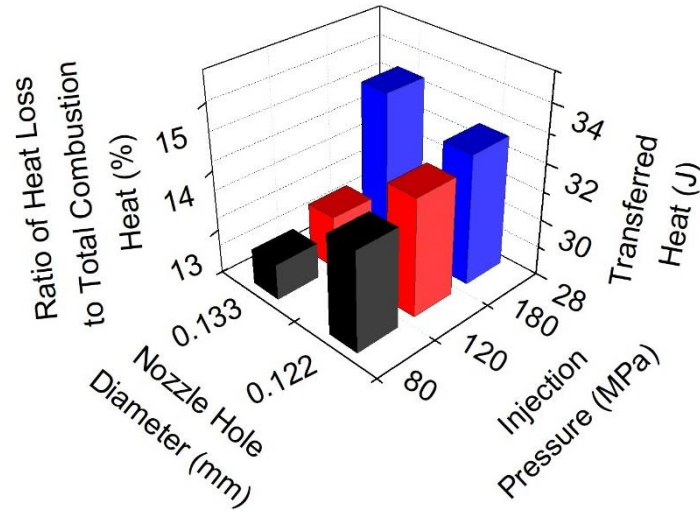


Figure 5.17 Comparison of the areal transferred heat at combined nozzle hole diameter/injection pressure

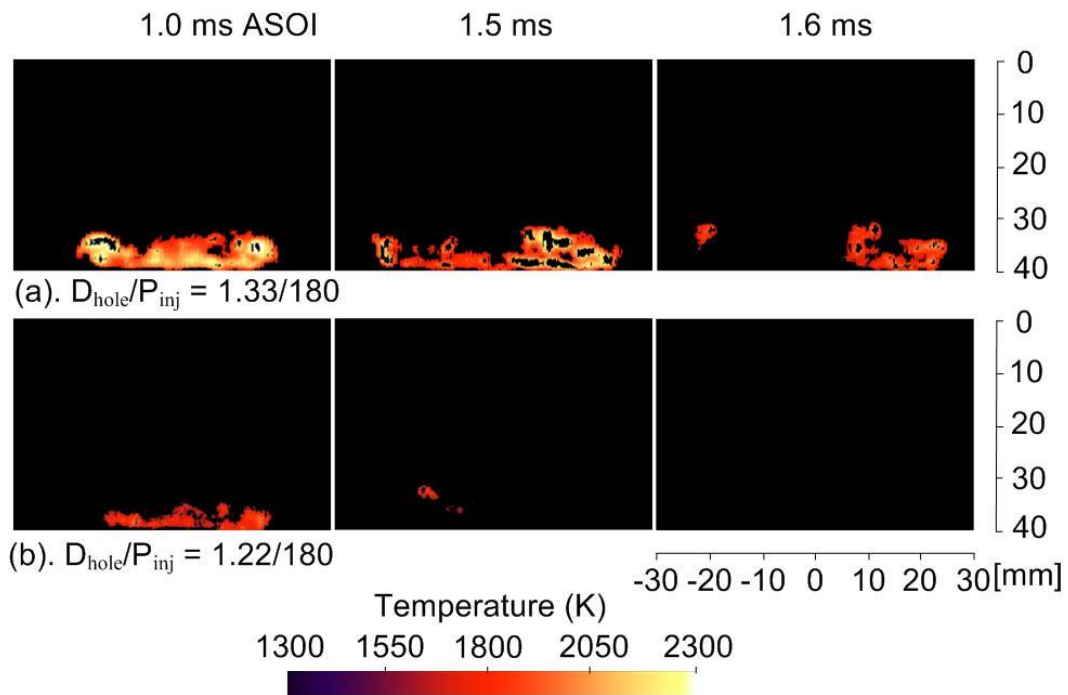


Figure 5.18 Comparison of temperature distribution at high injection pressure with different nozzle hole diameter

Comparison of the areal transferred heat at combination of nozzle hole diameter/injection pressure ($D_{\text{hole}}/P_{\text{inj}}$) are presented in Figure 5.17. As shown in the figure, the

transferred heat increased proportional with injection pressure at both nozzle hole diameter. These increases gradually at $D_{\text{hole}} = 1.22$ mm and at $D_{\text{hole}} = 1.33$ mm was transferred heat significant increased when it was high injection pressure. As described in the previous section, increasing injection pressure contributed to increases in flame velocity. These high turbulent flow combustion by high injection pressure and larger areal heat affected are the reason to influential to transferred heat rate in combined effect of injection pressure and nozzle hole diameter on wall heat transfer.

In the case of lower injection pressure, 80 and 120 MPa, larger nozzle ($D_{\text{hole}} = 1.33$ mm) generated lower heat loss as shown in Figure 5.17. Flame temperature, which is a dominant factor on heat loss at this injection pressure, decreases with increasing nozzle hole diameter [9]. On the other hand, in the case of injection pressure 180 MPa, larger nozzle generated more heat loss. High temperature end gases in outer boundary of the flame at the end of combustion largely determines this heat loss. It is evident that the temperature distribution was found develops further along the wall as shown in Figure 5.18. The flame contact area with a longer residence time at $D_{\text{hole}}/P_{\text{inj}} = 1.33/180$, is the reason why transferred heat increased further. However, when nozzle hole diameter decreased and pressure increased ($D_{\text{hole}}/P_{\text{inj}} = 1.22/180$), it can be more air entrainment and accelerated the fuel-air mixing then lead rapid combustion. As a result, resident time during impinging flame along the wall was decreased. Based on the Figure 5.17, ratio heat loss is around 13-15% to total combustion energy.

5.6 SUMMARY

This study is to clarify the effects of injection pressure and nozzle hole diameters on the impinging combustion wall heat transfer. The measurement was investigated under diesel engine-like conditions. The results show that the variation of local heat flux characteristics was caused by spray flame velocity and temperature distribution. The main conclusions are summarized as follows.

1. Convection by turbulence has a significant effect on resulted heat flux values. Spray impingement to the wall was delayed at lower injection pressures, thus, injection pressure, 80 MPa, had the minimum heat flux value. Whereas impingement was realized at faster rates

with higher injection pressures due to earlier turbulent convection effect, which is reason for the higher heat flux values.

2. Convection by spray motion contributes to the total transferred heat through the impingement wall as does the higher injection pressure. The portion which was attributed to spray motion reached around 30 % at injection pressure 180 MPa.
3. Local heat transfer coefficients were calculated by using measured heat flux and temperature in both combustion and non-combustion conditions. The results showed that both combustion and non-combustion conditions had similar waveforms of heat transfer coefficient at all the positions. This largely determines that induced flow by the spray is dominant for the heat transfer to the wall in combustion case.
4. Injection pressure increases was proportional with that the rate of heat transfer both non-combustion and combustion conditions. Higher spray flame velocity by high injection pressure was the main factor in these losses than flame distribution and resident time during flame contact area.
5. A larger nozzle hole diameter has a significant effect on the peak value of local heat flux, which was caused by the its high of velocity and momentum. However, it was decreased on total heat flux and transferred heat due to flame temperature distribution was not as wide as the smaller nozzle hole diameter.
6. Regarding with the effect of injection pressure and nozzle hole diameter on the wall heat loss, the larger nozzle hole diameter, the less heat loss was generated at injection pressure of 80 and 120 MPa. Flame temperature was influencing factor on heat loss under these conditions. in contrast, the larger nozzle hole diameter caused more heat loss at injection pressure of 180 MPa. Local high-temperature end gas regions had dominant effect on heat loss at this injection pressure/nozzle hole diameter condition.

CHAPTER 6

EFFECT OF OXYGEN CONCENTRATION ON HEAT TRANSFER

6.1 INTRODUCTION

In modern diesel engine, the fuel-air mixture become important factor on the combustion process and exhaust emissions, and then in thermal efficiency. In order to reduce the emission, exhaust gas recirculation (EGR) is effective equipment part to reduce nitrogen oxides (N_{Ox}) from diesel engines because it lowers the flame temperature and the oxygen concentration of the working fluid in the combustion chamber [114]. With increasing EGR rate, the oxygen concentration in the fuel/gas mixture decreases and the specific heat of the cylinder increases and leads reaction rate decrease. Further, in-cylinder pressure and combustion decrease [43]. As described by the previous researchers in literature review, oxygen concentration has an effect on combustion behavior, which closely relates with lower temperature combustion. Therefore, to clarify an effect of oxygen concentration on decreasing heat loss, variation of oxygen concentration will be investigated in this study.

6.2 EXPERIMENTAL CONDITIONS

Injector including injection condition and experimental measurement conditions are listed in Table 6.1 and 6.2. Injection quantity was 5 mm^3 with injection pressure 120 MPa using a nozzle of 0.133 mm hole diameter. The impinging distance between the nozzle tip to the impingement wall was set at 40 mm. Oxygen concentrations were conducted at 21 and 16% as experimental parameters to investigate the effect of the heat transfer characteristics on the impinging flame on the wall.

Table 6.1 Injector and Injection Conditions

Injector type	Piezo actuator type
Number of nozzle holes	1
Injection quantity (mm^3)	5
Diameter of nozzle holes (mm)	0.133
Injection pressure (MPa)	120

Table 6.2 Experimental and Impingement Wall Conditions

Ambient condition	Combustion
Ambient gas	O ₂ = 21 % O ₂ = 16 %
Ambient pressure (MPa)	4.1
Ambient temperature (K)	873
Ambient density (kg/m ³)	16
Fuel	Diesel Fuel
Impingement wall	Flat plate, Stainless steel
Impingement distance (mm)	40
Wall temperature (K)	460 ± 10
Cooling method	Oil cooling

6.3 COMBUSTION FLAME BEHAVIOR

In this section, impinging flame behavior under oxygen concentration are studied. Effects of the oxygen concentrations (O₂), which were 21% were investigated at impingement distance of 40 mm. Figure 6.1 shows images of impinging flame natural luminosity at different oxygen concentrations. In this condition, non-evaporation and evaporation non-combustion has explained in the previous section.

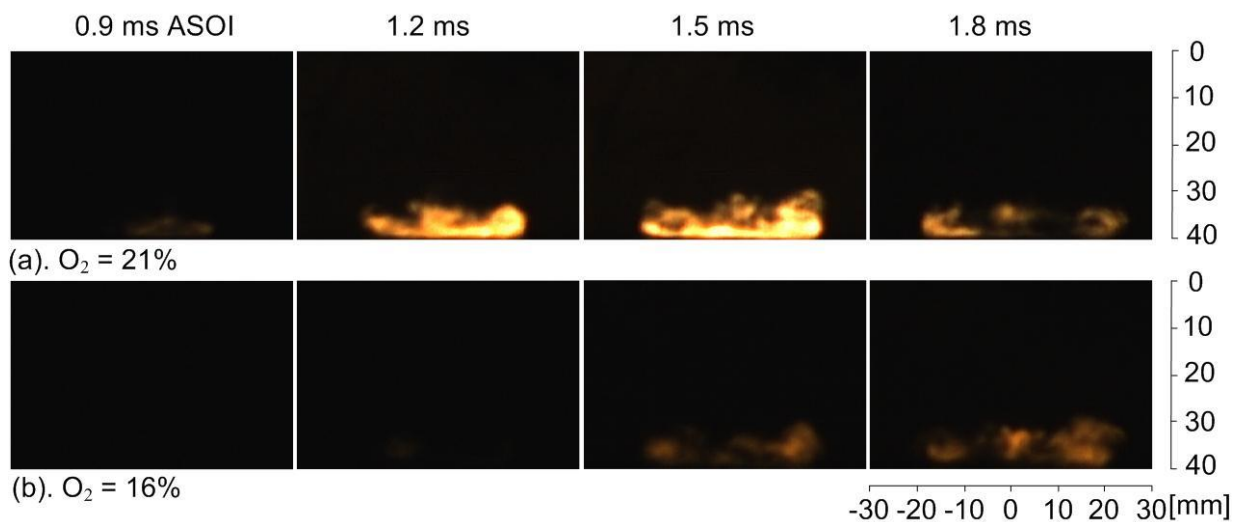


Figure 6.1 High-speed video camera images of impinging flame at different oxygen concentration

In the Figure 6.1, the luminous flame appeared earlier with $O_2 = 21\%$. It had started at 0.9 ms ASOI before the end of injection (EOI) and at 1.25 ms ASOI just after the EOI for $O_2 = 16\%$. It is found that the reduction of the oxygen concentration in the enclosure mainly affects the reactions in the gas phase and results in changes of the combustion behavior such as ignition timing and flame development. It can be seen at 1.5 to 1.8 ms ASOI, flame natural luminosity start to be decreased at $O_2 = 21\%$. However, it starts to develop at $O_2 = 16\%$ due to ignition delay was decrease. Consideration the intensity of luminous flame, they were surprisingly different each other. As shown in the figure, lower oxygen concentration generated lower luminous and flame develops quite slowly. Oxygen concentration is therefore required to complete the combustion process since the ignition was not possible occurred without any oxygen.

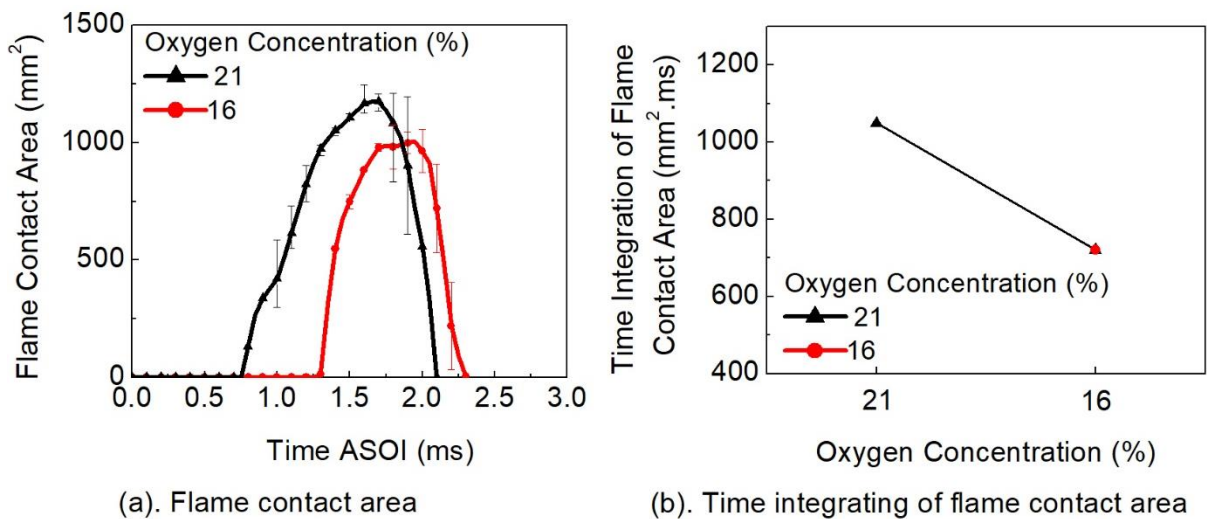


Figure 6.2 Comparison of flame contact area and time integrating of flame contact area at different oxygen concentration

Effect of flame contact to the wall at different oxygen concentrations are presented in Figure 6.2. Figure 6.2 (a) shows that $O_2 = 16\%$ had smaller contact area than that $O_2 = 21\%$. It means with oxygen concentration of 21%, leads to flame contact significantly to spread wide into circumferential area of flat wall. This flame contact area contributes to the heat transfer by conduction. The larger flame contact area causes larger area to be affected to rate of heat

transfer. Time integration of the flame contact area can be seen in Figure 6.2 (b), which shows that flame traveling distance was shorter as the oxygen concentration is decreased.

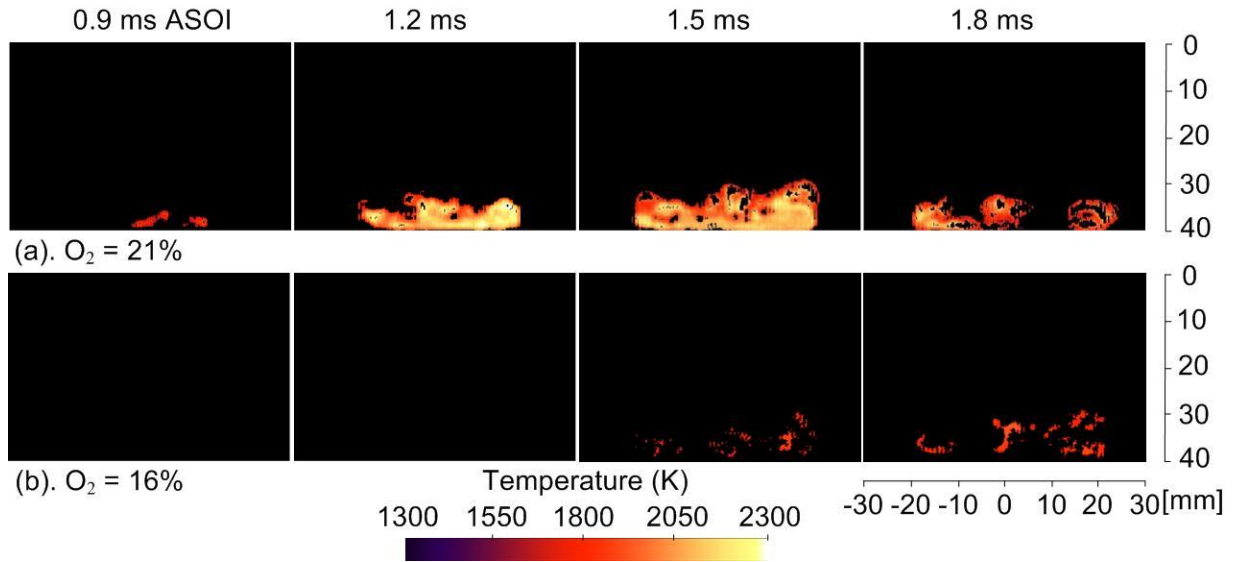


Figure 6.3 Flame temperature distribution at different oxygen concentration

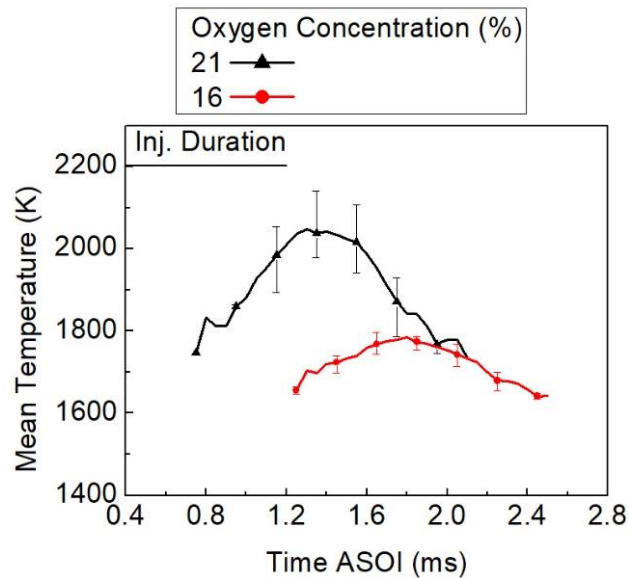


Figure 6.4 Mean temperature at different oxygen concentration

Figure 6.3 shows flame temperature distributions at different oxygen concentrations obtained from two-color method analysis, which was performed with flame natural luminosity images. By comparing the temperature distributions with different oxygen concentrations, it

can be seen that the temperature distribution was decreased by decreasing oxygen concentration. It can be inferred from Figure 6.4 that burned gas temperature decreases with decreasing volume fraction of oxygen because the heat capacity of ambient gas increase with decreasing the volume oxygen concentration [23]. When the combustion temperature was low, the temperature difference between the flame and the wall surface were decreased. So that it will have an impact on the reduced energy lost to the wall. Furthermore, soot emission during combustion process also decreased at low temperature as can be seen that the luminous flame significantly decreased. At $O_2 = 16\%$, the maximum temperature was 1785 K, around 400 K decreased from the peak value of $O_2 = 21\%$.

6.4 HEAT FLUX ON THE WALL SURFACE

Non-steady local heat fluxes with flame impinging on the wall and integrated luminosity from flame images at different oxygen concentrations are presented in Figure 6.5 (a-b). The figure shows a significant difference in the ignition timing both conditions. The low temperature due to decreasing oxygen concentration causes unsuitable equivalence ratio for ignition. As a result, local heat flux at Position 1 and 2 started to increase earlier before the ignition occurred. The most surprising is the peak value of local heat flux was dramatically decreased when the ignition occurred later after spray impingement. It is because the both positions increased mainly by convective evaporation spray during the injection duration. Consequently, the rate of heat transfer was lower around area Position1 and 2. However, in case of $O_2 = 21\%$, the ignition occurred just after impingement in which cover Position1 and 2, as a result Position2 increased simultaneously with ignition and gave substantial amount on local heat flux in that region. The temperature distribution also playing role on this phenomenon.

Even though, local heat flux increase and higher peak value was observed at Position1 and 2 under $O_2 = 21\%$. However, there was no significant difference in Position3 at both conditions. The wall friction and momentum loss due to turbulent mixing took place at Position3 as the far area from the center of impingement.

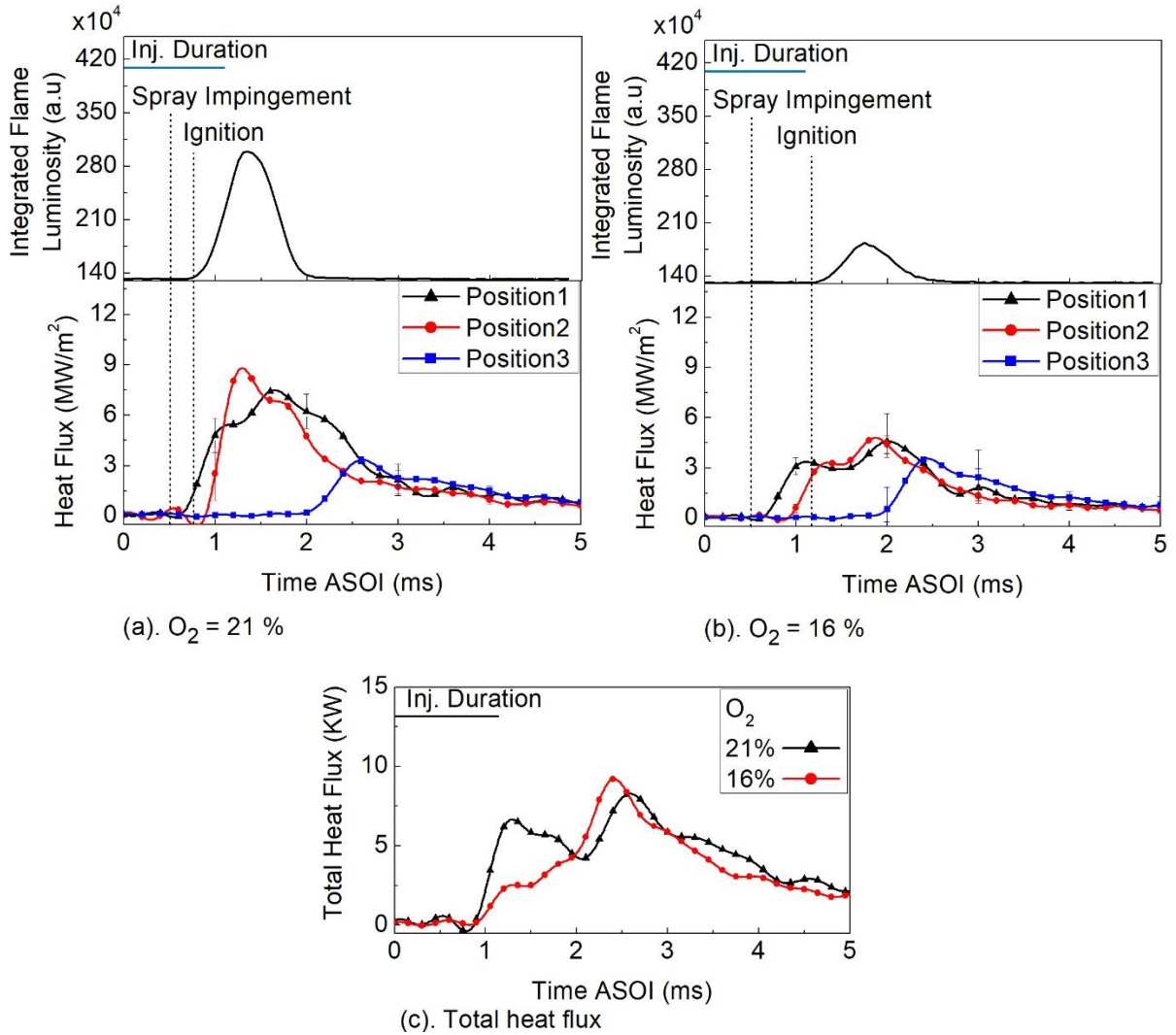


Figure 6.5 Temporal variation of local heat flux, integrated flame luminosity, and total heat flux at combustion

Figure 6.5 (c) shows temporal variation of the total heat flux at different oxygen concentrations. It can be seen in the graph, O₂ of 21% had two peaks waves i.e. there were two stages for the local heat transfer. At first, the local heat flux was increased by turbulence of impingement spray. Then, heat transfer by flow along the wall, which started after impingement, took place. While O₂ of 16% accumulated at the second stage for local heat transfer due to significant ignition delay. Consequently, the temperature distribution was appeared far away from the center of impingement in which influence on larger area.

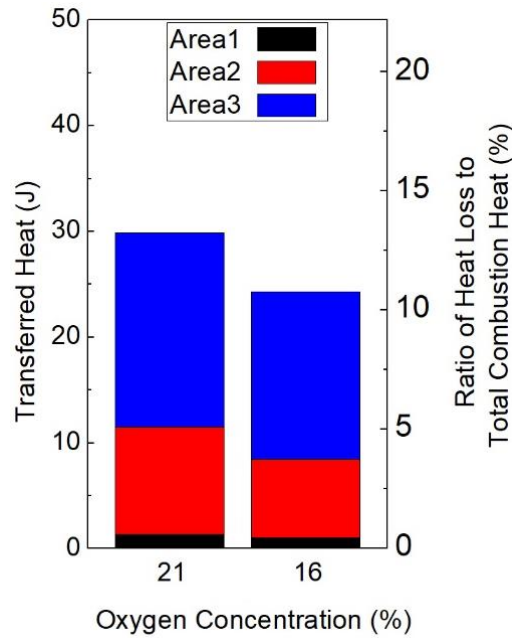


Figure 6.6 Comparison of the areal transferred heat and ratio of heat loss to total combustion heat at different oxygen concentration

A comparison of the transferred heat at each area under different oxygen concentrations are shown in Figure 6.6. Transferred heat value was decreased with lower oxygen concentration. This effect is mainly due to the decrease in the burned gas temperature with decreasing the volume fraction of oxygen concentration [23]. Regarding this graph, the transferred heat at $O_2 = 16\%$ decreased around 18% from $O_2 = 21\%$. This decrease was observed at all areas. Decreasing oxygen concentration was effective parameter for reducing the heat transfer on the wall. Ratios of heat lost through the wall to total combustion heat are also shown in the graph. It is about 11% of total combustion energy at lower oxygen concentration.

6.5 SUMMARY

This chapter has explained the effects of oxygen concentration on the combustion wall heat transfer under diesel engine-like conditions. The following conclusions can be deduced as follows.

1. By using the two-color pyrometry analysis, we found that the combustion distribution was low temperature at oxygen concentration of 16%.

2. The low temperature due to decreasing oxygen concentration delays start of ignition. As a result, total heat flux accumulated at the peak of second waveform stage.
3. Comparing different oxygen concentration, O₂ of 16% showed the lower transferred heat to the wall. This was caused by decrease in burned gas temperature and small flame contact area.
4. At O₂ = 16% condition, transferred heat to the wall was reduced around 18%. It means around 11% of heat was lost from total combustion energy.

CHAPTER 7

COMBINED EFFECT OF IMPINGEMENT DISTANCE/INJECTION PRESSURE AND OXYGEN CONCENTRATION/INJECTION PRESSURE

7.1 INTRODUCTION

In the previous chapter, the mechanism of wall heat transfer with impinging spray/flame on the wall have studied with various effects parameter in order to improving the thermal efficiency. In this chapter, further study was conducted with combined effect of impingement distance/injection pressure and oxygen concentration/injection pressure. Furthermore, in this study, relation between Nusselt number (Nu) and Reynolds number (Re) were also investigated to understand the heat transfer phenomena in diesel engines. For the characteristic velocity, mean piston speed is usually used in the previously proposed heat transfer equation. Recently, Kuboyama, et al. [23] used spray tip velocity as characteristic velocity during the fuel injected period. In this study, to obtain characteristics velocity for Re number, flamelet velocity as a new method for determining characteristics velocity will be discussed in detail. The aim of this study is to gain a full understanding of the heat loss phenomenon at some combined effects as a parameter condition.

7.2 EXPERIMENTAL CONDITIONS

Table 7.1 demonstrates the injector and injection conditions that will be used in the combined effect. The injection pressures were set 80, 120, and 180 MPa. Under the combined effect of impingement distance/injection pressure, the experimental and impingement wall con-

Table 7.1 Injector and Injection Conditions

Injector type	Piezo actuator type
Number of nozzle holes	1
Injection quantity (mm ³)	5
Diameter of nozzle holes (mm)	0.133
Injection pressure (MPa)	80, 120, 180

Table 7.2 Experimental and Impingement Wall Conditions under Combined Effect of Impingement Distance/Injection Pressure

Ambient condition	Non-Evaporation	Evaporation and Combustion
Ambient gas	N ₂	Combustion: Air (N ₂ :79%,O ₂ :21%) Evaporation: N ₂
Ambient pressure (MPa)	1.4	4.1
Ambient temperature (K)	300	873
Ambient density (kg/m ³)	16	←
Fuel	Diesel Fuel	←
Impingement wall	Flat plate, Stainless steel	←
Impingement distance “D _{imp} ” (mm)	30, 40, 50	←
Wall temperature (K)	300	460 ±10
Cooling method	-	Oil cooling

Table 7.3 Experimental and Impingement Wall Conditions under Combined Effect of Oxygen concentration/Injection Pressure

Ambient condition	Combustion
Ambient gas	O ₂ = 21 % O ₂ = 16 %
Ambient pressure (MPa)	4.1
Ambient temperature (K)	873
Ambient density (kg/m ³)	16
Fuel	Diesel Fuel
Impingement wall	Flat plate, Stainless steel
Impingement distance (mm)	40
Wall temperature (K)	460 ±10
Cooling method	Oil cooling

ditions are presented in Table 7.2. Distance from nozzle tip to wall was used 30, 40, and 50 mm as various of impingement distances. The conditions at non-evaporation, evaporation and combustion also presented in the table. Table 7.3 shows the experimental conditions and wall condition under the combined effect of oxygen concentration/injection pressure. The oxygen concentration was selected as 21 and 16% at impingement distance of 40 mm. The nozzle hole diameter was set at 0.133 mm regardless of injection pressure, impingement distance, and oxygen concentration.

7.3 COMBINED EFFECT OF IMPINGEMENT DISTANCE /INJECTION PRESSURE ON WALL HEAT TRANSFER

In this section, combined effects of the impingement distance and injection pressure on heat transfer were investigated. Figure 7.1 shows the combined effect of impingement distance/injection pressure on the transferred heat and ratio to the total combustion heat. Three injection pressures, i.e. 80, 120, and 180 MPa were investigated at each impingement distance of 30, 40, and 50 mm. The combined effect can be explained as follows:

1. The transferred heat significantly increased at injection pressure of 180 MPa. Especially combining with longer impingement distance, it dramatically increased.
2. On the other, there were small differences in them except 180 MPa by the distances.
3. The ratio of heat loss through the wall accounts for about 10-17 % of total combustion energy.

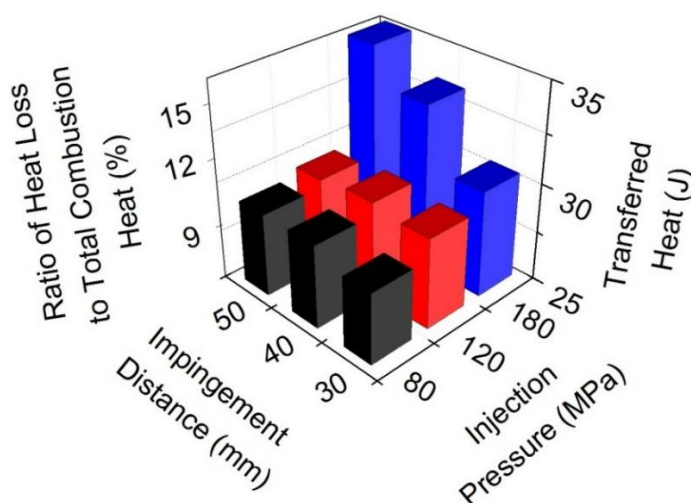


Figure 7.1 Comparison of the areal transferred heat at combined impingement distance/injection pressure

The heat loss phenomenon under the combined effect of impingement distance/injection pressure, D_{imp}/P_{inj} conditions may be related to the liquid spray impingement on the wall. Figure 7.2 presents the evaporating wall impinging spray at combined D_{imp}/P_{inj} under the same injected fuel quantity, which was taken just before the end of injection (EOI) each. Figure 7.2 (a) shows liquid fuel adhered in all the pressure conditions due to small impingement distance. In general, liquid film on a wall surface tended to decrease with increased injection pressure [115], because the impinged spray spreads to wider area and distribution of the spray is more uniform as the

injection pressure rises. However, these photographs look similar in all injection pressures due to the same amount of injected fuel. This means that the transferred heat decrease at the distance of 30 mm under injection pressures in Figure 7.1 was influenced by liquid fuel adhered on the wall. Moreover, Figure 7.2 (a-c) at 180 MPa injection pressure shows the short impingement distance could not avoid liquid impingement on the wall. Consequently, the lower wall temperature due to liquid impingement then influences combustion temperature in the near wall region which led to the decelerating wall heat transfer.

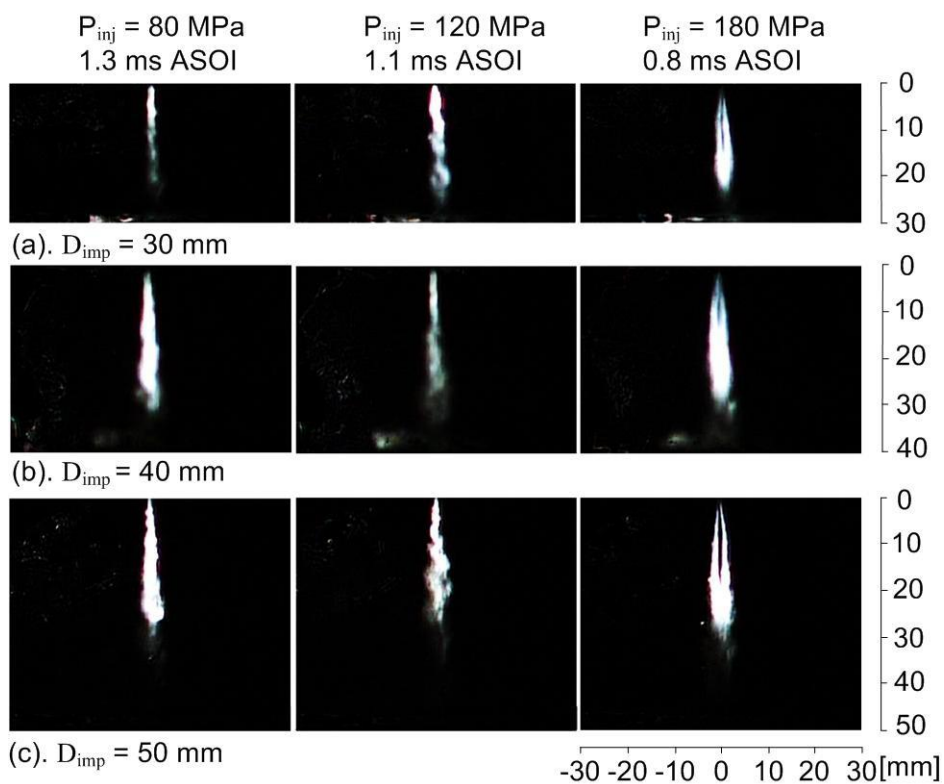
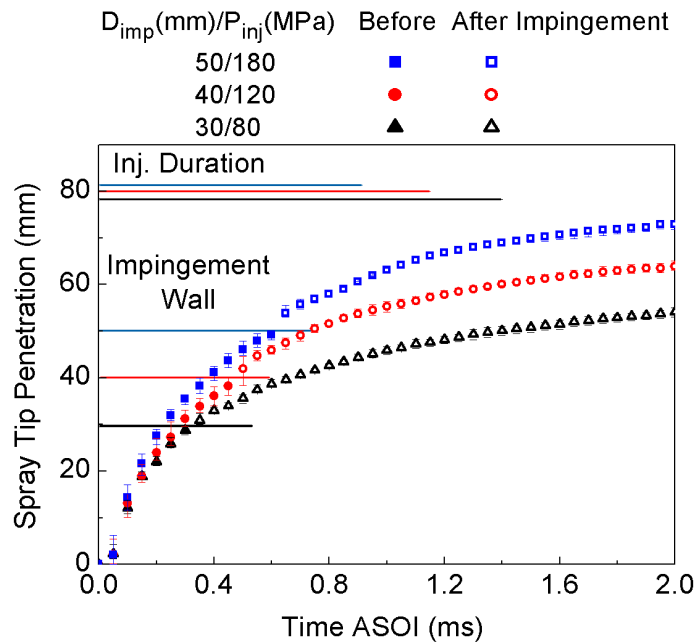


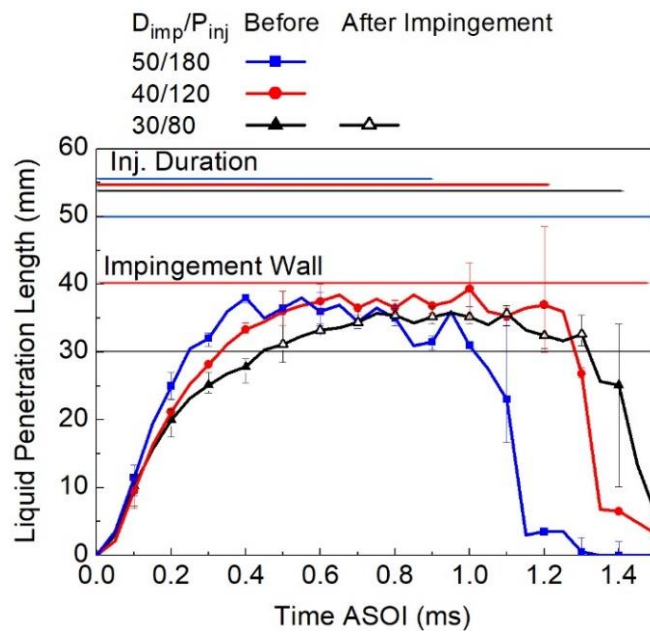
Figure 7.2 Evaporating wall impinging spray (liquid component) at combined impingement distance/injection pressure under same amount injected fuel quantity

As the transferred heat was increased by combination of the longer distance with the higher pressure we studied with the following combination, i.e. Impingement distance/injection pressure, $D_{imp}/P_{inj} = 30/80, 40/120$ and $50/180$ (mm/MPa), respectively. The nozzle hole diameter was set at 0.133 mm regardless of injection pressure and impingement distance conditions.

7.3.1 Combined Effect of Impingement Distance and Injection Pressure under Non-combustion



(a). Non-evaporation condition



(b). Evaporation non-combustion condition

Figure 7.3 Non-evaporating spray tip penetrations and evaporating liquid penetration length at combined impingement distance/injection pressure.

Non-evaporating spray tip penetrations and evaporating liquid penetration length under combined impingement distance/injection pressure are presented in Figure 7.3 (a). After fuel being injected, momentum exchange between the liquid and surrounding gas lead to deceleration of the droplets [116]. The spray tip experiences the strongest deceleration and the droplets with low kinetic energy are pushed aside. This forms more diluted spray downstream the nozzle, while liquid fuel mass is concentrated near the spray axis [117]. Combination of $D_{imp}/P_{inj} = 50/180$ reached a maximum spray tip penetration as shown in Figure 7.3 (a). In the case of high injection pressure, thus, high injection velocity, the droplets at the spray tip are continuously replaced with new ones, and the spray penetration increases further [117].

Combined effect of injection pressure and impingement distance on evaporating spray tip penetrations can be seen in Figure 7.3 (b). In the case of $D_{imp}/P_{inj} = 30/80$ liquid spray length still exists at time of impingement, while 120/40 hardly ever contact with impingement wall in liquid phase. A further increase in injection pressure, 180 MPa, liquid fuel was completely vaporized before reaching impingement distance, 50 mm.

7.3.2 Combined Effect of Impingement Distance and Injection Pressure under Combustion Condition

Figure 7.4 (a-c) shows flame temperature distribution at combined impingement distance/injection pressure. The flame temperature distribution will be greatly different from that combined effect. Spray mixture during ignition delay is the main factor in combustion develop including its flame temperature. The occurrence of a very bright intensity after auto-ignition is considered as flame temperature. As impingement distance shorter and injection pressure lower, temperature distribution become wider. The large flame growth is without any doubt due to by effect of local high equivalence ratio, as this combination could not avoid fuel film around the wall impingement as shown in Figure 7.2 and 7.3 (b). However, in longer impingement distance and high injection pressure, $D_{imp}/P_{inj} = 50/180$ lead more air entrainment with improving in spray atomization and premixing between fuel and air due to high velocity. As a result, flame luminosity was reduced at Figure 7.4 (c). Due to weak intensity of the flame luminosity image, when it applying to the two-color method, the flame temperature also reduces.

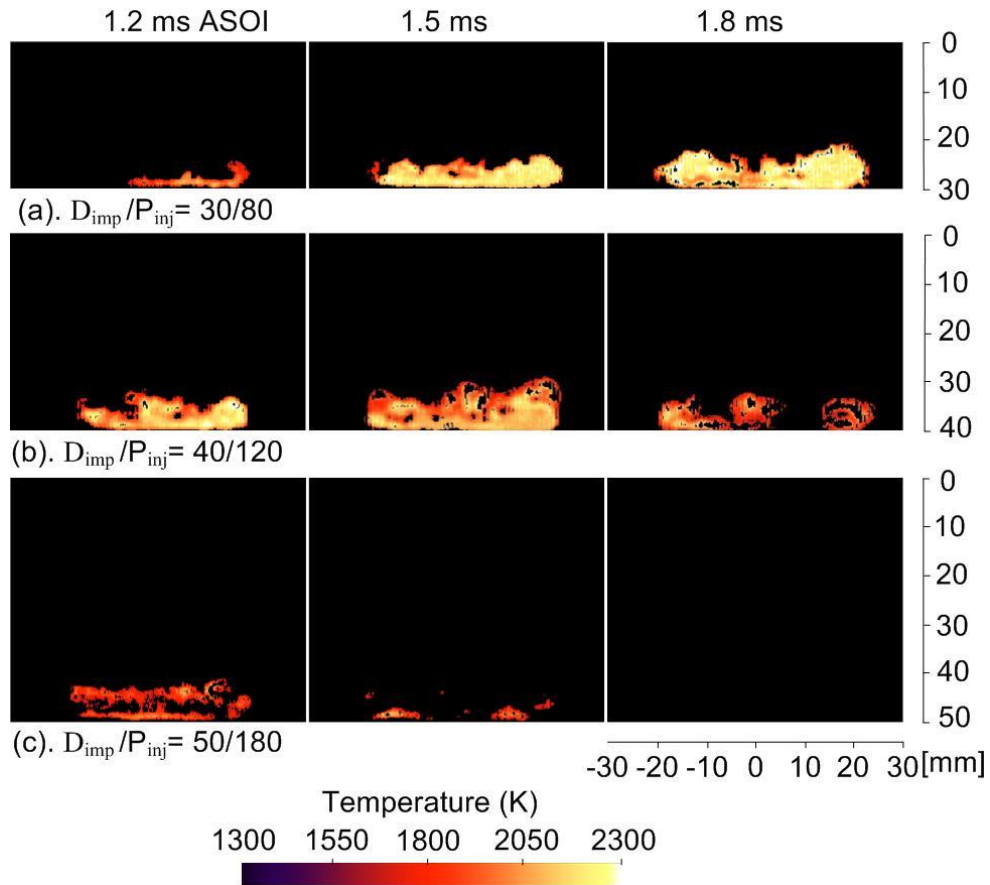


Figure 7.4 Flame temperature distribution at combined impingement distance/injection pressure.

7.3.3 Combined Effect of Impingement Distance and Injection Pressure on Wall Heat Transfer

As to the combined effect, the transferred heat was increased by combination of the longer distance with the higher pressure, in this subsection will be studied with the following combination, i.e. 30/80, 40/120 and 50/180, respectively. Figure 7.4 (a-c) shows temporal changes of non-steady local heat flux and integrated luminosity with the combination of D_{imp}/P_{inj} conditions. The combination showed far lower integrated flame luminosity at higher injection pressure than that of lower injection pressure. This means more complete combustion with sufficient oxygen was achieved.

By comparing the combination of 30/80, 40/120, and 50/180 as shown in the Figure 7.4 (a-c), combination of 50/180 showed that the heat fluxes rose more steeply and higher. Moreover, start points of the steep rise at Position1 and 2 became simultaneous with the combination. This was probably the convection by turbulence from spray impinging, which

took time to reach the wall due to longer impingement distance. As a result, it reached to the wall simultaneously with the ignition which had a major impact on the local heat flux values. At the same times, due to high injection pressure related to high velocity, the flame gas flow of outer area became faster and led to the higher local heat flux waveform at position3 comparing with the other combination.

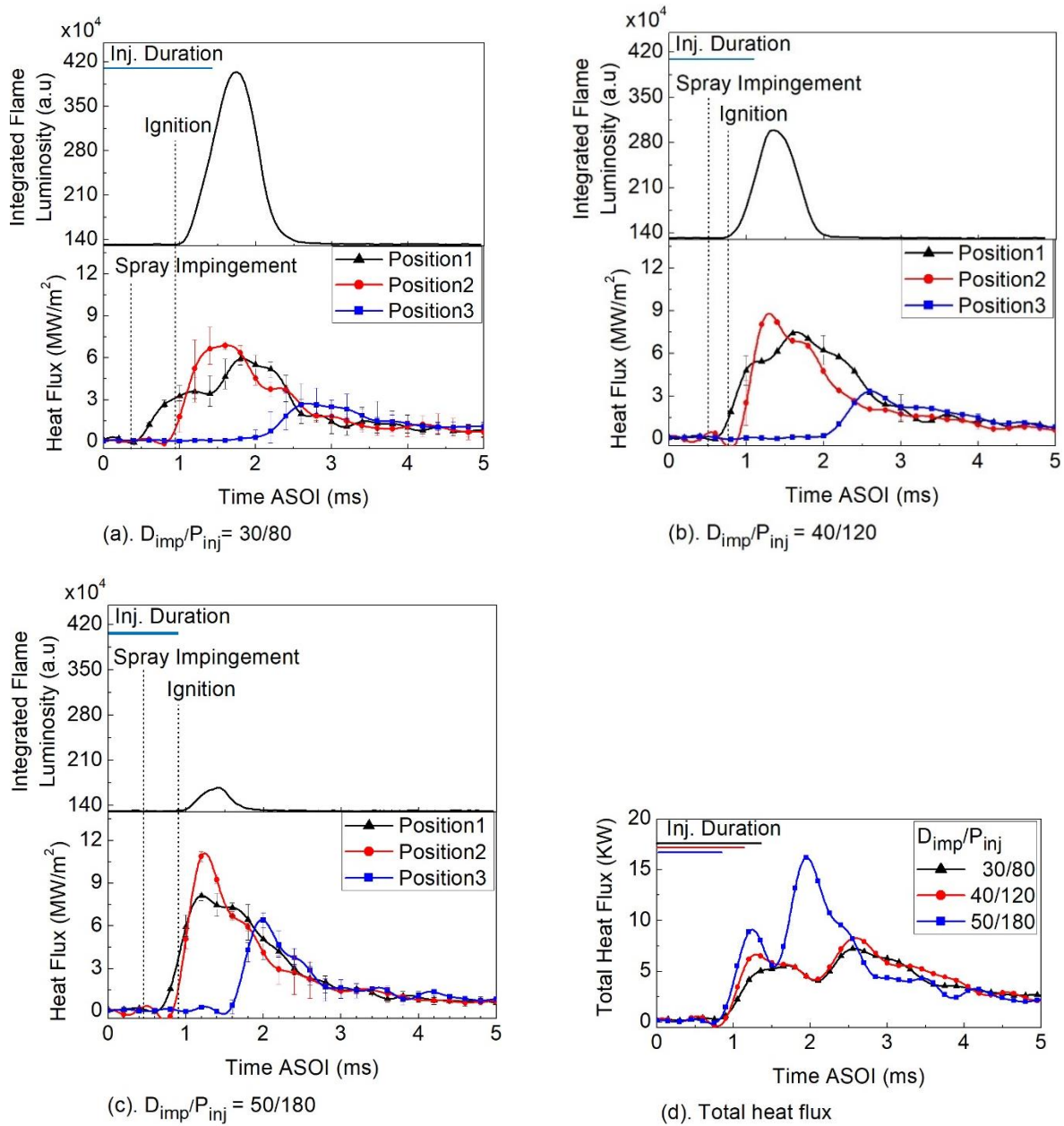


Figure 7.4 Temporal variation of local heat flux, integrated flame luminosity, and total heat flux at combined impingement distance/injection pressure

On the other hand, combination of 30/80 had a lower local heat flux due to a large liquid spray impingement to the wall. It could be explained with Figure 7.3 (b) that liquid component of the spray reached to the wall only at impingement distance of 30 mm. It was plausible that cooling effect from liquid fuel adhered on the wall could have influenced to the slow heat transfer rate. Besides, liquid fuel adhered on the wall caused the local heat flux waveform at Position1 had slope after increasing. For reducing heat loss through the wall, liquid spray impingement was effective.

Figure 7.4 (d) shows total local heat flux at combination effect. The result showed that a maximum total heat flux value of 16.2, 8.3, and 7.2 kW for combined effect of 50/180, 40/120, and 30/80. According to the combined effect, it can be concluded that the high injection pressure more influential to total heat flux at longer impingement distance.

7.4 COMBINED EFFECT OF IMPINGEMENT OXYGEN CONCENTRATION/INJECTION PRESSURE ON WALL HEAT TRANSFER

In this subsection, combined effects of the oxygen concentration and injection pressure on wall heat transfer were investigated. Figure 7.5 presents the combined effect of oxygen concentration/injection pressure on the transferred heat and ratio to the total combustion heat. 21 and 16% as the various oxygen concentration were investigated at each injection pressure of

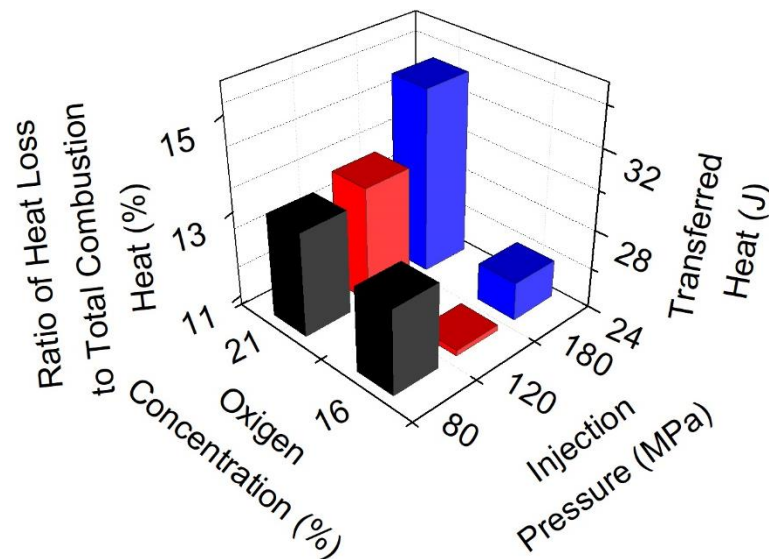


Figure 7.5 Comparison of the areal transferred heat at combined oxygen concentration/injection pressure

80, 120, and 180 MPa. The combined effect can be explained as follows:

Firstly, the heat transferred increased gradually with increasing injection pressure at $O_2 = 21\%$. However, it was not applied to $O_2 = 16\%$, the heat transferred increased disproportionately even though the injection pressure was increased. It means high velocity by increasing injection pressure was not dominant factor on transferred heat when oxygen concentration under 21%.

Secondly, lower oxygen concentrations consistently reduce heat transfer on the wall in all conditions. This decreased due to the flame temperature was lower. By higher oxygen concentration as 21%, it allows more stable combustion with produce high flame temperature then can lead more rate of heat transfer. And thirdly, the ratio of heat loss through the wall accounts for about 10-15% of total combustion energy.

Considering Figure 7.6, at lower oxygen concentration, the transferred heat decreased even though injection pressure was increase. It is inversely proportional when oxygen concentration was set $O_2 = 21$. Therefore, the studied will be focus on the following combination, i.e. $O_2/P_{inj} = 16/80, 16/180$ and $21/180$ (%/MPa) each. These conditions can represent both comparison different effect of injection pressures and oxygen concentration. Non-steady local heat flux and integrated luminosity with the combination of O_2/P_{inj} conditions are presented in Figure 7.6 (a-c).

Figure 7.6 (a-b) demonstrates the comparison of injection pressure in the combined effect. In the previous section, effect of injection pressure was explained in detail. However, since the oxygen concentration of 16% produced lower flame temperature, it is interesting to clarify the phenomenon in local heat flux history. By comparing the combination of 16/80 and 16/180 as shown in the Figure 7.6 (a-b), local heat flux waveform at all positions started to increase earlier at combination of 16/180. It is certainly due to increasing injection pressure related to increasing velocity. On the other hand, local heat flux peak value was almost similar in these combinations. Regarding this phenomenon, increasing injection pressure did not affect more on local heat flux at oxygen concentration of 16% due to both temperatures are lower. Even though spray mixture increases by higher injection pressure, the time of ignition was not change with pressure, but the combustion process was significant decreased in this condition.

At lower injection pressure, combustion duration is slightly longer which causes the flame contact was stayed longer on the wall. As a result, transferred heat to the wall increased as shown in Figure 7.5.

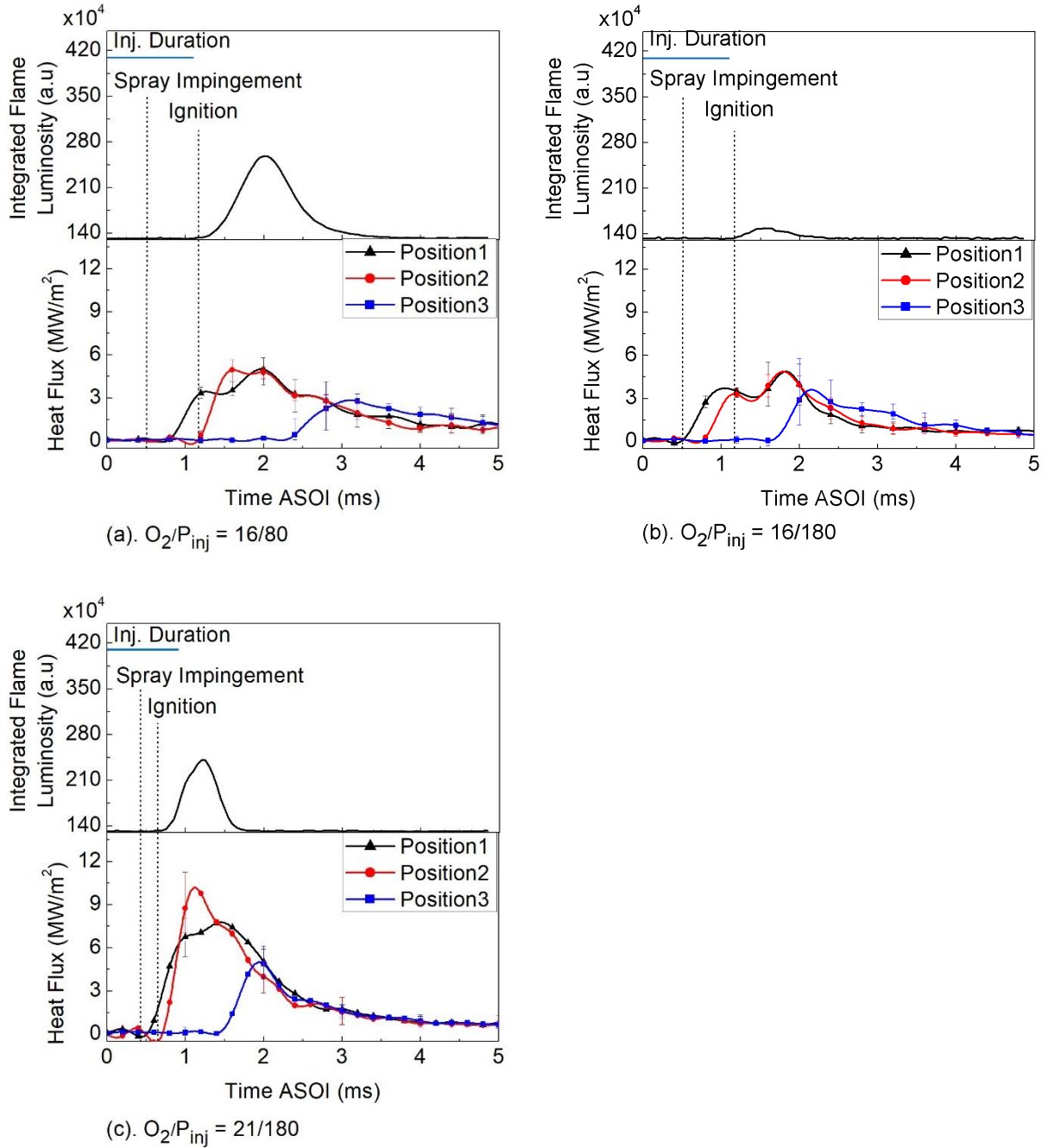


Figure 7.6 Temporal variation of local heat flux, integrated flame luminosity, and total heat flux at combined oxygen concentration/injection pressure

Figure 7.6 (b-c) shows a comparison of oxygen concentration in the combined effect. Combination of 21/180 had high local heat flux at all positions. with the increased oxygen concentration, increased both the fuel-air mixture and the reaction rate. As a result, the flame

temperature increased and this flame gas flow distributed along the wall due to high injection pressure, then lead the increase rate of the heat transfer. However, at lower oxygen concentration, the heat loss was decreased. It is due to the lower flame temperature and the reduced area contact period between the flame and the wall surface, caused by the higher heat capacity and density of the ambient gas [118].

7.5 HEAT TRANSFER CORRELATIONS

According to the above explanations, the spray flame flow has considerable effect on heat loss through the wall. Then, we studied relation between Reynold number (Re) and Nusselt Nu number.

7.5.1 Flamelet Velocity

As shown in equation (2.18), Re number requires characteristic flow velocity. Recently, Kuboyama, et al. [23] have provided alternative correlations which are applicable to recent diesel engines. They used flow induced by fuel injection during the fuel injection period for characteristic velocity. After the fuel injection, character velocity used in the Woshni's equation (piston speed). However, it was not possible to estimate the velocity by commonly used measurements, so we utilized waveforms of the heat flux as represented characteristics velocity. As characteristics velocity, mean piston speed is usually used in previously proposed heat transfer equations.

The waveforms had clear peaks which seemed to have resulted from combustion flame motion. If the peaks were similar in the different positions, by comparing peak by peak we could obtain flamelet velocities along the wall as will be explained in flamelet velocity. The characteristic velocity for the Reynolds number obtained from the single-shot heat flux waveform. In order to investigate characteristic flow velocity, flamelet velocity determined according to local combustion flame motion near wall which has direct impact on local heat flux waveform characteristic. It was assumed that the waveform which had clear peaks as a consequence of combustion flame motion.

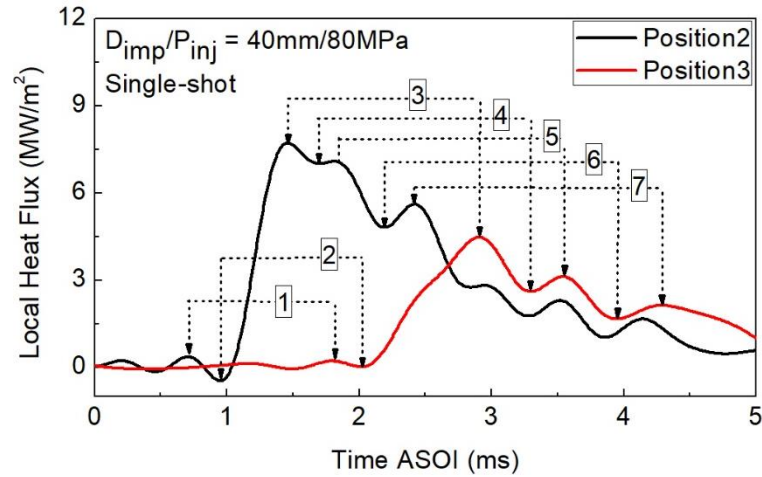


Figure 7.7 Relation of heat flux waveforms between the two points

Figure 7.7 presents single shot heat flux waveform in which only Position2 and 3 are displayed. The calculation method of flamelet velocity is as follows. First, the distance between Position2 and Position3 was 10 mm, denoted as characteristics length. Position2 and Position3 were chosen with consideration that Positions had a more stable velocity compared to that of Position1, at which it was in a state of stagnation. Next, time value can be detected from measuring the change in waveform between Position2 and Position3 as depicted by number 1 to 7 inside square as shown in Figure 7.7. According by the time difference between Position2 and Position3 (for example number 1), we obtained time value to calculate characteristic velocity. The Table 7.4 shows the result of flamelet velocity. From these results, it can be used for calculating *Re* number.

Table 7.4 Flamelet velocity result from heat flux waveform

Number	Times at Position (ms)		Distance from Position2 to Position3 (mm)	Velocity (m/s)
	P2	P3		
1	0.7	1.8	10	9.09
2	0.95	2.02	10	9.35
3	1.45	2.91	10	6.85
4	1.7	3.3	10	6.25
5	1.83	3.55	10	5.81
6	2.2	3.96	10	5.68
7	2.43	4.3	10	5.35

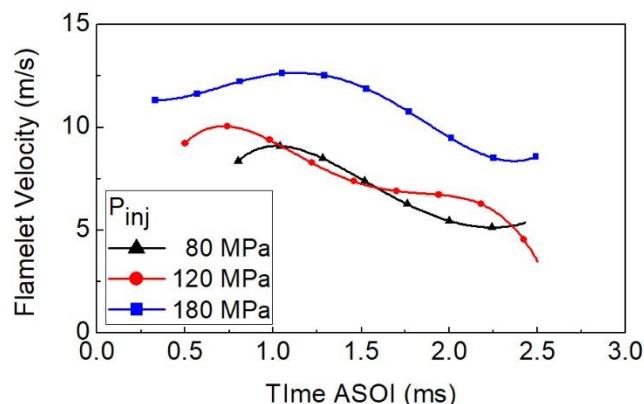


Figure 7.8 Flamelet velocity at different injection pressure

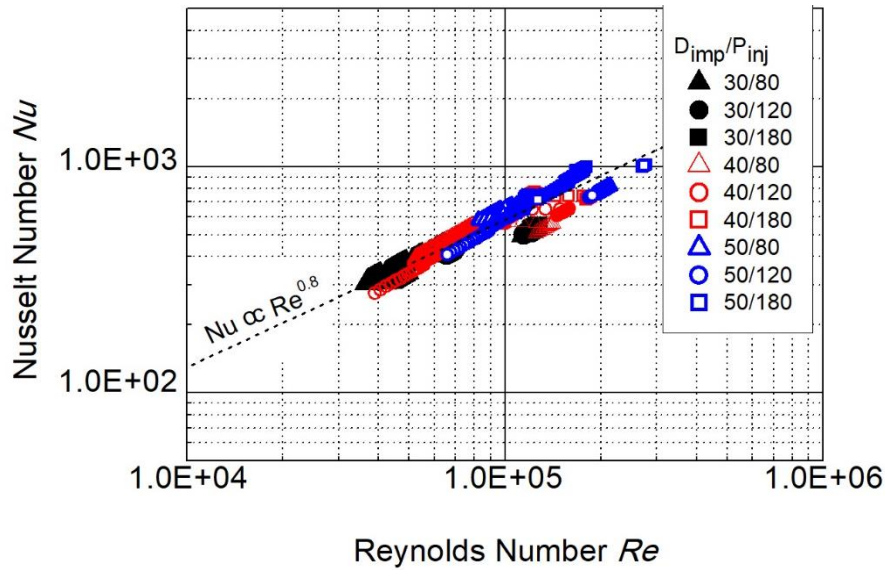
Figure 7.8 shows characteristic velocities at the different injection pressures by the method. 80 and 120 MPa showed similar velocity, while 180 MPa had higher velocity compared with others. This result seemed reasonable, as is reported by some researcher [26,27] at which the local flame velocity increased with high injection pressure. This increase is thought to be due to the increasing fuel injection velocity. Then we used these values for calculating Re number.

7.5.2 Correlation between Reynolds Number and Nusselt Number

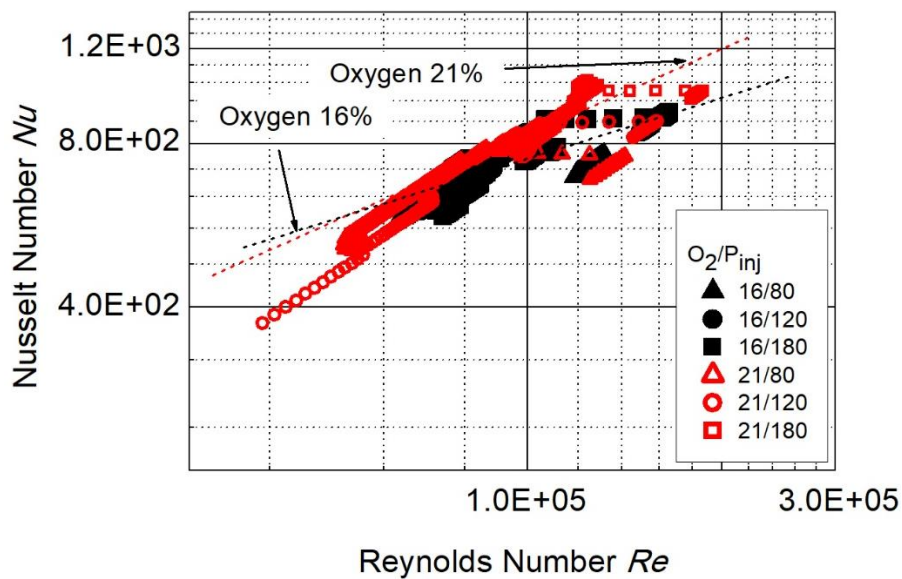
Figure 7.9 (a) shows correlation between Re and Nu number in all of Positions at difference of impingement distance and injection pressure. For Re number calculation, impingement distance is selected as a representative length, i.e. 40 mm, whereas those shown in Figure 7.8 were used for characteristic velocity. For Nu number calculation, thermodynamic properties of air were taken into account. It can be seen from the figure, relation between Nu number and Re number, approximates one line, regardless of the impingement distance and injection pressure conditions. It was found that Nu number was directly proportional to Re number of 0.8 powers for the combined case.

Figure 7.9 (b) performing a correlation between Re and Nu number at difference of oxygen concentrations and injection pressures. Once again, the figure showing the Nu number was proportional to Re number. High turbulence flow from combustion which is characterized by high Reynolds number is one of the major factors causing a large amount of heat transfer on

the wall. Regarding these results, using flamelet velocity to calculate Re number was well expressed in the correlation.



(a). Combined effect of impingement distance/injection pressure



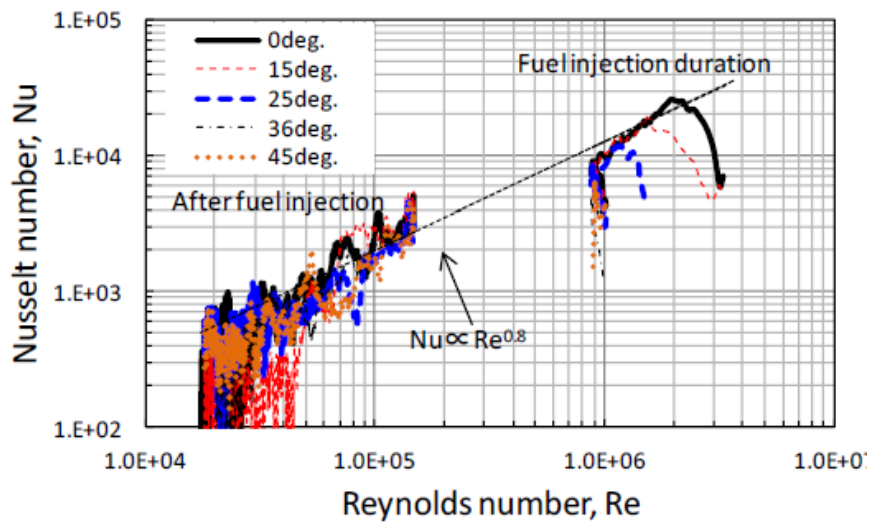
(b). Combined effect of oxygen concentration/injection pressure

Figure 7.9 Correlation between Reynolds number and Nusselt number at combined impingement distance/injection pressure and oxygen concentration/injection pressure.

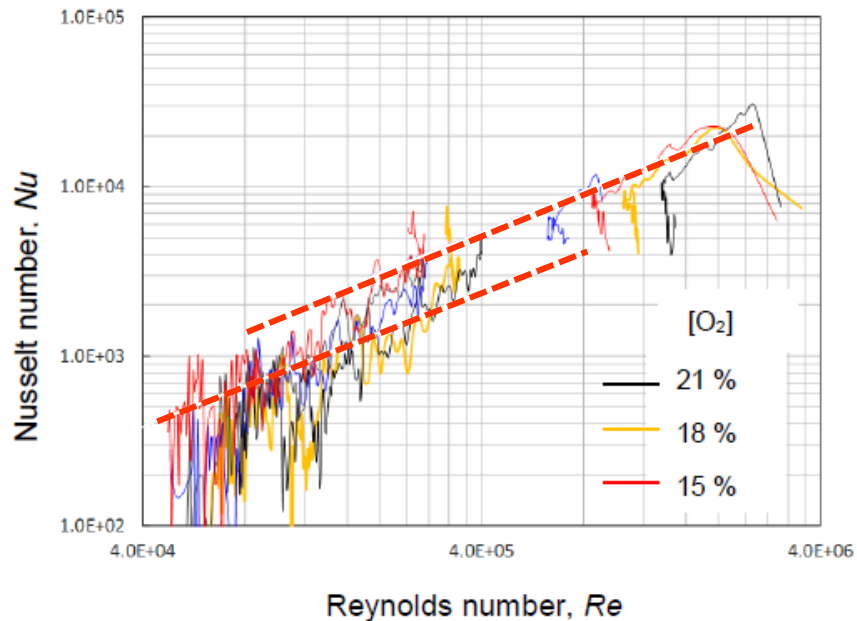
Differences in characteristics velocity for examples: Kuboyama et al.,[23] using flow induced by fuel injection and piston speed and Fujikawa et al.,[119] using flame tip velocity as shown in Figure 7.10, it can be compared as follows:

a. Nu number was directly proportional to Re number at all conditions.

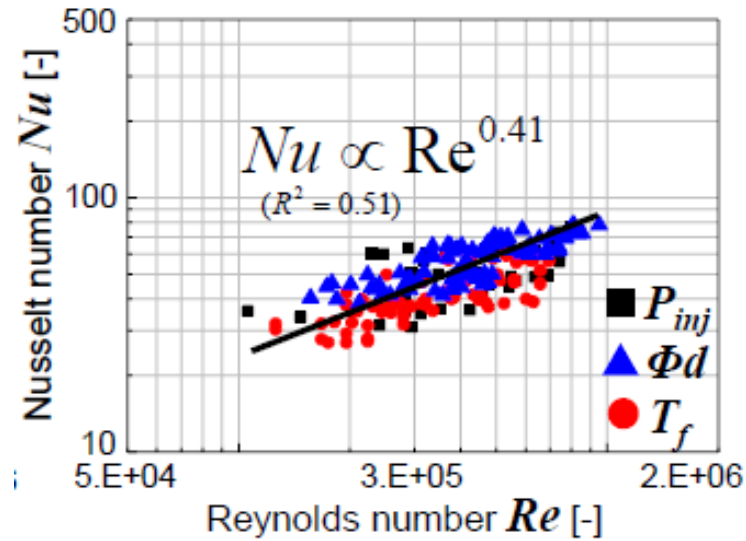
- b. As can be seen in the Figure 7.9, the value of Reynolds number was 0.8 powers at all combines case. It was similar with Kuboyama et al., in Figure 7.10 (a-b).
- c. Nusselt number value was slightly higher at Kuboyama et al., results. It is because the Kuboyama et al., using rapid compression expansion machine in which high turbulent flow occurred with high compression ratio.



(a). Effect of the different location measurements [23]



(b). Effect of the volume fraction of the oxygen [23]

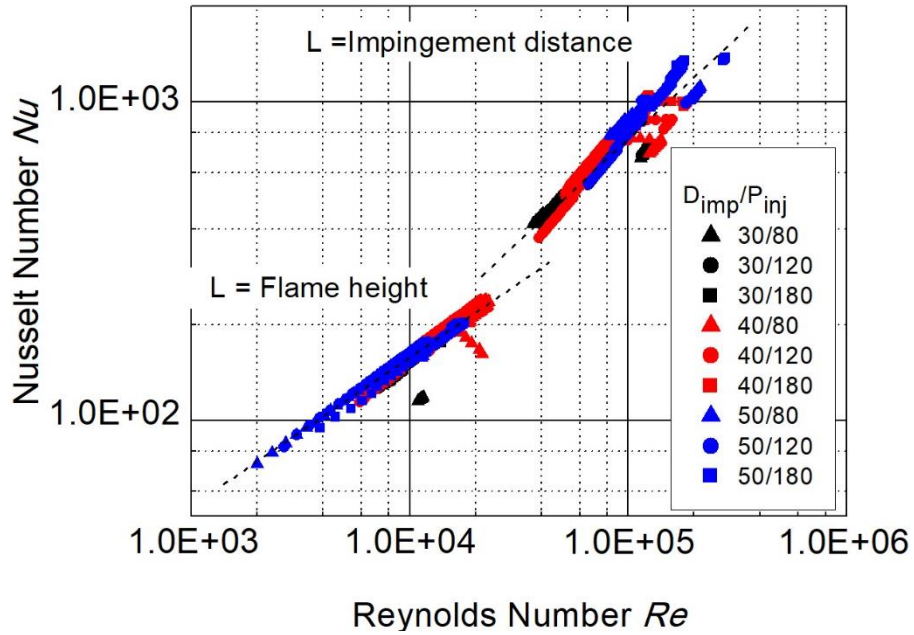


(c). Effect of the injection pressure, nozzle hole diameter, and fuel temperature [119]

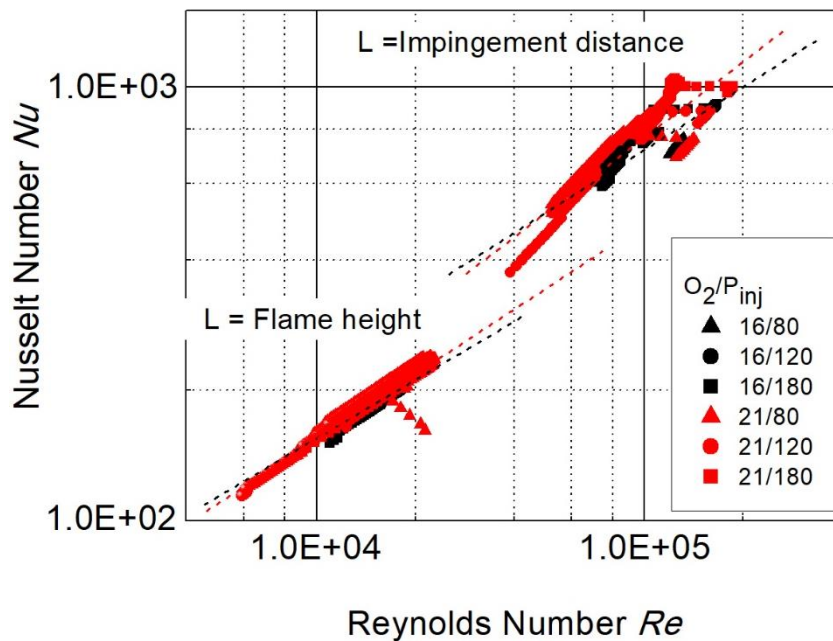
Figure 7.10 Relation between Reynolds number and Nusselt number at different location measurements and different oxygen concentrations [23]; and injection pressure, nozzle hole diameter, and fuel temperature [119]

- d. However, Nusselt number value was slightly lower at Fujikawa et al., due to different ambient density and characteristics height.
- e. Comparison heat transfer correlation with others researcher can be seen in appendix Figure 7 (a-b).

To more accurately predict the heat transfer correlation, then we modified the characteristics length from impingement distance to flame height as shown in Figure 7.10 (a-b). As a result, Nusselt and Reynold number value was lower by using flame high characteristics length at both combined effect of impingement distances/injection pressure and oxygen concentration/injection pressure.



(a). Combined effect of impingement distance/injection pressure



(b). Combined effect of oxygen concentration/injection pressure

Figure 7.10 Correlation between Reynolds number and Nusselt number at combined impingement distance/injection pressure and oxygen concentration/injection pressure using flame height as characteristics length.

7.6 SUMMARY OF ALL PARAMETER EFFECTS

In order to understand the heat loss at various of experimental parameters, Figure 7.11 shows relative change of the heat loss for experimental parameter corresponding to baseline

condition. From this graph, heat loss increased only under injection pressure of 180 MPa at both experimental parameter of injection pressure, P_{inj} and impingement distance, D_{imp} . Furthermore, it contributed heat loss around 17% when longer impingement distance and higher injection pressure. Nozzle hole diameter, D_{hole} is another experimental parameter that contributed heat loss on the wall. These D_{hole} generated heat loss at all of injection pressures. In contrast with what was D_{hole} resulted, oxygen concentration produced lower heat loss at all injection pressures. It was around 18% heat loss decreased at injection pressure 120 MPa. Temperature gradient is as the major source of transferred heat, when the flame temperature is weak, the result is slow heat transfer on the wall.

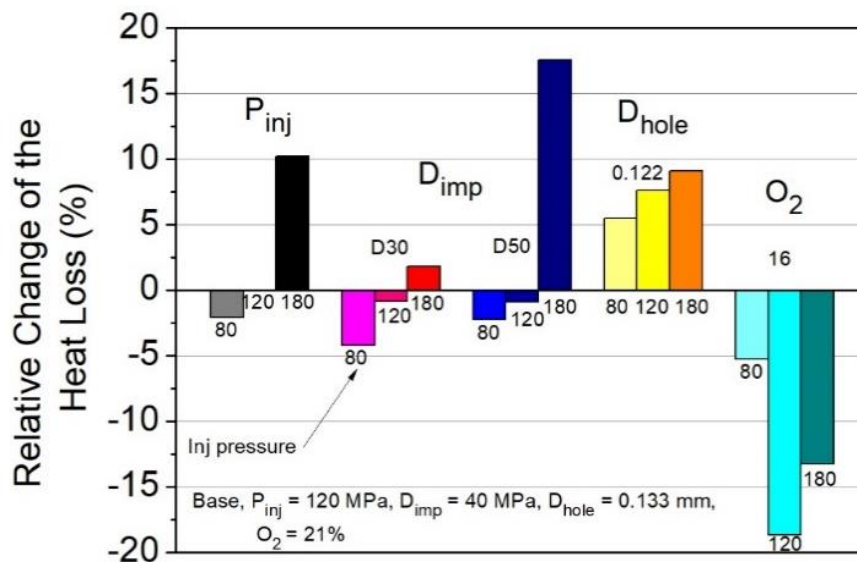


Figure 7.11 Relative change of the heat loss for experimental parameter.

7.7 SUMMARY

The combined effects of impingement distance/injection pressure and oxygen concentration/injection pressure on the combustion wall heat transfer under diesel engine-like conditions were investigated. Moreover, the correlation between Re and Nu number also was investigated in this study. From these results and discussions, conclusions this work are derived as follows.

1. The combined effect of injection pressure/impingement distance on the wall heat loss showed that heat loss was dramatically increased at injection pressure and impingement distance, 180/50 condition. Turbulent mixing effects before wall impingement played important role for this heat loss.
2. Regarding with the combined effect of oxygen concentration/injection pressure on the wall heat loss, the lower oxygen concentration, the less heat loss was generated at all injection pressures. Lower flame temperature and reduced flame contact area and period were influencing factor on heat loss under these conditions.
3. Under summary all of parameter effects (such as: Injection pressure, impingement distance, nozzle hole diameter and oxygen concentration), the decreasing oxygen concentration was effective to reduce heat loss on the wall.
4. The characteristics velocity in the heat transfer correlation under diesel engine-like conditions based on flamelet velocity in which was obtained from heat flux waveform. flamelet velocity determined according to local combustion flame motion near wall which has direct impact on local heat flux waveform characteristic.
5. A new method for determining characteristic velocity to calculate Re number has been proposed. By using the value, it was found that Nu number was proportional to Re number of 0.8 powers.

CHAPTER 8

CONCLUSIONS

The aim of this dissertation was understanding the mechanism of heat transfer from spray and flame to the impinging wall under small diesel engine-like conditions. The spray behavior under non-evaporation and evaporation scenarios were investigated using the Mie scattering technique. Moreover, the combustion behavior was investigated using direct imaging of the flame's natural luminosity. The distribution of the flame temperature and soot emission were quantitatively calculated by applying the two-color method on the natural luminosity images. The instantaneous temperature was detected via three thin-film thermocouple heat flux (TFTHF) sensors that had been mounted on the wall surface side. Unsteady heat flux at the impinging wall was calculated with the finite difference method using the measured temperatures as a boundary condition. The impingement distances (30, 40, and 50 mm), injection pressures (80, 120, and 180 MPa), nozzle hole diameters (0.133 and 0.122 mm), oxygen concentrations (21 and 16%), and combined effects (impingement distance/injection pressure, oxygen concentration/injection pressure) were investigated parametrically for elucidating the heat transfer to the wall and ratio of heat loss to total combustion heat. Furthermore, heat transfer coefficients were obtained from the measurements, and the relationships between the Nusselt number and Reynolds number were investigated to clarify the phenomenon of heat transfer in diesel engines. The general conclusions are discussed in turn in this chapter.

8.1 MAIN FINDINGS OF THIS STUDY

Heat transfer under baseline conditions

The baseline conditions for investigating the heat transfer were selected as follows: injection pressure of 120 MPa, impingement distance of 40 mm, nozzle hole diameter of 0.133 mm, and 21% oxygen concentration. The investigation aimed to clarify the relationship between the impinging spray/flame and local heat flux under baseline conditions. To investigate this

relationship, three conditions of non-evaporation, evaporation, and combustion were considered in this study. It was found that, under non-evaporating spray, the spray tip penetration increased with time, although the fuel has done injected. Under evaporation conditions, the liquid length penetration was saturated under 40 mm and remained constant, while the fuel continued to be injected. This means that, under baseline conditions, the liquid phase of the spray could not reach the wall. In other words, the impingement distance of 40 mm was enough to generate a conversion from the liquid to vapor phase before the fuel reached the wall. In the vapor area around the center of impingement, the flame's natural luminosity occurrence was identified after reaching a certain temperature for ignition.

Regarding the spatial nonuniformity of the spray and flame flow, the time histories of local heat fluxes were different at the three measurement locations (Position1, Position2, and Position3). The observed increase in local heat flux at Position1 could be interpreted as resulting from the effect of convection when a turbulent part of the evaporating spray impinges the wall. Then, the large effect of combustion gas velocity was responsible for starting the local heat flux peak at Position2. Wall friction and momentum loss took place due to turbulent mixing, and the local heat flux at Position3 was significantly lower than the heat fluxes at the other positions. The total transferred heat under the base condition was around 30 joules.

Effects of impingement distances

To clarify the effects of impingement distance on the wall heat transfer, three impingement distances from the injection tip to the wall were investigated. The variation of impingement distance has an important role in the spray behavior, combustion development, soot emission, and heat loss. Comparing three impingement distances under non-evaporating spray, it was found that they had similar penetrations until impingement on the wall, but they differed from each other after impingement due to the impingement timing difference. However, the spray tip penetration velocity showed almost the same inclination after impingement among the three impingement distances.

Under combustion conditions, it was confirmed that the ignition delay became longer with distance. At $D_{imp} = 40$ mm, a higher flame area, mean temperature, and KL factor were observed compared with the other impingement distances. This means that deteriorated

combustion occurred at this distance, thereby leading to high soot formation. However, at $D_{imp} = 30$ mm, impinged spray droplets were rolled up, caused by the shorter impingement distance. This resulted in better mixing with ambient air, enhancing the oxidation of fuel and reducing soot formation. When increasing the distance to 50 mm, the flame area, mean temperature, and KL factor had significantly lower values. At $D_{imp} = 50$ mm, with a longer impinging path, combustion became slower, with a lower temperature, and soot formation was reduced due to the improved fuel air mixing before combustion occurrence.

Among the three different distances, 40 mm had the maximum local heat flux and heat loss on the wall. This was caused by high temperature near the wall and a large flame contact area. The larger flame contact during resident time on the wall led to a high wall surface temperature; therefore, it increased the rate of heat transfer. The ratio of heat loss through the wall to total combustion heat at different impingement distances was around 14–15%.

Effects of injection pressure

The effects of the injection pressure on the spray motion, flame behavior, and wall heat transfer were investigated. Under non-evaporating and evaporating non-combustion, it was found that the spray development and spray tip penetration depended highly on the injection. The higher the injection pressure became, the more the spray would spread to a larger circumferential area on the flat wall and the greater the spray tip penetration would be. With evaporating spray, an increase in velocity with higher injection pressure led to more effective atomization. Consequently, a more homogeneous mixture distribution emerged due to the faster evaporation rate.

Injection pressure also had a significant effect on the heat flux characteristics in the non-combustion condition. By increasing the injection pressure, the initiation of the local heat flux increase occurred at an earlier point, which was associated with the increased spray velocity and led to earlier turbulent convection. As a result, the hot gas flowed toward a wider wall area, which was an influential factor for the increasing temporal variations of the total heat flux.

In the case of combustion, the transferred heat increased significantly, and the highest transferred heat was observed at 180 MPa among both lower injection pressures (80 and 120 MPa). The flame velocity, which relates to the heat transfer coefficient, increased with the

injection pressure, leading to hot gas flow spreading to the circumferential area of the flat wall. Regarding both the combustion and non-combustion conditions, they had similar waveforms and orders of heat transfer coefficients at all the positions and injection pressures. This indicates that, in combustion, flow induced by the injected spray is dominant for the heat transfer to the wall.

Effects of the nozzle hole diameter

The effects of the nozzle hole diameter on heat transfer were considered in this study. It was found that, under the non-combustion condition, the local heat flux rises at Position1 became earlier and higher at $D_{\text{hole}} = 0.133$ mm in which larger nozzle hole diameter comparing $D_{\text{hole}}=0.122$ mm. It increased due to the higher momentum and velocities stemming from an increased fuel injection rate. Similarly, under the combustion condition, higher heat flux values at Position1 and Position2 were obtained at a larger nozzle diameter. However, a smaller nozzle hole diameter with smaller droplet size can promote spray atomization and entrainment. As a result, the flame develops into a wider circumferential area at $D_{\text{hole}} = 1.22$ mm. As a consequence of this phenomenon, Position3 exhibited an earlier and higher increase, leading to a greater rate of heat transfer due to the larger affected area.

Regarding the effect of the injection pressure and nozzle hole diameter on the wall heat loss, the larger the nozzle hole diameter, the less heat loss was generated at injection pressures of 80 and 120 MPa. The flame temperature was an influencing factor on heat loss under these conditions. In contrast, the larger nozzle hole diameter caused more heat loss at an injection pressure of 180 MPa. Local high-temperature end gas regions had a dominant effect on heat loss at this injection pressure/nozzle hole diameter condition.

Effects of oxygen concentration

The effects of oxygen concentration on heat transfer were investigated. By comparing the temperature distributions with different oxygen concentrations, it was found that the temperature distribution and flame contact area were decreased with a decreasing oxygen concentration. When the combustion temperature was low, the temperature difference between the flame and wall surface was smaller. As a result, the local heat flux decreased, and the transferred heat value was also reduced.

Combined effects

Combined effects of the impingement distance and injection pressure on heat transfer were examined. It was found that the transferred heat significantly increased at an injection pressure of 180 MPa. Especially, it increased dramatically when combined with a longer impingement distance. This was probably due to the convection by turbulence from spray impinging, which took time to reach the wall because of the longer impingement distance. As a result, it reached the wall simultaneously with the ignition, which had a major influence on the local heat flux values. In contrast, the combination of $D_{imp}/P_{inj}=30/80$ had a lower local heat flux due to a large liquid spray impingement to the wall.

Under the combined effects of the oxygen concentration and injection pressure, it was found that lower oxygen concentrations consistently reduced the heat transfer on the wall in all conditions. The transferred heat decreased even when the injection pressure was increased. This occurred because the flame temperature was lower compared with the base oxygen concentration of $O_2 = 21\%$.

As a new method for determining the characteristic velocity to calculate the Re number, flamelet velocity has been proposed. Flamelet velocity is determined according to the local combustion flame motion near the wall, which has a direct effect on the local heat flux waveform characteristic. In this study, using the flamelet velocity value, it was found that the Nu number was proportional to the Re number. Its mean, value of Nu number is high when the Re number value increased.

Summary

In summary, this dissertation found that the wall impinging spray flame is a vital factor with a significant effect on heat transfer characteristics. Comparing non-combustion and combustion, around 30% of the transferred heat through the wall was transferred by the convection of non-combustion evaporating spray. In terms of the effect of impingement distance, a distance of 40 mm resulted in substantial heat transfer due to the high temperature near wall and long flame contact period. Similarly, the results showed that the heat transfer increased when the nozzle hole diameter was decreased to 0.122 mm. In contrast, a high injection pressure reached the peak heat transfer, which was attributed to a high flame velocity

with the increasing heat transfer coefficient due to the increased fuel injection rate. However, when the oxygen concentration decreased to 16%, less heat transfer was generated, even though the injection pressures increased. The lower flame temperature and reduced flame contact area period were influencing factors on heat loss under these conditions. Considering the combined effects, heat transfer significantly increased under a high injection pressure and longer impingement distance. This was probably because the ignition occurred almost simultaneously with the impingement timing, which had a major effect on the local heat flux values, and consequently, the total heat transfer.

Regarding some parameter conditions that were investigated, decreasing the oxygen concentration was an effective parameter when it came to reducing the heat transfer on the wall due to the lower temperature distribution. Furthermore, the cooling effect from liquid fuel adhering to the wall could have influenced the slow heat transfer rate. This was achieved by the combined effects of the lower impingement distance and lower injection pressure.

This study proposed that characteristic velocity in the heat transfer correlation in diesel engines is defined by flamelet velocity. Flamelet velocity was determined from the assumption that local combustion flame motion near the wall has a direct influence on the local heat flux waveform characteristics.

8.2 RECOMMENDATIONS FOR FUTURE WORKS

Several recommendations can be made for future work in this field. The detailed mechanism of the heat transfer on the flat wall impinging spray flames needs to be further investigated. Therefore, to better understand the spray flame velocity, a particle image velocimetry (PIV) system is needed at all conditions. In addition, future study should seek to improve the systems for measuring pressure and gas temperature, allowing better calculation of the heat release and heat transfer coefficient.

Some effect parameters for the wall heat transfer were investigated in this study; however, the effects of split injection and similar injection rates with different nozzle hole diameters should also be investigated in future research to better understand factors that will improve the thermal efficiency of small diesel engines. In addition, computational fluid

dynamics should be applied to obtain valuable information on the physical phenomena associated with heat transfer diesel engine combustion.

The main goal in this study was reducing heat loss for improving the thermal efficiency in a small diesel engine. Although the ambient conditions and wall temperature were controlled, such that the experimental setup was like a real diesel engine, a turbulent flow may affect the combustion behavior, and thus, the rate of heat transfer. Therefore, future studies on the current topic should investigate the heat transfer characteristics by applying different chamber shapes and injection amounts, as well as using multi-hole injectors, to include multiple injection strategies.

REFERENCES

- [1] BP, “67 th edition Contents is one of the most widely respected,” *Stat. Rev. World Energy*, pp. 1–56, 2018.
- [2] ExxonMobil, “2017 Outlook for Energy,” *Outlook for Energy*, p. 52, 2017.
- [3] ExxonMobil, “2018 Outlook for Energy: A View to 2040,” *Outlook*, 2018.
- [4] Continental-automotive, *Worldwide Emission Standards and Related Regulations*. 2019.
- [5] M. Kono, M. Basaki, M. Ito, T. Hashizume, S. Ishiyama, and K. Inagaki, “Cooling Loss Reduction of Highly Dispersed Spray Combustion with Restricted In-Cylinder Swirl and Squish Flow in Diesel Engine,” *SAE Int. J. Engines*, pp. 504–515, 2012.
- [6] J. B. Heywood, *Internal Combustion Engine Fundamentals*, vol. 21. New York: McGraw-Hill, 1988.
- [7] T. Tatsumi, S. Maeda, S. Miyata, Y. Kobashi, and *et al.*, “A Study on the Wall Heat Loss in Diesel Spray Flame (First Report: Effect of injection pressure on the heat flux),” *Trans. Soc. Automot. Eng. Japan*, vol. 47, no. 6, pp. 1291–1296, 2016.
- [8] T. Tatsumi, S. Maeda, M. Nakata, Y. Kobashi, and *et al.*, “A Study on the Wall Heat Loss in Diesel Spray Flame (Third report: Effects of Fuel Heating on the Heat Flux),” *27th Intern. Combust. Engine Symp.*, p. in japanese, 2016.
- [9] T. Tatsumi, S. Maeda, M. Nakata, Y. Kobashi, and *et al.*, “A Study on the Wall Heat Loss in Diesel Spray Flame (Fourt Report: Effect of Nozzle Hole Diameter on the Heat Flux),” *JSAE Trans.*, vol. 49, no. 2, pp. 144–149, 2018.
- [10] M. Nakata, N. Arai, S. Maeda, T. Tatsumi, E. Matsumura, and J. Senda, “A Study on the Wall Heat Loss in Diesel Spray Flame (Sixth Report: Effects of Impingement Distance and Inclination Angel of The Wall on The Heat Flux),” in *Proceeding of 2016 JSAE Annual Congress*, 2016.
- [11] G. Borman and K. Nishiwaki, “Internal-combustion engine heat transfer,” *Prog. Energy Combust. Sci.*, vol. 13, no. 1, pp. 1–46, 1987.
- [12] T. Lefevre, P. S. Myers, and O. A. Uyehara, “Experimental Instantaneous Heat Fluxes in a Diesel Engine and Their Correlation,” 1969.
- [13] G. Eichelberg, “Some New Investigations on Old Combustion Engine Problems,” *Engineering*, vol. 148, pp. 463–446, 547–560, 1939.
- [14] W. J. D. Annand, “Heat Transfer in the Cylinder of Reciprocating Internal Engines,”

- Proc. Instn Mech. Engineers*, vol. 177, no. 36, pp. 973–990, 1963.
- [15] G. Woschni, “A Universally Applicable Equation for the Instantaneous Heat Transfer Coefficient in the Internal Combustion Engine,” 1967.
- [16] G. Sitkei and GV Ramanaiah, “A Rational Approach for Calculation of Heat Transfer in Diesel Engines,” *SAE Tech. Pap. 720027*, pp. 165–174, 1972.
- [17] T. Morel and R. Keribar, “A Model for Predicting Spatially and Time Resolved Convective Heat Transfer in Bowl-in-Piston Combustion Chambers,” *SAE Tech. Pap. 850204*, 1985.
- [18] T. Morel, C. I. Rackmil, R. Keribar, and M. J. Jennings, “Model for Heat Transfer and Combustion In Spark Ignited Engines and its Comparison with Experiments,” *SAE Tech. Pap. 880198*, 1988.
- [19] G. F. Hohenberg, “Advanced Approaches for Heat Transfer Calculations,” *SAE Tech. Pap. 790825*, p. 19, 1979.
- [20] S. Bin Han, Y. J. Chung, Y. J. Kwon, and S. Lee, “Empirical Formula for Instantaneous Heat Transfer Coefficient in Spark Ignition Engine,” *SAE Tech. Pap. 972995*, 1997.
- [21] J. Chang, O. Güralp, Z. Filipi, D. N. Assanis, and et al., “New heat transfer correlation for an HCCI engine derived from measurements of instantaneous surface heat flux,” *SAE Tech. Pap. 2004-01-2996*, 2004.
- [22] C. A. Finol and K. Robinson, “Thermal modelling of modern engines: A review of empirical correlations to estimate the in-cylinder heat transfer coefficient,” *Proc. Inst. Mech. Eng. Part D J. Automob. Eng.*, vol. 220, no. 12, pp. 1765–1781, 2006.
- [23] T. Kuboyama and Y. Moriyoshi, “Heat Transfer Analysis in a Diesel Engine Based on a Heat Flux Measurement using a Rapid Compression and Expansion Machine,” *SAE Tech. Pap. 2017-32-0115*, p. 6, 2017.
- [24] N. Katsura, M. Saito, J. Senda, and H. Fujimoto, “Characteristics of a Diesel Spray Impinging on a Flat Wall,” *SAE Tech. Pap. 890264*, 1989.
- [25] L. M. Pickett and J. J. López, “Jet-Wall Interaction Effects on Diesel Combustion and Soot Formation Reprinted From : Compression Ignition Combustion Processes 2005,” *SAE Tech. Pap. 2005-01-0921*, p. 17, 2005.
- [26] L. Zhao, R. Torelli, X. Zhu, R. Scarcelli, and et al., “An Experimental and Numerical Study of Diesel Spray Impingement on a Flat Plate,” *SAE Int. J. Fuels Lubr.*, vol. 10, no. 2, pp. 2017-01–0854, 2017.

- [27] S. W. Park and C. S. Lee, "Macroscopic and microscopic characteristics of a fuel spray impinging on the wall," *Exp. Fluids*, vol. 37, no. 5, pp. 745–762, 2004.
- [28] Y. Zama, Y. Odawara, and T. Furuhashi, "Experimental investigation on velocity inside a diesel spray after impingement on a wall," *Fuel*, vol. 203, pp. 757–763, 2017.
- [29] G. Bruneaux, "Combustion Structure of Free and Wall-Impingement Diesel Jets by Simultaneous Laser-Induced Fluorescence of Formaldehyde, Poly-Aromatic Hydrocarbons, and Hydroxides," *Int. J. Engine Res.*, vol. 9, no. 3, pp. 249–265, 2008.
- [30] T. Kogo, Y. Hamamura, K. Nakatani, T. Toda, A. Kawaguchi, and A. Shoji, "High Efficiency Diesel Engine with Low Heat Loss Combustion Concept - Toyota 's Inline 4-Cylinder," *SAE Int.*, no. 2016-01-0658, 2016.
- [31] Y. Wakisaka, M. Inayoshi, K. Fukui, H. Kosaka, and *et al.*, "Reduction of Heat Loss and Improvement of Thermal Efficiency by Application of 'Temperature Swing' Insulation to Direct-Injection Diesel Engines," *SAE Int. J. Engines*, vol. 9, no. 3, pp. 2016-01-0661, 2016.
- [32] K. Fukui, Y. Wakisaka, K. Nishikawa, Y. Hattori, H. Kosaka, and A. Kawaguchi, "Development of Instantaneous Temperature Measurement Technique for Combustion Chamber Surface and Verification of Temperature Swing Concept," *SAE Tech. Pap. 2016-01-0675*, 2016.
- [33] N. Uchida. and H. Osada., "A New Piston Insulation Concept for Heavy-Duty Diesel Engines to Reduce Heat Loss from the Wall," *SAE Int. J. Engines 2017-24-0161.*, pp. 10(5):2565-2574, 2017.
- [34] S. Li, T. Kamimoto, S. Kobori, and Y. Enomoto, "Heat Transfer from Impinging Diesel Flames to the Combustion Chamber Wall," *SAE Tech. Pap. 970896*, 1997.
- [35] J. Dahlstrom, O. Andersson, H. Persson, and M. Tuner, "Effect of Spray-Swirl Interactions on Heat Losses in a Light Duty Diesel Engine," *ASME 2015 Int. Mech. Eng. Congr. Expo. IMECE2015*, pp. 1–11, 2015.
- [36] J. Senda, H. Fujimoto, M. Kobayashi, K. Yamamoto, and Y. Enomoto, "Heat Transfer Characteristics of a Diesel Spray Impinging on a Wall," *Transl. from J. MESJ*, no. 9, pp. 3–12, 1995.
- [37] J. Senda, K. Yamada, H. Fujimoto, and " Miki, H., "The Heat-transfer Characteristics of a Small Droplet Impinging upon a Hot Surface," *JSME Int. J. Ser. II*, vol. 31, no. 1, 1988.
- [38] S. Kimura, M. Koike, Y. Matsui, and Y. Enomoto, "Effect of combustion chamber

- specifications and swirl ratio on transient heat transfer and combustion in a DI diesel engine,” *3rd Int. Symp. diagnostics Model. Combust. Intern. engines (COMODIA 94)*, pp. 131–138, 1994.
- [39] K. Arato and T. Takashima, “A Study on Reduction of Heat Loss by Optimizing Combustion Chamber Shape,” *SAE Tech. Pap. 2015-01-0786*, 2015.
- [40] F. Perini, A. Dempsey, R. Reitz, D. Sahoo, B. Petersen, and P. Miles, “A Computational Investigation of the Effects of Swirl Ratio and Injection Pressure on Mixture Preparation and Wall Heat Transfer in a Light-Duty Diesel Engine,” *SAE Tech. Pap. 2013-04-08*, p. 17, 2013.
- [41] D. Mayer, A. Seelig, T. Kunz, F. Kopple, M. Mansbart, and M. Bargende, “Experimental Investigation of Flame-Wall-Impingement and Near-Wall Combustion on the Piston Temperature of a Diesel Engine Using Instantaneous Surface Temperature Measurements,” *SAE Tech. Pap. 2018-01-1782*, pp. 1–18, 2018.
- [42] H. Osada, N. Uchida, K. Shimada, and Y. Aoyagi, “Reexamination of Multiple Fuel Injections for Improving the Thermal Efficiency of a Heavy-Duty Diesel Engine,” *SAE Tech. Pap. 2013-01-0909*, 2013.
- [43] X. Cheng, L. Chen, F. Yan, G. Hong, Y. Yin, and H. Liu, “Investigations of Split Injection Strategies for the Improvement of Combustion and Soot Emissions Characteristics Based on the Two-Color Method in a Heavy-Duty Diesel Engine,” *SAE Tech. Pap. 2013-01-2523.*, 2013.
- [44] T. Kuboyama and H. Kosaka, “A Measurement of Heat loss in Combustion Chamber of DI Diesel Engines,” *Marit. Res. Inst. Technol. Saf.*, vol. 8, no. 215–221, pp. 89–96, 2008.
- [45] Li Kuichun, “Effects of Wall Impingement and Multiple Injection on Mixture Formation and Combustion Processes of Diesel Spray,” Hiroshima University, Dissertation, 2014.
- [46] K. Li, K. Nishida, Y. Ogata, and B. Shi, “Effect of flat-wall impingement on diesel spray combustion,” *Proc. Inst. Mech. Eng. Part D J. Automob. Eng.*, vol. 229, no. 5, pp. 535–549, 2014.
- [47] X. Wang, Z. Huang, W. Zhang, O. A. Kuti, and K. Nishida, “Effects of ultra-high injection pressure and micro-hole nozzle on flame structure and soot formation of impinging diesel spray,” *Appl. Energy*, vol. 88, no. 5, pp. 1620–1628, 2011.
- [48] J. E. Dec and D. R. Tree, “Diffusion-flame/wall Interactions in a Heavy-Duty DI

- Diesel Engine,” *SAE Tech. Pap. 2001-01-1295*, 2001.
- [49] J. D. Naber and R. D. Reitz, “Modeling Engine Spray / Wal Impingement,” *SAE Tech. Pap. 880107*, 1988.
- [50] C. Bai and A. D. Gosman, “Development of Methodology for Spray Impingement Simulation,” *SAE Tech. Pap. 950283*, 1995.
- [51] J. Senda, M. Kobayashi, S. Iwashita, and H. G. Fujimoto, “Modeling of diesel spray impinging on flat wall,” *SAE Tech. Pap. 941894*, 1994.
- [52] J. Senda, M. Kobayashi, S. Iwashita, and H. Fujimoto, “Modeling of diesel spray impinging on flat wall,” *Int. J. JSME Ser. B Fluids Therm. Eng.*, vol. 39, no. 4, pp. 859–866, 1996.
- [53] J. Senda, T. Kanda, M. Ai-roub, and P. V Farrell, “Modeling Spray Impingement Considering Fuel Film Formation on the Wall,” *SAE 1997 Trans. - J. Engines*, vol. 106, no. 3, pp. 37–51, 1997.
- [54] A. L. N. Moreira, A. S. Moita, and M. R. Panão, “Advances and challenges in explaining fuel spray impingement: How much of single droplet impact research is useful?,” *Prog. Energy Combust. Sci.*, vol. 36, no. 5, pp. 554–580, 2010.
- [55] S. Y. Lee and S. U. Ryu, “Recent progress of spray-wall interaction research,” *J. Mech. Sci. Technol.*, vol. 20, no. 8, pp. 1101–1117, 2006.
- [56] H. Zhao and N. Ladommatos, “Optical diagnostics for soot and temperature in diesel engines,” *Prog. Energy Combust. Sci.*, vol. 24, no. 97, pp. 221–255, 1998.
- [57] H. Zhao and N. Ladommatos, *Engine Combustion Instrumentation and Diagnostics*. Warrendale, Pa. : Society of Automotive Engineers, 2001.
- [58] L. M. Pickett, J. Manin, C. L. Genzale, D. L. Siebers, M. P. B. Musculus, and C. A. Idicheria, “Relationship Between Diesel Fuel Spray Vapor Penetration/Dispersion and Local Fuel Mixture Fraction,” *SAE Int. J. Engines*, vol. 4, no. 1, pp. 2011-01–0686, 2011.
- [59] J. Palmer, M. Ramesh, V. Kirsch, M. Reddemann, and R. Kneer, “Spray Analysis of C 8 H 18 O Fuel Blends using High-Speed Schlieren Imaging and Mie Scattering,” *SAE Tech. Pap. 2015-24-2478*, 2015.
- [60] A. Montanaro, M. Migliaccio, L. Allocca, V. Fraioli, and *et al.*, “Schlieren and Mie Scattering Visualization for Single-Hole Diesel Injector under Vaporizing Conditions with Numerical Validation,” *SAE Tech. Pap. 2014-01-1406*, 2014.
- [61] J. T. Hodges, T. A. Baritaud, and T. A. Heinze, “Planar Liquid and Gas Fuel and

- Droplet Size Visualization in a DI Diesel Engine¹,” *SAE Tech. Pap.* 910726, 1991.
- [62] T. Hoffmann, P. Hottenbach, H.-J. Koss, C. Pauls, and G. Grünefeld, “Investigation of Mixture Formation in Diesel Sprays under Quiescent Conditions using Raman, Mie and LIF Diagnostics,” vol. 2008, no. 724, pp. 776–790, 2008.
- [63] G.S. Settles, *Schlieren and Shadowgraph Techniques: Visualizing Phenomena in Transparent Media (Experimental Fluid Mechanics)*. Springer-Verlag Berlin Heidelberg, 2001.
- [64] G. S. Settles and M. J. Hargather, “A review of recent developments in schlieren and shadowgraph techniques,” *Meas. Sci. Technol.*, vol. 28, no. 4, 2017.
- [65] L. M. Pickett, S. Kook, and T. C. Williams, “Visualization of Diesel Spray Penetration, Cool-Flame, Ignition, High-Temperature Combustion, and Soot Formation Using High-Speed Imaging,” *SAE Int. J. Engines*, vol. 2, no. 1, pp. 2009-01–0658, 2009.
- [66] J. Pastor, J. M. Garcia-Oliver, A. Garcia, W. Zhong, C. Micó, and T. Xuan, “An Experimental Study on Diesel Spray Injection into a Non-Quiescent Chamber,” *SAE Int. J. Fuels Lubr.*, vol. 10, no. 2, pp. 2017-01–0850, 2017.
- [67] J. V. Pastor, R. Payri, J. M. Garcia-Oliver, and F. J. Briceño, “Schlieren Methodology for the Analysis of Transient Diesel Flame Evolution,” *SAE Int. J. Engines*, vol. 6, no. 3, pp. 2013-24–0041, 2013.
- [68] J. D. Naber and D. L. Siebers, “Effects of Gas Density and Vaporization on Penetration and Dispersion of Diesel Sprays,” *SAE Tech. Pap.* 960034, 1996.
- [69] L. Pickett, S. Kook, and T. Williams, “Transient Liquid Penetration of Early-Injection Diesel Sprays,” *SAE Int. J. Engines*, vol. 2, no. 1, pp. 785–804, 2009.
- [70] C. Idicheria and L. Pickett, “Quantitative Mixing Measurements in a Vaporizing Diesel Spray by Rayleigh Imaging,” *SAE Tech. Pap.* 2007-01-0647, 2007.
- [71] F. Q. Zhao and H. Hiroyasu, “The applications of laser Rayleigh scattering to combustion diagnostics,” *Prog. Energy Combust. Sci.*, vol. 19, no. 6, pp. 447–485, 1993.
- [72] C. Espey, J. E. Dec, T. A. Litzinger, and D. A. Santavicca, “Quantitative 2-D Fuel Vapor Concentration Imaging in a Firing D . I . Diesel Engine Using Planar Laser-Induced Rayleigh Scattering,” *SAE Tech. Pap.* 940682, pp. 1851–1862, 1994.
- [73] C. Espey, J. E. Dec, T. A. Litzinger, and D. A. Santavicca, “Planar Laser Rayleigh Scattering for Quantitative Vapor-Fuel Imaging in a Diesel Jet,” *Combust. Flame*, no. 109, pp. 65–78, 1997.

- [74] J. Egermann, A. Gottler, and A. Leipertz, "Application of Spontaneous Raman Scattering for Studying the Diesel Mixture Formation Process Under Near-Wall Conditions," *SAE Tech. Pap. 2001-01-3496*, no. 724, 2001.
- [75] M. Taschek, J. Egermann, S. Schwarz, and A. Leipertz, "Quantitative analysis of the near-wall mixture formation process in a passenger car direct injection Diesel engine by using linear Raman spectroscopy," *Appl. Opt.*, no. 44, pp. 6606–6615, 2005.
- [76] M. Golombok and D. B. Pye, "Stimulated Raman scattering in diesel injected fuel sprays.," *J. Phys. D Appl. Phys.*, vol. 22, p. 851, 1989.
- [77] T. Brands, P. Hottenbach, H. Koss, G. Grünefeld, S. Pischinger, and P. Adomeit, "Quantitative Fuel-Air-Mixing Measurements in Diesel-Like Sprays Emanating from Convergent and Divergent Multi-Layer Nozzles," *SAE Int. J. Engines*, vol. 5, no. 2, pp. 430–445, 2012.
- [78] T. Raffius, C. Schulz, T. Ottenwälder, G. Grünefeld, and *et al.*, "Flame-temperature, light-attenuation, and CO measurements by spontaneous Raman scattering in non-sooting diesel-like jets," *Combust. Flame*, vol. 176, pp. 104–116, 2017.
- [79] T. Heinze and T. Schmidt, "Fuel-Air Ratios in a Spray, Determined between Injection and Autoignition by Pulsed Spontaneous Raman Spectroscopy," *SAE Tech. Pap. 892102*, 1989.
- [80] M. Hayashida, T. Yamato, H. Sekino, and Sugahara, K., "Investigation of Performance and Fuel Distribution of a Direct Injection Gas Engine Using LIF Measurement," *SAE Tech. Pap. 1999-01-3291*, 1999.
- [81] J. T. Kashdan, "Tracer LIF Visualisation Studies of Piston-Top Fuel Films in a Wall-Guided, Low-NOx Diesel Engine," *SAE Tech. Pap. 2008-01-2474*, no. 724, 2008.
- [82] H. Nakagawa, H. Endo, Y. Deguchi, M. Noda, H. Oikawa, and T. Shimada, "NO measurement in Diesel spray flame using laser induced fluorescence," *SAE Tech. Pap. Ser.*, no. 412, p. 970874, 1997.
- [83] S. De Zilwa and R. Steeper, "Predicting NOX Emissions from HCCI Engines Using LIF Imaging," *SAE Tech. Pap. 2006-01-0025*, 2006.
- [84] S. De Zilwa and R. Steeper, "Predicting Emissions from HCCI Engines using LIF Imaging," *SAE Tech. Pap. 2005-01-3747*, no. 724, 2005.
- [85] G. Bruneaux, "Mixing Process in High Pressure Diesel Jets by Normalized Laser Induced Exciplex Fluorescence Part II: Wall Impinging Versus Free Jet," *SAE Tech. Pap. 2005-01-2097*, 2005.

- [86] L.A. Melton, "Spectrally separated fluorescence emissions for diesel fuel droplets and vapor," *Appl. Opt.*, no. 22, pp. 2224–2226, 1983.
- [87] J. Senda, Y. Tanabe, H. Fujimoto, and Y. Fukami, "Visualization of Evaporative Diesel Spray Impinging Upon Wall Surface by Exciplex Fluorescence Method," *SAE Tech. Pap. 920578*, 1992.
- [88] H. Fujimoto, S. Kusano, and " Senda, J., "Distribution of Vapor Concentration in a Diesel Spray Impinging on a Flat Wall by Means of Exciplex Fluorescence Method -In Case of High Injection Pressure-," *SAE Tech. Pap. 972916*, 1997.
- [89] J. Senda, T. Kanda, M. Kobayashi, and H. (1997) Fujimoto, "Quantitative Analysis of Fuel Vapor Concentration in Diesel Spray by Exciplex Fluorescence Method," *SAE Tech. Pap. 970796*, 1997.
- [90] G. Bruneaux, "Mixing Process in High Pressure Diesel Jets by Normalized Laser Induced Exciplex Fluorescence Part I: Free Jet," *SAE Tech. Pap. 2005-01-2100*, 2005.
- [91] Y. Zhang, T. Yoshizaki, and Keiya Nishida, "Imaging of droplets and vapor distributions in a Diesel fuel spray by means of a laser absorption–scattering technique," *Appl. Opt.*, no. 39, pp. 6221–6229, 2000.
- [92] A. R. Chraplyvy, "Nonintrusive measurements of vapor concentrations inside sprays," *Appl. Opt.*, no. 20, p. 2620, 1981.
- [93] Y. Zhang, T. Ito, and K. Nishida, "Characterization of Mixture Formation in Split-Injection Diesel Sprays via Laser Absorption-Scattering (LAS) Technique," *SAE Tech. Pap. 2001-01-3498*, 2001.
- [94] Y. Matsumoto, J. Gao, M. Namba, and " Nishida, K., "Mixture Formation and Combustion Processes of Multi-Hole Nozzle with Micro Orifices for D.I. Diesel Engines," *SAE Tech. Pap. 2007-01-4049*, 2007.
- [95] J. Gao, Y. Matsumoto, M. Namba, and K. Nishida, "Group-Hole Nozzle Effects on Mixture Formation and In-cylinder Combustion Processes in Direct-Injection Diesel Engines," *SAE Tech. Pap. 2007-01-4050*, 2007.
- [96] S. Moon, Y. Matsumoto, and Nishida, K., "Entrainment, Evaporation and Mixing Characteristics of Diesel Sprays around End-of-Injection," *SAE Tech. Pap. 2009-01-0849*, 2009.
- [97] K. Yang, S. YASAKI, K. Nishida, and Y. Ogata, "Injection Strategy to Enhance Mixture Formation and Combustion of Fuel Spray in Diesel Engine," *SAE Tech. Pap. 2018-01-0241*, 2018.

- [98] Y. Wakisaka and A. Azetsu, "Effects of Fuel Injection Rate Shaping on Combustion and Emission Formation in Intermittent Spray," *SAE Tech. Pap. 2002-01-1159*, 2002.
- [99] G. R. Bower and D. E. Foster, "A Comparison of the Bosch and Zuech Rate of Injection Meters," *SAE Tech. Pap. 910724*, 1991.
- [100] Y. Matsui, T. Kamimoto, Matsuoka, and Shin, "A Study on the Time and Space Resolved Measurement of Flame Temperature and Soot Concentration in a D. I. Diesel Engine by the Two-Color Method," *SAE Tech. Pap. 790491*, 1979.
- [101] Y. Matsui, T. Kamimoto, and S. Matsuoka, "A Study on the Application of the Two-Color Method to the Measurement of Flame Temperature and Soot Concentration in Diesel Engines," *SAE Tech. Pap. 800970*, pp. 1808–1822, 1980.
- [102] S. K. Ahn, Y. Matsui, T. Kamimoto, and S. Matsuoka, "Measurement of flame temperature distribution in a D.I. diesel engine by means of image analysis of negative color photographs," *SAE Trans.*, vol. 90, no. 1, pp. 736–745, 1981.
- [103] H. C. Hottel and F. P. Broughton, "Determination of True Temperature and Total Radiation from Luminous Gas Flames: Use of Special Two-Color Optical Pyrometer," *Ind. Eng. Chem. - Anal. Ed.*, vol. 4, no. 2, pp. 166–175, 1932.
- [104] K. Li, M. Ido, Y. Ogata, K. Nishida, B. Shi, and D. Shimo, "Effect of Spray/Wall Interaction on Diesel Combustion and Soot Formation in Two-Dimensional Piston Cavity," *SAE Int. J. Engines 6(4)2061-2071*, p. 11, 2013.
- [105] K. Svensson, A. Mackrory, M. Richards, And, and D. Tree, "Calibration of an RGB, CCD Camera and Interpretation of its Two-Color Images for KL and Temperature," *SAE Tech. Pap. 2005-01-0648*, 2005.
- [106] R. Mahmud, T. Kurisu, K. Nishida, Y. Ogata, J. Kanzaki, and T. Tadokoro, "Experimental study on flat-wall impinging spray flame and its heat flux on wall under diesel engine-like condition: First report—effect of impingement distance," *Proc. Inst. Mech. Eng. Part D J. Automob. Eng.*, pp. 1–4, 2018.
- [107] D. P. D.- Theodore L. Bergman, Adrienne S. Lavine, Frank P. Incropera, *Fundamentals of Heat and Mass Transfer*, Eighth. John Wiley & Sons, Inc., 2017.
- [108] Eric Gingrich, J. Ghandhi, and R. Reitz, "Experimental investigation of piston heat transfer in a light duty engine under conventional diesel, homogeneous charge compression ignition, and reactivity controlled compression ignition combustion regimes," *SAE Tech. Pap. 2014-01-1182*, 2014.
- [109] G. Woschni and K. Huber, "The Influence of Soot Deposits on Combustion Chamber

- Walls on Heat Losses in Diesel Engines,” *SAE Tech. Pap.* 910297, 1991.
- [110] Z. Wang, S. Wu, Y. Huang, Y. Chen, and *et al.*, “Evaporation and ignition characteristics of water emulsified diesel under conventional and low temperature combustion conditions,” *Energies*, vol. 10, no. 8, 2017.
- [111] S. Li, T. Kamimoto, and S. Kobori, “Heat Transfer From Impinging Diesel Flames to the Combustion Chamber Wall,” *SAE Int. J. Fuels Lubr.* 5(1)1-6, 19972, no. 412, 2015.
- [112] H. Osada, N. Uchida, and Y. Zama, “An Analysis on Heat Loss of a Heavy-Duty Diesel Engine by Wall-Impinged Spray Flame Observation,” *SAE Tech. Pap.* 2015-01-1832., 2015.
- [113] T. Su, C. Chang, R. Reitz, P. Farrell, A. D. Pierpont, and T. C. Tow, “Effects of Injection Pressure and Nozzle Geometry on Spray SMD and D.I. Emissions,” *SAE Tech. Pap.* 952360, 1995.
- [114] M. Zheng, G. T. Reader, and J. G. Hawley, “Diesel engine exhaust gas recirculation - A review on advanced and novel concepts,” *Energy Convers. Manag.*, vol. 45, no. 6, pp. 883–900, 2004.
- [115] M. Z. Akop, Y. Zama, T. Furuhashi, and M. Arai, “Characteristics of Adhesion Diesel Fuel on an Impingement Disk Wall. Part 3: Ambient Pressure Effect,” *At. sprays*, vol. 24(7), pp. 625–650, 2014.
- [116] R. Gramlich, P. Leich, J. Kaleta, A. Miller, and *et al.*, “Air Entrainment and Momentum Distribution in the Near Field of Diesel Sprays from Group Hole Nozzles,” *ILASS Eur. 2016, 27th Annu. Conf. Liq. At. Spray Syst.*, pp. 4–7, 2016.
- [117] C. Baumgarten, *Mixture Formation in Internal Combustion Engine*. Springer, 2006.
- [118] T. Kuboyama, H. Kosaka, T. Aizawa, and Y. Matsui, “A Study on Heat Loss in DI Diesel Engines by Using a Rapid Compression and Expansion Machine (1st Report, The Effects of Oxygen Volume Fraction and Density of Ambient Gas on Heat Loss),” *Japan Soc. Mech. Eng.*, vol. 72, no. 721, pp. 2315–2322, 2006.
- [119] S. Fujikawa, M. Nakata, S. Maeda, N. Arai, and *et al.*, “Proposal of Wall Heat Transfer Coefficient Applicable to Spray-wall Interaction Process in Diesel Engines,” *Trans. Soc. Automot. Eng. Japan*, pp. 1120–1125, 2018.

ACKNOWLEDGEMENTS

This dissertation was accomplished at the Fluid Engineering Laboratory, Faculty of Engineering, University of Hiroshima. I would like to express my gratitude to all those who helped me during the working of this dissertation.

My deepest gratitude goes first and foremost to Professor. Keiya Nishida, my academic supervisors, for his constant encouragement, earnest guidance, constructive criticism and invaluable discussions throughout study in Fluid Engineering Laboratory.

Gratefulness is also given to Prof. Toru Kurisu (Mazda Co) and Prof. Yoichi Ogata, for their extremely valuable comments and helpful suggestions of this research work. Also, my sincere appreciation goes to the dissertation committee members: Professors Takuma Endo and Professor Yukihiro Matsumura.

I would like to thanks are also given to Mazda Co: Mr. Jun Kanzaki, Mr. Tadashi Tadokoro, and Mr. Makoto Namba, for their support with measurement in this study; M and K Group: Mr. Seong Bum Kim, Mr. Akgol Onur, Mr. Wang and Mr. Van, for their assistance in the experiment; FEST Lab: Dr. KIM Jae Heun, Mr. Saifiullah and FEST Lab members, for useful discussion and advise.

I would like to appreciate the Ministry of Education, Japan (Monbukagakusho), for sponsoring my studies by providing scholarship and tuitions fees. I would like to extend my thank is also given to Adhi Tama Institute of Technology, for financial and moral support during study in University of Hiroshima.

Last but not least, my deepest gratitude goes to my parent and family, especially to my wife, Iis Rohmawati, for her consistent love, encouragement, and support.

APPENDIX

Data Acquisition Flowchart

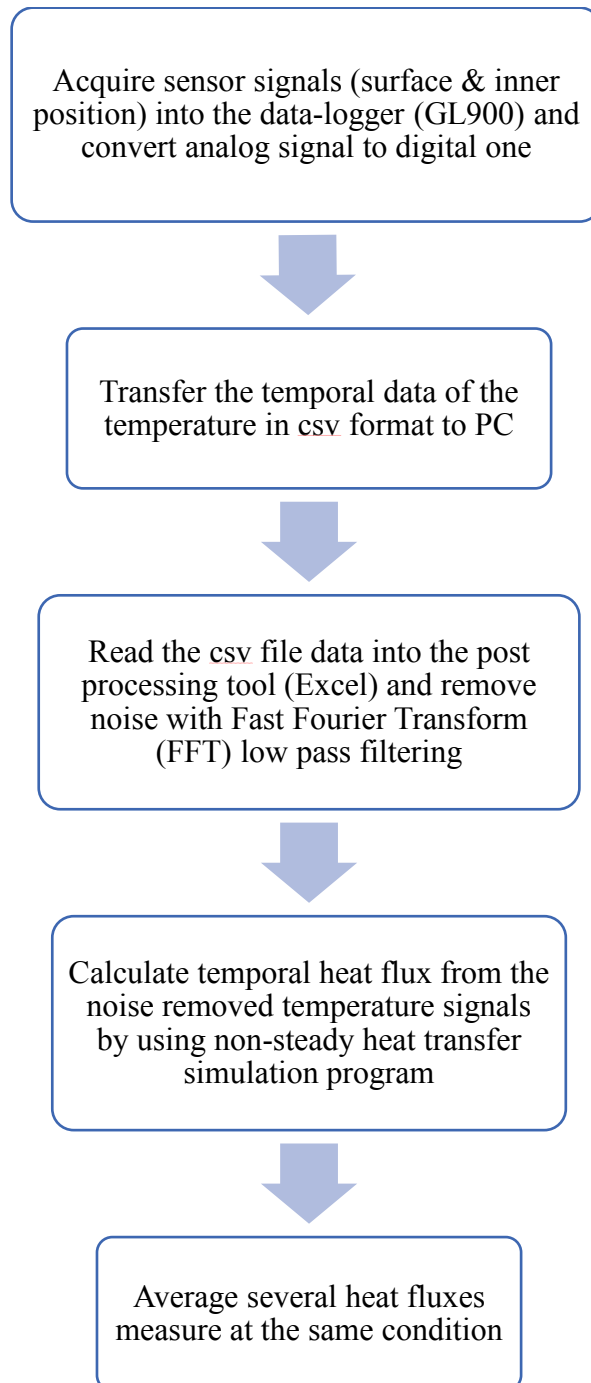


Figure 1. Flowchart of data acquisition

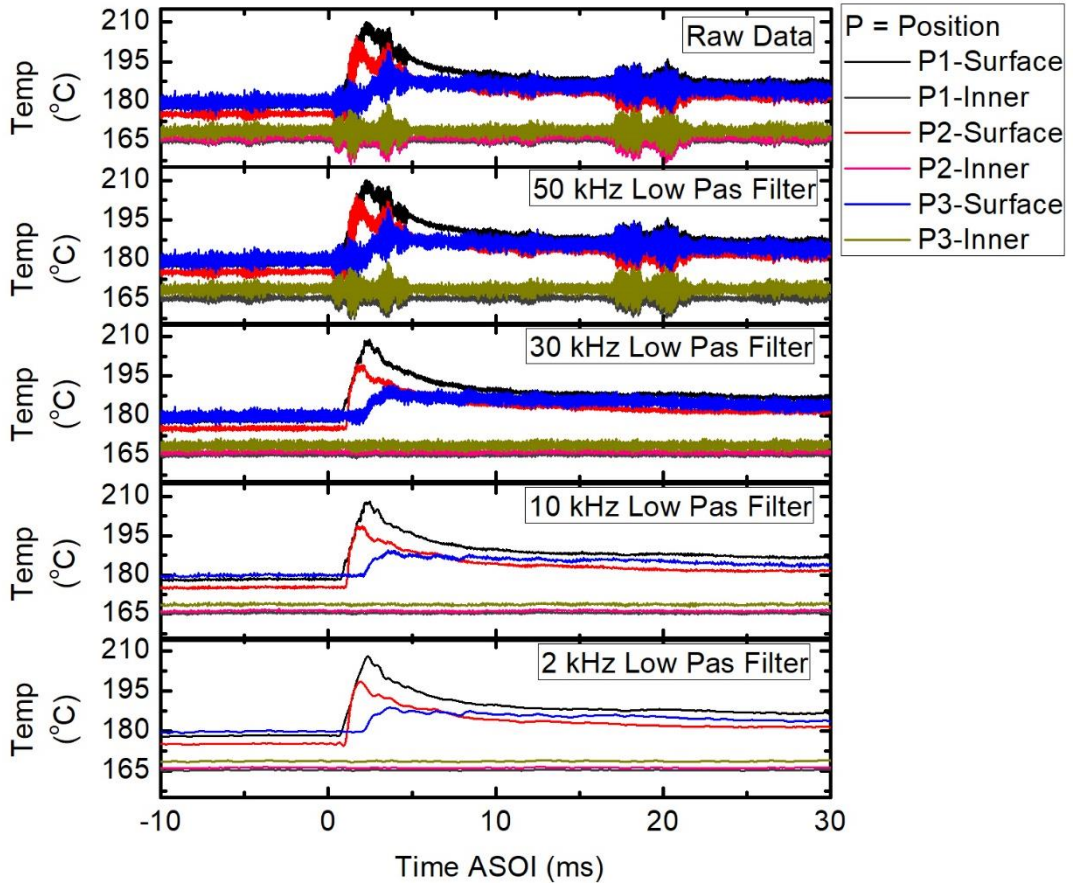


Figure 2. Various noise at surface and inner temperature

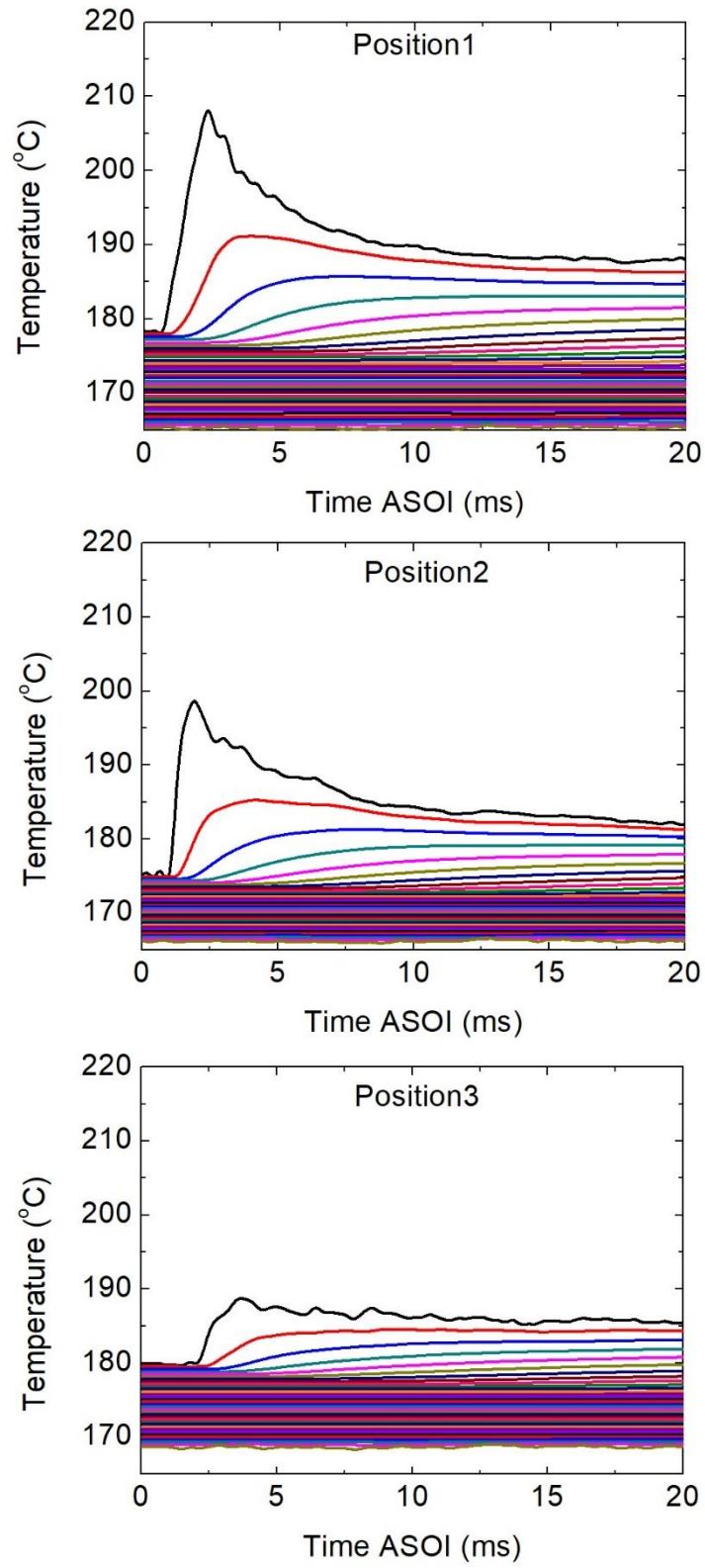


Figure 3. Temperature distribution at Position1, Position2 and Position3

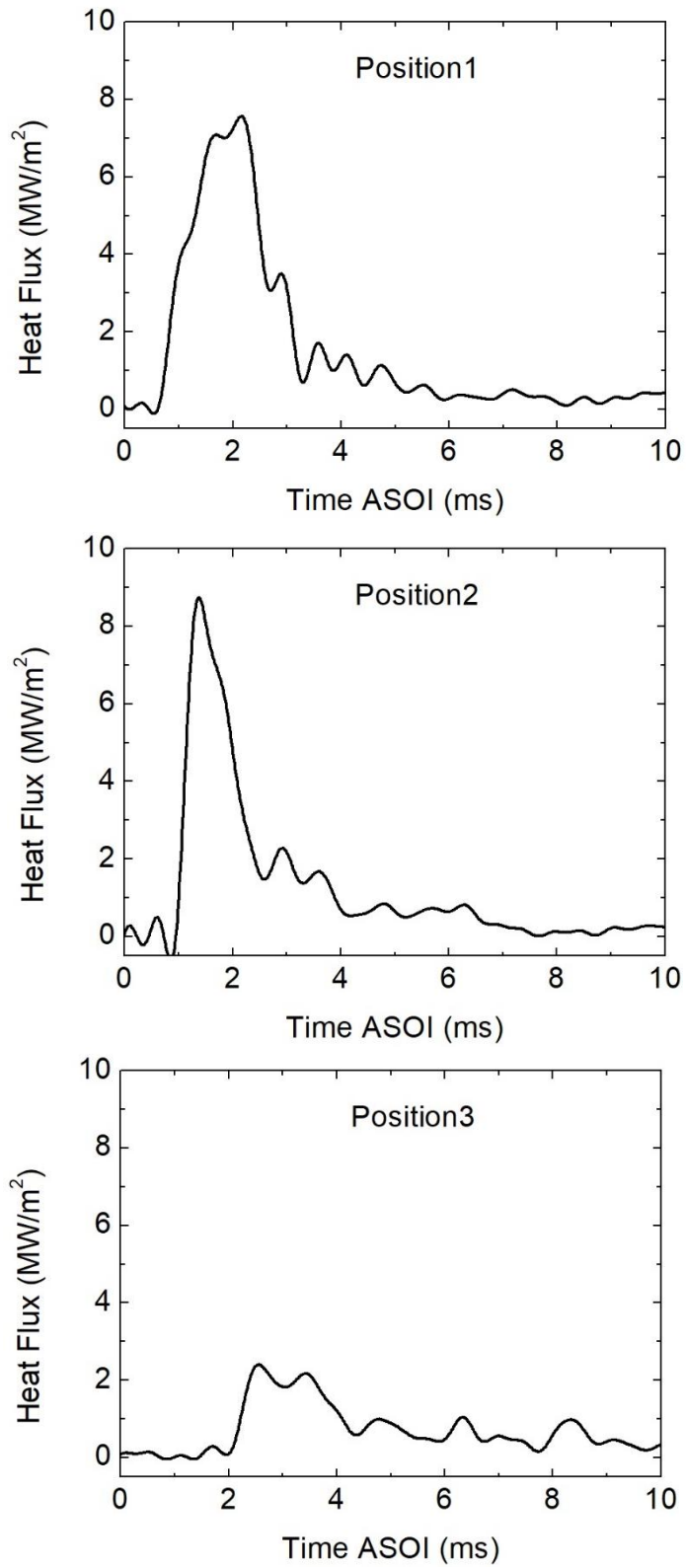


Figure 4. Temperature distribution at Position1, Position2 and Position3

Figure 1 and 2 shows flowchart of data acquisition and various noise. Since the electromotive force of the thermocouple is very small, noise is easy to get on the signal, and various noises such as 60 kHz power supply noise and high frequency propagation noise are carried. Therefore, we wrapped the compensating lead wire with aluminum foil, shielded the ground from the GL900, used the battery to drive the GL900 at the time of measurement, and took noise prevention measures. Even so, noise appeared on the signal waveform obtained as shown in Figure 2. Therefore, noise was removed by digital data such as filtering the digital output result from GL 900.

Figure 3. shows the temperature distribution of wall surface to inside the wall at Position1, Position2, and Position3. These results are obtained by solving the equation 2.14. Then, by applying the equation 2.16, the unsteady local heat flux can be observed at Figure 4.

Validation Between Experiment and Simulation

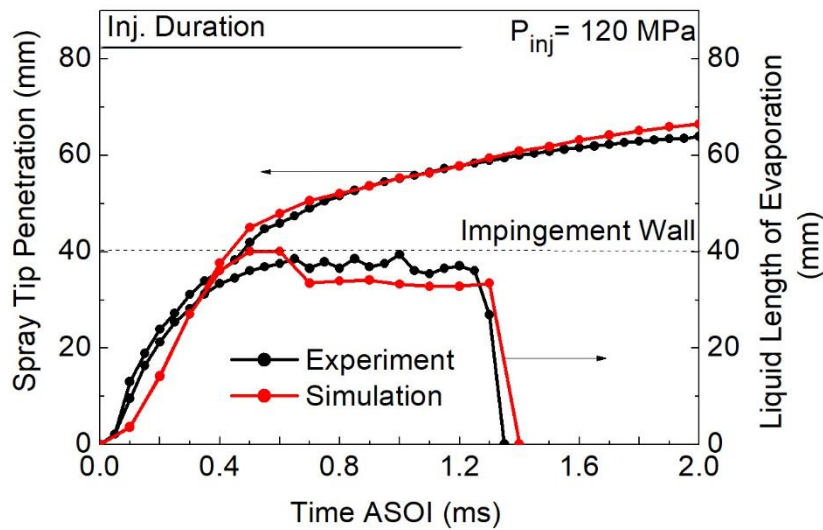


Figure 5. Temperature distribution at Position1, Position2 and Position3

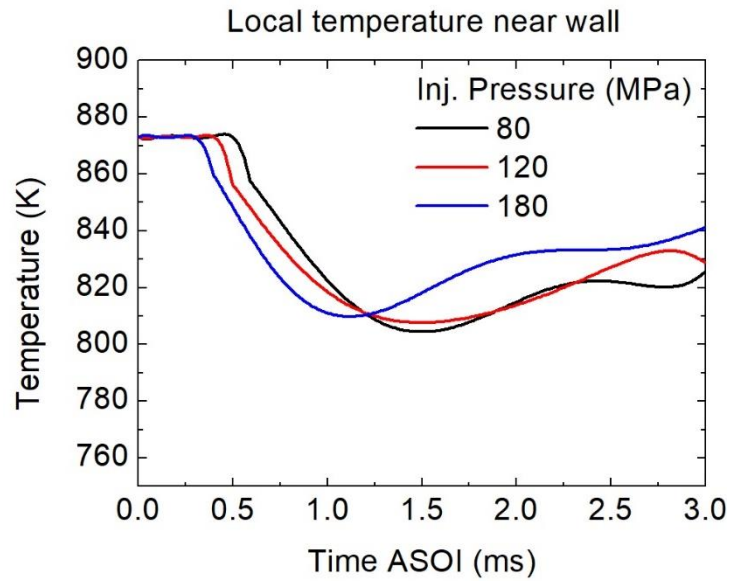
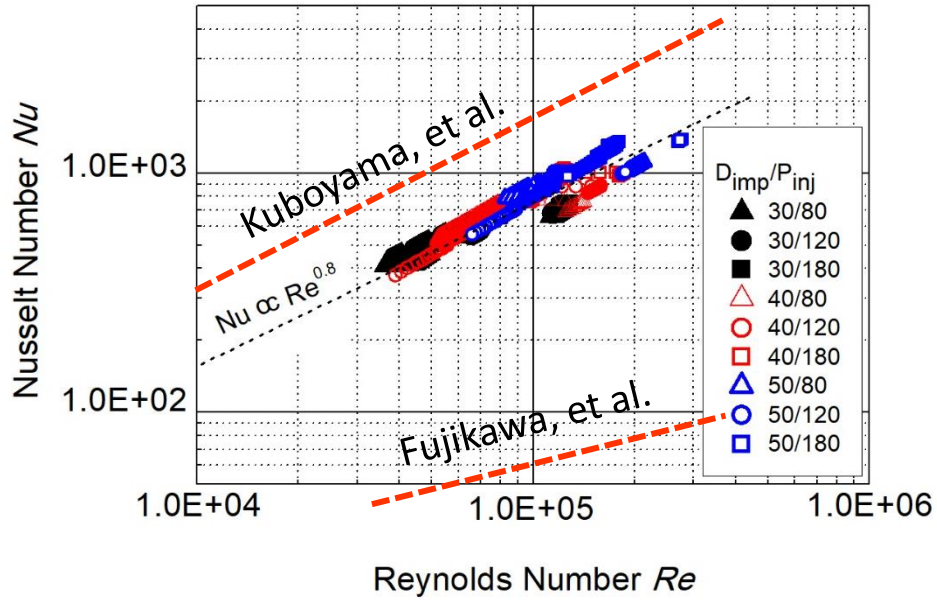


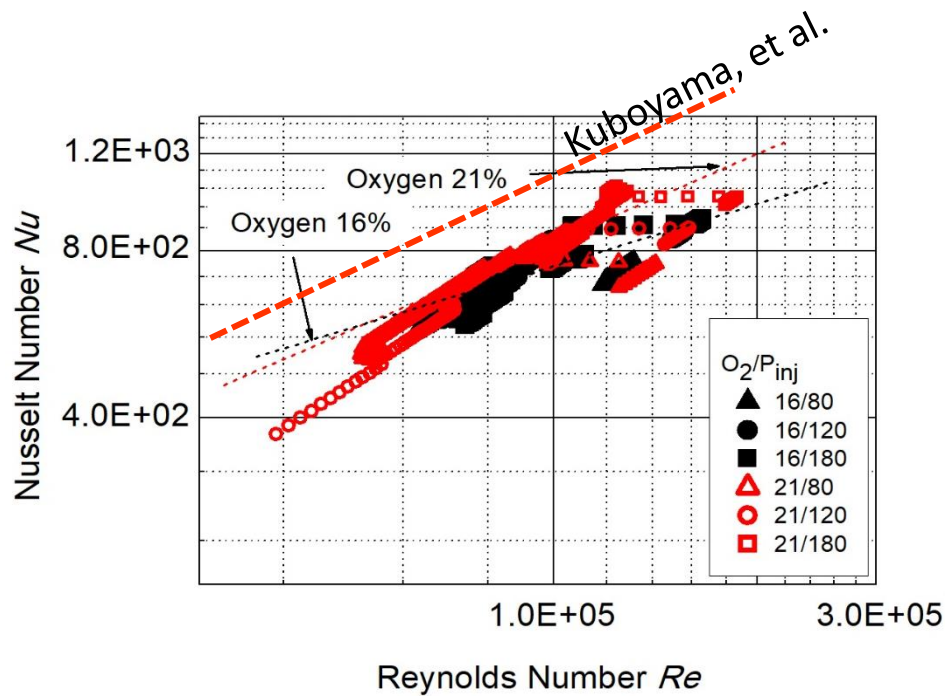
Figure 6. Temperature distribution at Position1, Position2 and Position3

In order to obtain gas temperature at non-combustion condition, the Converge CFD software was performed in this condition. Then to validate the results, comparison with experiment is made as shown in Figure 5. The simulation results may not be accurate with that of experiment, however, the diesel fuel spray characteristics can represent the experimental phenomenon. After validating, we are able to use the data (Figure 6) for calculation heat transfer coefficient.

Comparison Heat transfer correlation with other researchers.



(a). Combined effect of impingement distance/injection pressure



(b). Combined effect of oxygen concentration/injection pressure

Figure 7. Comparison heat transfer correlation

Paper Lists

1. Characteristics of flat-wall impinging spray flame and its heat transfer under small diesel engine-like condition, 2017 Small Engine Technologies Conference & Exhibition, SAE Paper No. 2017-32-0032/JSAE Paper No. 20179032 (2017), pp. 1-7.
2. Experimental study on flat-wall impinging spray flame and its heat flux on wall under diesel engine-like condition: First report—effect of impingement distance, Journal of Automobile Engineering, Institution of Mechanical Engineers, Part D, DOI: 10.1177/0954407018778153 (2018). (in press).
3. Characteristics of flat-wall impinging spray flame and its heat transfer under small diesel engine-like condition. 3th report: effect of oxygen concentration, ICATECH, IOP Conference Series: Materials Science and Engineering. 462. 012046. DOI:10.1088/1757-899X/462/1/012046. (2019).
4. Effects of injection pressure and impingement distance on flat-wall impinging spray flame and its heat flux under diesel engine-like condition, Advances in Mechanical Engineering (AIME) Journal, (2019). DOI.org/10.1177/1687814019862910
5. Characteristics of flat-wall impinging spray flame and its heat transfer under diesel engine-like condition: effects of injection pressure, nozzle hole diameter and impingement distance, JSAE 20199255. JSAE/SAE 2019 International Powertrains, Fuels and Lubricants Conference.